Unsteady Aerodynamics of Delta Kites applied to Airborne Wind Energy Systems

by

Iván Castro-Fernández

in partial fulfillment of the requirements for the degree of Doctor in the PhD Program in Aerospace Engineering

Universidad Carlos III de Madrid

Advisors:
Prof. G. Sánchez-Arriaga
Prof. R. Cavallaro

Tutor:
Prof. G. Sánchez-Arriaga

Leganés, October 2023

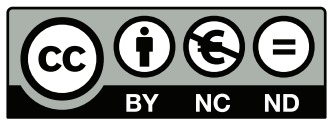

A Cristina, gracias por tu apoyo incondicional...

Unsteady Aerodynamics of Delta Kites applied to Airborne Wind Energy Systems

Iván Castro-Fernández

Aerospace Engineering Department, Universidad Carlos III de Madrid
Avenida de la Universidad, 30, Leganés, Spain

Abstract

Airborne wind energy (AWE) is an emerging field within the wind power sector that aims at harvesting energy or gain traction from tethered aircraft flying at high altitudes. Aerodynamics becomes one of its critical areas due to its influence on both the flight physics and the energy generation process during typical figure-of-eight and circular trajectories. Despite the dynamic nature of these maneuvers, unsteady aerodynamics remains nearly unexplored in AWE. This dissertation studies the aerodynamics of a two-line rigid-framed delta kite applied to AWE with the objective of improving the aerodynamic understanding and preparing models to be combined with dynamic and control software. The contents are classified into two main blocks: the first focuses on numerical unsteady aerodynamics, and the second involves the preparation and testing of a small-scale AWE testbed aimed at the aerodynamic characterization of kites.

The first block investigates the aerodynamics of the delta kite through numerical simulation with particular emphasis on the unsteady behavior. A fast unsteady potential-flow aerodynamic tool (UnPaM) was firstly benchmarked against experimental data from a previous flight test campaign. The estimated state vector included the kinematic state of the kite (aerodynamic velocity vector and angular rates, among others) and the aerodynamic force and moment coefficients about the kite center of mass. The recorded kite kinematics was prescribed in UnPaM and the resulting numerical aerodynamic coefficients were compared with the experimental counterparts. The inviscid tool was able to reproduce the order of magnitude and trend of the experimental lift and lateral force coefficients versus the angle of attack and sideslip angle, respectively. The drag coefficient was underestimated by UnPaM, which ignores viscous drag and flow separation. Although the numerical and experimental moment coefficients were in the same order, the comparison was cumbersome due to experimental uncertainties. Moreover, steady, quasi-steady and unsteady potential-flow effects were compared by performing three independent simulations with UnPaM. The quasi-steady assumption, which considers the full kite kinematics but neglects wake roll-up, among others, resulted sufficient for this case study.

A further post-processing of the former experimental data and new flow visualization data of the delta kite suggested dynamic stall phenomenology induced by periodic changes in the angle of attack. These evidences inspired a numerical study on dynamic stall by using three unsteady aerodynamic tools at different levels of approximation and computational cost. The first is the potential-flow tool UnPaM presenting the lowest fidelity. The second tool is the open-source computational fluid dynamics (CFD) code SU2 configured to solve the Reynolds-averaged Navier-Stokes equations closed with the $k-\omega$ SST turbulence model. The third, with a fidelity level between UnPaM and SU2, is a semi-empirical dynamic stall tool based on the Leishman-Beddoes model that combines attached flow through UnPaM with a phenomenological module. The latter consists of three ordinary differential equations with free empirical parameters that were fine tuned

with CFD data from SU2. The periodic kite kinematics was imposed in the three tools and the aerodynamic coefficients were compared among one another and the experimental results. UnPaM was unable to reproduce dynamic stall due to its inherent inviscid nature. The CFD and semi-empirical tools provided very consistent lift and drag coefficients versus the angle of attack curves that qualitatively matched the experimental hysteresis behavior. Moreover, a leading-edge vortex that periodically forms and detaches on the kite extrados was identified from CFD data corroborating experimental flow visualizations. Finally, a preliminary analysis of aerostructural deflections revealed that dynamic stall and fluid-structure interaction may work collaboratively causing stronger hysteresis cycles.

The second block of this dissertation focuses on the development and testing of a small-scale AWE infrastructure for aerodynamic, dynamic and control characterization of two-line and three-line kites. The testbed consists of a rigid-framed delta kite and a ground control unit on the air and ground segments, respectively. The kite avionics includes an inertial measurement unit, a magnetometer, two differential GNSS receivers and a flow visualization system. The latter was used to record surface tufts covering the kite extrados. The control unit has lateral steering and reel-in/reel-out capabilities through an automatic linear actuator and a winch. Moreover, it is equipped, among others, with load cells, a wind station and a novel visual motion tracking system. The latter is based on three cameras and an artificial neural network and has the capability of reconstructing the kite position and course angle. The results of a five-min flight were used to characterize the control of the delta kite and ground control unit. Linear correlations between the time derivative of the course angle and the delayed steering input and differential tether tension were identified. The dispersion between the time derivative of the course angle and the differential tether tension was lower, suggesting that such a variable may be adequate to close the control loop. The reconstructed kite position and course angle by the visual motion tracking system presented a good agreement with independent onboard data. Moreover, the three-camera system proved robust due to its nearly continuous operation (99.9% of the time), opening the possibility of using it as a redundant observation or backup system for the avionics.

Keywords: Airborne wind energy; automatic testbed; dynamic stall; rigid-framed delta kite; unsteady aerodynamics; visual motion tracking system.

Aerodinámica No-Estacionaria de Cometas en Delta aplicadas a Sistemas de Generación de Energía Eólica Aerotransportada

Iván Castro-Fernández
Departamento de Ingeniería Aeroespacial, Universidad Carlos III de Madrid
Avenida de la Universidad, 30, Leganés, España

Resumen

La energía eólica aerotransportada (AWE, por sus siglas en inglés) es un campo emergente dentro del sector de la energía eólica que tiene como objetivo generar energía o ganar tracción a partir de aeronaves amarradas a tierra que vuelan a gran altitud. La aerodinámica es una de sus áreas críticas debido a su influencia tanto en la física del vuelo como en el proceso de generación de energía durante trayectorias típicas en forma de ocho y círculos. A pesar de la naturaleza dinámica de estas maniobras, la aerodinámica no estacionaria permanece prácticamente inexplorada en el campo AWE. Esta tesis estudia la aerodinámica de una cometa en delta de dos líneas aplicada a AWE con el objetivo de mejorar el conocimiento aerodinámico y preparar modelos para ser combinados con software dinámico y de control. Los contenidos se dividen en dos bloques principales: el primero se centra en aerodinámica numérica no estacionaria y el segundo lleva a cabo la preparación y ensayo de un banco de pruebas para AWE a pequeña escala cuyo propósito es la caracterización aerodinámica de cometas.

El primer bloque investiga la aerodinámica de la cometa en delta a través de simulación numérica, con énfasis en el comportamiento no estacionario. Una herramienta aerodinámica potencial no estacionaria rápida (UnPaM) se comparó inicialmente con datos experimentales de una campaña de pruebas de vuelo previa. El vector de estado estimado incluía el estado cinemático de la cometa (vector velocidad aerodinámica y velocidades angulares, entre otros) y los coeficientes de fuerza y momentos aerodinámicos alrededor del centro de masas de la cometa. La cinemática medida de la cometa se prescribió en UnPaM y se compararon los coeficientes aerodinámicos numéricos resultantes con sus equivalentes experimentales. La herramienta no viscosa pudo reproducir el orden de magnitud y la tendencia de los coeficientes de sustentación y fuerza lateral experimentales en función del ángulo de ataque y el ángulo de resbalamiento, respectivamente. El coeficiente de arrastre fue subestimado por UnPaM, que ignora el arrastre viscoso y la separación del flujo. Aunque los coeficientes de momento numéricos y experimentales tenían el mismo orden de magnitud, la comparación resultó complicada debido a incertidumbres experimentales. Además, se compararon los efectos de flujo potencial estacionario, cuasiestacionario y no estacionario mediante tres simulaciones independientes con UnPaM. La asunción cuasiestacionaria, que considera la cinemática completa de la cometa pero ignora, entre otras cosas, el enrollamiento de la estela, resultó suficiente para este caso de estudio.

Un posterior procesamiento de los datos experimentales y nuevos datos de visualización del flujo de la cometa en delta sugirió fenómenos de entrada en pérdida dinámica inducidos por cambios periódicos en el ángulo de ataque. Estas evidencias inspiraron un estudio numérico sobre la entrada en pérdida dinámica utilizando tres herramientas aerodinámicas no estacionarias a diferentes niveles de aproximación y costo computacional. La primera es la herramienta de flujo potencial no estacionario UnPaM, que presentaba la menor fidelidad. La segunda herramienta es el código de dinámica de fluidos computacional

(CFD) de código abierto SU2 configurado para resolver las ecuaciones de Navier-Stokes promediadas en Reynolds cerradas con el modelo de turbulencia $k-\omega$ SST. El tercero, con un nivel de fidelidad entre UnPaM y SU2, es una herramienta semiempírica de entrada en pérdida dinámica basada en el modelo Leishman-Beddoes que combina el flujo adherido a través de UnPaM con un módulo fenomenológico. Este último consiste en tres ecuaciones diferenciales ordinarias con parámetros empíricos libres que se ajustaron con datos de CFD de SU2. La cinemática periódica de la cometa se impuso en las tres herramientas y se compararon los coeficientes aerodinámicos entre las tres herramientas y con los resultados experimentales. UnPaM no pudo reproducir la entrada en pérdida dinámica debido a su naturaleza no viscosa. Las herramientas CFD y semiempíricas proporcionaron coeficientes de sustentación y arrastre muy consistentes en función del ángulo de ataque que coincidieron cualitativamente con el comportamiento de histéresis experimental. Además, se identificó un vórtice en el borde de ataque que se forma y desprende periódicamente en el extrados de la cometa en los datos CFD, corroborando las visualizaciones del flujo experimentales. Finalmente, un análisis preliminar de las deflexiones aeroestructurales reveló que la entrada en pérdida dinámica y la interacción fluido-estructura puede que trabajen colaborativamente causando ciclos de histéresis más intensos.

El segundo bloque de esta tesis se centra en el desarrollo y ensayo de una infraestructura AWE a pequeña escala para la caracterización aerodinámica, dinámica y de control de cometas de dos y tres líneas. El banco de ensayos consta de una cometa delta de estructura rígida y una unidad de control en tierra en los segmentos de aire y tierra, respectivamente. La aviónica de la cometa incluye una unidad de medición inercial, un magnetómetro, dos receptores GNSS diferenciales y un sistema de visualización del flujo. Este último se utilizó para grabar una serie de mechones que cubrían el extrados de la cometa. La unidad de control tiene capacidades de dirección lateral y enrollado/desenrollado a través de un actuador lineal automático y un carrete. Además, está equipada, entre otros, con células de carga, una estación meteorológica y un novedoso sistema visual de seguimiento de movimiento. Este último se basa en tres cámaras y una red neuronal artificial y tiene la capacidad de reconstruir la posición de la cometa y el ángulo de curso. Los resultados de un vuelo de cinco minutos se utilizaron para caracterizar el control de la cometa delta y la unidad de control en tierra. Se identificaron correlaciones lineales entre la derivada temporal del ángulo de curso y versiones retrasadas de la entrada de control lateral y tensión diferencial de las líneas. La dispersión entre la derivada temporal del ángulo de curso y la tensión diferencial de las líneas retrasada fue menor, lo que sugiere que esta variable puede ser adecuada para cerrar el lazo de control. La posición y el ángulo de curso de la cometa reconstruidos por el sistema visual de seguimiento de movimiento presentaron una buena concordancia con datos independientes a bordo. Además, el sistema de tres cámaras demostró ser robusto debido a su operación casi continua (99.9% del tiempo), abriendo la posibilidad de utilizarlo como sistema de observación redundante o de respaldo para la aviónica.

Palabras clave: Energía eólica aerotransportada; banco de ensayos automático; entrada en pérdida dinámica; cometa en delta de estructura rígida; aerodinámica no estacionaria; sistema visual de seguimiento de movimiento.

Acknowledgements

This thesis has been carried out in the Aerospace Engineering Department at Universidad Carlos III de Madrid. The financial support has been partially provided by the Universidad Carlos III de Madrid, through a PIPF scholarship awarded on a competitive basis, and under the framework of the GreenKite-2 project (PID2019-110146RB-I00) funded by MCIN/AEI/10.13039/501100011033.

I would like to express my gratitude to the people that have supported me in different ways during this four-year journey. First of all, my warmest thanks to my two thesis advisors, Prof. Gonzalo Sánchez Arriaga and Prof. Rauno Cavallaro, for giving me the opportunity to develop a PhD thesis under their supervision and for their tireless support. I arrived to the Aerospace Engineering Department being a child with some physical and engineering concepts in my mind and now I am becoming a well-educated doctor. Not only my technical knowledge was expanded but also my personal and scientific maturity thanks to them... Gonzalo, keep being such a nice and humble person whatever your professional degree is. You always find the time for your students and make them grow... Rauno, keep teaching your students and learning from them as you used to do with me. I never thought that a supervisor could be such a good colleague.

Along the PhD, I have met a number of good friends that taught me many different things and, more importantly, gave me a way out to work and problems. To all the phycologists and humorists involved in the Thursday's (Sanjurjo's) and Friday's beers, big thanks from your good friend. Besides fun, we also used to work hard and as a team. Ricardo, the pioneer, Paco, the third PhD student on Airborne Wind Energy (AWE) at UC3M, and my motivated Bachelor's students many thanks for your continuous help with the hardware-related tasks. To the UC3M AWE group, keep growing and making things happen thanks to your effort. I really wish to see AWE technology fully deployed in the near future. It is impossible to forget my research stay at TU Delft in The Netherlands during my third year of PhD. Prof. Roland Schmehl, his PhD students and the whole wind energy team embraced me with a hospitality that I will never forget. Thanks to all of them and in particular to my good friends Mehtab, Rishi and Filippo. You made me see that a day has an optimal number of working hours and exceeding this is counterproductive.

Focusing on a single topic when one starts a PhD is probably the most desirable situation to become an expert on the discipline. Even though I put much effort into doing a single thing at a time, I could not satisfy my hunger for science and engineering. Since my PhD topic deserved between 8-10 hours a day, I decided to spend around 90% of my spare time (evenings and weekends) on technical side projects. For my first side activity, my good friend Jesús proposed me and a few friends to build a team, DZH Dynamics, to

do research on novel spacecraft attitude control techniques, completely off-topic for me by that time but attractive! After probably the most vast amount of work of our lives, we managed to perform a parabolic flight campaign in the Fly Your Thesis! 2021 programme from the European Space Agency (ESA). Thanks to Jesús, Guillermo, Fran, Manuel, Chema, Javi, Antonio and all the hard workers that made this possible. Regarding my second and more personal side project, flags flutter for energy harvesting, I would like to thank Prof. Miguel Fosas and Prof. Antonio Juan Gámez, who supervised my Bachelor's thesis at Universidad de Cádiz, Prof. Rauno Cavallaro and Dr. Rocco Bombardieri, that supervised my Master's thesis at UC3M, my colleague Prof. Marco Raiola and my student and friend Martín. We understood the complex physics of flags flutter, and build a flags simulator and a real energy harvester from scratch. The third and last side activity during the last months of PhD was to prepare an exam for a public position at INTA that I ended up earning. Dear Juan, I owe you one for your continuous inputs and motivation.

To finish my acknowledgements, I find no words to appreciate the emotional support provided by my family and friends. Four years ago, they encouraged me to do what I wished regardless of the salary, distance and sacrifice. With all my love, I dedicate this dissertation to Cristina who has supported me and cheer me up every day. You are the most beautiful, nice and understanding person in the World. Big thanks also to her family who gave me a second home and so much support. My parents Mari Carmen and Juan Antonio, my siblings Juan Antonio and Esther, my grandparents Carmen, Pascual, María and Raimundo and the rest of my family constitute one of the strongest pillars in my life. Apart from their continuous support and love, they taught me how to work hard and make dreams come true with humbleness. Thanks to my best friends Álvaro, Torres, Rafa, Paco, Juan Carlos, Miguelillo..., together since our childhood and still united. I learned so many things from you and enjoyed so many good times. Thanks to my endearing flatmates Manuel, Juan Martín, Marta and Antonia for spending so many seasons (every year was a season!) with me and hearing so many problems of mine. You always did a bit of magic to restore my positivity.

I am becoming a doctor thanks to all of you...

Preface

This thesis investigates the unsteady aerodynamics of delta kites applied to airborne wind energy by combining experiments and simulations. The thesis is structured in three chapters. The first chapter provides an overview of the thesis including a top-level introduction (Section 1.1), a state of the art of numerical and experimental aerodynamic methods applied to AWE aircraft (Section 1.2), an introduction to dynamic stall phenomenology (Section 1.3) and a summary of experimental setups in airborne wind energy (Section 1.4). Chapter 2 contains a compendium of the three articles published and submitted during the development of the thesis. The papers are adjusted to comply with the present thesis format for consistency, but their contents have not been altered as compared with their original counterparts. Paper 1 benchmarks a low- to mid- fidelity unsteady potential-flow aerodynamic code applied to a delta kite against experimental data from a former flight campaign. The second paper focuses on the dynamic stall behavior of the same delta kite and introduces two new unsteady viscous tools. The third paper presents the architecture and a flight test campaign of a small-scale machine consisting of an automatic ground control unit and the delta kite. Chapter 3 summarizes the main conclusions, contributions and future lines of work of the thesis.

Paper 1. Castro-Fernández, I.; Borobia-Moreno, R.; Cavallaro, R. & Sánchez-Arriaga, G., 2021. *Three-Dimensional Unsteady Aerodynamic Analysis of a Rigid-Framed Delta Kite applied to Airborne Wind Energy.* Energies **14(23)** (8080).

Paper 2. Castro-Fernández, I.; Cavallaro, R.; Schmehl R. & Sánchez-Arriaga, G., 2023. *Unsteady Aerodynamics of Delta Kites for Airborne Wind Energy under Dynamic Stall Conditions.* Wind Energy **(Under Review)**.

Paper 3. Castro-Fernández, I.; DeLosRíos-Navarrete, F.; Borobia-Moreno, R.; Fernández-Jiménez, M.; García-Cousillas, H.; Zas-Bustingorri, M.; Ghobaissi, A. T.; Lopez-Vega, F.; Best, K.; Cavallaro, R. & Sánchez-Arriaga, G., 2023. *Automatic Testbed with a Visual Motion Tracking System for Airborne Wind Energy Applications.* Wind Energy **26(4)**, 388-401.

October 2023, Leganés
Iván Castro-Fernández

Division of work between authors

Paper 1. Conceptualization: RC and GSA; Formal analysis: ICF and RBM; Methodology: ICF and RBM; Software: ICF and RC; Writing - original draft: ICF; Writing - review & editing: RBM, RC and GSA; Supervision: RC and GSA;

Paper 2. Conceptualization: RC, RS and GSA; Formal analysis: ICF; Methodology: ICF; Software: ICF and RC; Writing - original draft: ICF; Writing - review & editing: RC, RS and GSA; Supervision: RC, RS and GSA;

Paper 3. Conceptualization: GSA; Formal analysis: ICF and GSA; Methodology: ICF, FRN, MFJ, HGC, MZB, AG, FLV and KB; Software: ICF and FRN; Writing - original draft: ICF; Writing - review & editing: FRN, RBM, RC and GSA; Supervision: RC and GSA;

Acronyms correspond to:

ICF Iván **Castro-Fernández**. Universidad Carlos III de Madrid. *PhD Candidate*.
GSA Gonzalo **Sánchez-Arriaga**. Universidad Carlos III de Madrid. *Advisor and Tutor*.
RC Rauno **Cavallaro**. Universidad Carlos III de Madrid. *Advisor*.
RS Roland **Schmehl**. Delft University of Technology. *Advisor during international stay*.
RBM Ricardo **Borobia-Moreno**. Instituto Nacional de Técnica Aeroespacial.
FRN Francisco **DeLosRíos-Navarrete**. Universidad Carlos III de Madrid.
MFJ Manuel **Fernández-Jiménez**.
HGC Helena **García-Cousillas**.
MZB María **Zas-Bustingorri**.
AG Álvaro Tarek **Ghobaissi**.
FLV Francisco **López-Vega**.
KB Kim **Best**.

Other research merits related to the thesis

Besides the three articles included in this thesis, the author was involved in the following journal publications related to AWE systems:

Borobia-Moreno, R.; Castro-Fernández, I.; Pastor, A.; Endo, H.; Cobos, C.; Cavallaro, R. & Sánchez-Arriaga, G., 2020. *Activities and Roadmap on Airborne Wind Energy Systems at UC3M.* Journal of Japan Wind Energy Society **44.134**, 188-191.

Trevisi, F.; Castro-Fernández, I.; Pasquinelli, G.; Riboldi, C.E.D. & Croce A., 2022. *Flight Trajectory Optimization of Fly-Gen Airborne Wind Energy Systems through a Harmonic Balance Method.* Wind Energy Science **7(5)**, 2039-2058.

Conferences

The work of this thesis was presented by the author in the following international conferences:

Castro-Fernández, I.; Borobia-Moreno R.; Cavallaro, R. & Sánchez-Arriaga, G., *3D Unsteady Aerodynamic Analysis of a Rigid-Framed Delta Kite applied to AWES.* Wind Energy Science Conference (WESC 2021). Hannover, Germany, 2021.

Castro-Fernández, I.; Cavallaro, R.; Schmehl, R. & Sánchez-Arriaga, G., *A Semi-Empirical Aerodynamic Model Based on Dynamic Stall for Rigid-Framed Delta Kites during Figure-of-Eight Maneuvers.* Airborne Wind Energy Conference (AWEC 2021). Milan, Italy, 2022.

Castro-Fernández, I.; Cavallaro, R.; Schmehl, R. & Sánchez-Arriaga, G., *Multi-Fidelity Computational Aerodynamic Framework for the Static and Dynamic Behavior of Rigid-Framed Delta Kites for Airborne Wind Energy.* Wind Energy Science Conference (WESC 2023). Glasgow, UK, 2023.

Other works in which the author was involved were presented in the following international conferences:

DeLosRíos-Navarrete, F.; Castro-Fernández, I.; Fernández-Jiménez, M., Zas-Bustingorri, M.; Tarek-Ghobaissi, A.; Cobos-Pérez, C. & Sánchez-Arriaga, G., *Status of UC3M Testbed for the Aerodynamic Characterization of Kites Applied to Airborne Wind Energy Systems.* Airborne Wind Energy Conference (AWEC 2021). Milan, Italy, 2022.

Trevisi, F.; Castro-Fernández, I.; Croce, A.; Riboldi, C.E.D & Pasquinelli, G., *Optimal Flight Path for Fly-Gen Airborne Wind Energy Systems.* Airborne Wind Energy Conference (AWEC 2021). Milan, Italy, 2022.

DeLosRíos-Navarrete, F.; Castro-Fernández, I.; Cavallaro R. & Sánchez-Arriaga, G., *Experimental Validation of an Airborne Wind Energy Simulator based on a Semi-Empirical Aerodynamic Model.* Wind Energy Science Conference (WESC 2023). Glasgow, UK, 2023.

Contents

Chapter 1

Overview and state of the art

1.1. Introduction

Climate change has become a major concern for any living being on Earth. Despite climate cycles have naturally existed in the history of our planet, the present climate change is unequivocally caused by human activities through their emissions of greenhouse gases (IPCC 2023). The global surface temperature grew 1.1°C during $2011 - 2020$ with respect to $1850 - 1900$ primarily due to unsustainable energy and land use, consumerism and overproduction in certain regions across the globe. A decarbonised power sector is the key to a sustainable energy future. To meet the goals of the Paris Agreement[1], the international renewable energy agency proposes to scale up renewable energy sources at least six times faster than in the past (Dolf Gielen *et al.* 2018). Moreover, the share of renewable energy should increase from 25% (currently) to 85% by 2050. Figure 1.1 shows the evolution of renewable electricity generation in the World and its main sources. Not only the total renewable energy produced is continuously increasing but also the relative weight of wind power, reaching 25% in 2022. In fact, wind power is receiving especial attention by most of the European states, particularly by Germany, Spain and the UK which concentrate the highest annual and cumulative installed wind capacities (Bórawski *et al.* 2020). Traditional wind turbines have become the preferred option due to their reliable operation and low levelized cost of energy ($\sim$ 40 €/MWh) (BVG Associates 2022). New emerging technologies, which may present socio-economic and environmental advantages as compared to windmills, can also contribute to the mix of renewable energy generation.

Airborne wind energy (AWE) is an innovative field that attempts to address some of the current limitations of established wind turbines such as their high infrastructure costs, limited operational altitude and lack of mobility. AWE systems employ tethered aircraft to harvest energy or gain traction from high-altitude winds. As compared to wind turbines, they replace the tower and blades by a tether and one or several aircraft, respectively. This allows them to fly at higher altitudes, where winds are generally stronger and less intermittent, and change their operating altitude to maximize the power output (Ecorys 2018). The concept was originally proposed by M. L. Loyd in the late 70's (Loyd 1980). He envisioned three modes of operation: the simple kite that was only subject to tether reel-out motion, the lift power mode (also known as ground-gen) where the kite flies crosswind patterns (i.e., orthogonal to the wind) to maximize the power produced by a generator on the ground, and the drag power mode (also known as fly-gen) which uses onboard wind turbines creating additional drag which translates into power. He anticipated that a kite working either in lift or drag power modes, both flying crosswind trajectories, could potentially harness the same amount of power being this about 40 times

[1] Available online at `https://www.un.org/en/climatechange/paris-agreement`

[2] Available online at `https://ourworldindata.org/grapher/modern-renewable-energy-consumption?facet=none`.

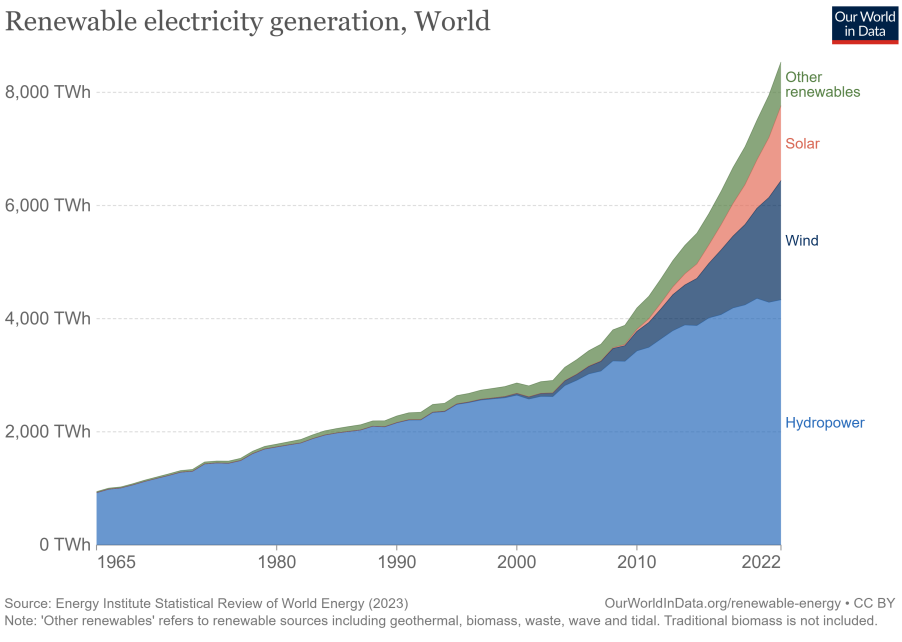

Figure 1.1: Renewable electricity generation in the world. Source: Our World in Data.[2]

higher than for the simple kite. For this reason, crosswind motion is normally adopted in AWE applications.

Despite its early introduction, the plethora of AWE developments has mostly occurred since 2000 (Fagiano & Milanese 2012) and it continues to progress in the present (Watson *et al.* 2019). A comprehensive review of AWE technology was presented in 2015 (Cherubini *et al.* 2015) and more recently in Vermillion *et al.* (2021). Many different concepts have been proposed but no clear convergence toward a winning architecture has yet been identified. AWE research and development has been mainly fostered by European countries and the US with a total public investment of \$58M and \$13M, respectively, since 2008 (U.S. Department of Energy 2021). In addition, about 20 small companies are developing AWE devices. Some of them are already commercializing systems in the order of 100 kW (SkySails Power 2022; Kitepower 2022) and others expect to have a commercial onshore system by 2025 (BVG Associates 2022).

Besides electrical energy generation, transportation applications also benefit from tethered kites. In fact, SkySails Power (SkySails Power 2022), which is one of the leading AWE companies, was a pioneer of kite-based propulsion systems of seagoing vessels (Erhard & Strauch 2013). They commercialized a system with a propulsion power of up to 2 MW using kites of up to 400 m^2 at altitudes above 200 m. However, the company decided to focus its efforts on airborne wind energy generation since 2012. A more recent project between the University of Stuttgart and the German company OCEANERGY AG[3] aims

[3]Available online at `https://www.ifb.uni-stuttgart.de/en/research/windenergy/projects/ICM-autoKite/`

to employ ships as mobile platforms to harvest energy of mid-ocean winds with a kite. The goal is to use this green electricity to propel the ship and produce affordable hydrogen and e-fuels onboard the ships. Nevertheless, the ocean does not seem to be the only medium of transportation for kite-propelled vehicles since a singular sustainable vehicle known as the WindSled was used in several explorations in the polar regions. It consists of a sled pulled by a 150 m^2 kite (González & Moreno 2019). This kind of applications presents clear synergies with AWE generators and they must work collaboratively for their parallel development.

AWE systems are currently in a development stage and must be further optimized. Within the multidisciplinary nature of these systems involving flight dynamics (Sánchez-arriaga *et al.* 2019), control (Vermillion *et al.* 2021) and fluid-structure interaction (Fasel *et al.* 2019), among others, aerodynamics has a crucial role. An accurate aerodynamic characterization of kites during crosswind trajectories through test and/or simulation may be used to improve the overall performance of AWE systems. Moreover, any AWE model requires an accurate and, if possible, fast aerodynamic module for coupling with other physics-based modules. On the other hand, despite AWE systems have demonstrated automatic energy generation and propulsion capacity, they need to face important technical challenges for their complete entry into market (Ecorys 2018). Fully automated takeoff and landing together with prolonged autonomous operation are the two most desired features (BVG Associates 2022) in AWE full-scale machines. In the past, important lessons were learned thanks to small-scale AWE prototypes due to their low cost and versatility. For instance, they were employed to characterize the dynamics and control of membrane wings steered by a ground-based control unit (Fagiano & Marks 2015). Small-scale testbeds continue to be fundamental for the advance of technical and scientific knowledge in the AWE field. In these regards, the contribution of this thesis covers two relevant aspects in the development of AWE systems: (i) unsteady aerodynamics of delta kites applied to AWE and (ii) development and testing of a small-scale testbed aimed at aerodynamic, dynamic and control characterization.

1.1.1. Objectives

The main goal of this dissertation is:

> Improving aerodynamic models and understanding of delta kites applied to airborne wind energy by combining experiments and simulations.

To achieve this goal, the following research objectives are proposed:

- Investigate the aerodynamics of delta kites by comparing experimental data (obtained in a former flight test campaign) and numerical results from an unsteady potential-flow tool.
- Characterize experimentally the dynamic stall phenomenon during the crosswind flight of delta kites by further post-processing the experimental data and preparing a flow visualization setup.
- Perform a detailed unsteady aerodynamic study of delta kites by applying and comparing three tools at different levels of fidelity and computational cost to explore the dynamic stall behavior.
- Develop and test a small-scale testbed for aerodynamic, dynamic and control characterization of two-tether and three-tether AWE systems.

1.2. Aerodynamics of airborne wind energy systems

This section provides a comprehensive state of the art of AWE systems aerodynamics. This was investigated in the literature at two different scales: (i) large scale that considers the complete trajectory of the aircraft, its aerodynamic wake and, potentially, other aircraft in the same AWE farm; and (ii) small scale by considering the detailed aircraft aerodynamics. Approach (i) is presented in Section 1.2.1. Then, approach (ii) is covered in Sections 1.2.2, 1.2.3, 1.2.4 by discussing the different wing types applied to AWE, and the numerical and experimental aerodynamic works. The discussions are limited to aircraft aerodynamics excluding tether, blade and rotor aerodynamics.

1.2.1. Wake and AWE farm aerodynamics

Wake and AWE farm aerodynamics is commonly associated with the design of AWE systems and wind farms layout. As in conventional wind turbines, it attempts to quantify induction effects, i.e., slowdown of the incoming wind caused by the AWE system itself and/or by others in the same park. From a physical point of view, the incoming flow must reduce its speed if power is extracted from it. In fact, the Betz's limit[4] applies to traditional wind turbines. In regard to AWE, important discussions arose after the pioneering work of Loyd's (Loyd 1980) neglected the induction effects arguing that, to maximize power, the ratio between the kite area and the swept area must be minimized (i.e., minimum induction). Other successive works (Archer 2013; Costello *et al.* 2015) doubted about the application of the Betz's limit to AWE due to the invalid assumption of disc-like swept area and the small kite area versus the large swept area. Nevertheless, other works concluded that the induction factor for a single 14 MW kite and multi-kite systems reduce the power production in roughly 30% (Zanon *et al.* 2014; Leuthold *et al.* 2017). In addition, they concluded that the induction factor is mainly axial, i.e., along the tether direction.

Some of the past computational aerodynamic studies focused on wind farm aerodynamics using CFD to solve large three-dimensional domains to assess the performance of one crosswind power kite (Kheiri *et al.* 2018, 2022; Pynaert *et al.* 2023) and AWE farms consisting of fly-gen and ground-gen AWE systems (Haas *et al.* 2022). More recently, an analytical wake model to compute the induced drag at a low computational cost was proposed in Trevisi *et al.* (2023). The resulting helicoidal wake was split into two components: a near wake with a similar effect to that in forward flight and a far wake, whose effect greatly depends on the trajectory turning radius. The smaller the turning radius, the higher the induction factor. It is therefore concluded that the small-domain aerodynamic approach containing the kite and its near wake is sufficient to obtain the pressure distribution and resulting forces and moments for aeroelastic, dynamic and control computations, among others. The far wake should be included for design and optimization of AWE systems if applicable depending on the flight trajectory and farm layout.

1.2.2. Aerodynamic studies organized by wing type

The aircraft is an essential component of every AWE system. At this stage of development, there is not a preferred aircraft architecture, and both fixed-wing and soft kites are used by companies and research groups. In fact, this depends, among others, on the structural

[4]Maximum theoretical efficiency (59.3%) of a wind turbine considering basic principles of mass and momentum conservation.

and aerodynamic requirements of the specific type of AWE system. For instance, the most powerful fly-gen system (600 kW) to date developed by the company Makani used a drone-like aircraft to accommodate eight small wind turbines (Echeverri *et al.* 2020*a*; Makani Team 2020; Echeverri *et al.* 2020*b*). Similarly to airplanes, horizontal and vertical tails are necessary for stability and control in fixed-wing AWE aircraft. On the other hand, soft (membrane-like) or semi-rigid (rigid frame + membrane canopy) wings are generally employed in ground-gen applications due to their light weight and low cost (Erhard & Strauch 2015; Viré *et al.* 2020; Candade *et al.* 2020*b*). In this case, the high tether forces are distributed over the kite structure through a bridle system. Figure 1.2 shows typical fly-gen (a-b) and ground-gen (c-f) AWE aircraft (Cherubini *et al.* 2015).

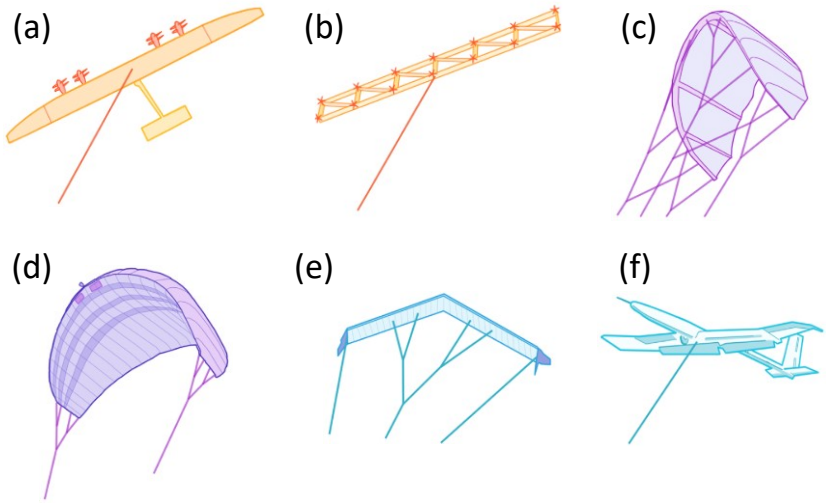

Figure 1.2: Main types of aircraft in fly-gen (a-b) and ground-gen (c-f) systems. Examples of AWE companies using aircraft types (a) to (f) are Makani, KiteKraft, Kite Power, Skysails Power, EnerKíte and Ampyx Power, respectively. Source: adapted from Cherubini *et al.* (2015).

Fixed-wing AWE aircraft (Figures 1.2a, 1.2b, 1.2f) are aerodynamically similar to small airplanes. In fact, an aerodynamic parameter identification from flight test data was conducted in Licitra *et al.* (2017) by using an estimation algorithm traditionally applied to conventional aircraft. The available computational fluid dynamics (CFD) studies put their efforts on multi-element airfoils due to their high-lift capability (De Fezza & Barber 2022; Ko *et al.* 2023) and pre-commercial machines such as the ground-gen Ampyx Power AP-3 (Vimalakanthan *et al.* 2018) and the fly-gen Makani M600 (Mehr *et al.* 2020). Interestingly, the interaction between the upper and lower rotors of the M600 aircraft have a positive effect on the wing lift as compared to the wing without rotors (Mehr *et al.* 2020).

Regarding soft kites, especial attention was paid to leading-edge inflatable (LEI) (Figure 1.2c) and ram-air (Figure 1.2d) kites due to their commercial availability for kitesurfing and paragliding. LEI kites consist of an inflated leading-edge tube and several chordwise struts distributed along the wing span to provide structural integrity, and a canopy that provides the aerodynamic shape and cope with the aerodynamic pressure. The

first 2D numerical studies of the flow past an airfoil of a LEI kite highlighted the presence of a strong recirculation zone behind the leading-edge tube and flow separation on the suction side even at moderate angles of attack (Breukels 2010; Breukels *et al.* 2013; Folkersma *et al.* 2019). A similar behavior and significant cross flow along the span was identified in a 3D aerodynamic study of a LEI kite (Viré *et al.* 2020). Moreover, a follow-up work (Viré *et al.* 2022) concluded that the effect of chordwise struts is negligible irrespective of the sideslip angle, however, the latter does affect the wing aerodynamic efficiency. Ram-air kites are flexible wings inflated by the apparent wind. This makes them virtually indestructible and eases their deployment and stowing in the field. However, these kites are subject to strong fluid-structure interaction. Work Folkersma *et al.* (2020) revealed that the aeroelastic deformation of ram-air kites further improves their aerodynamic performance as compared to the same rigid wing because the camber increases. In contrast, the formation of bumps near the leading edge and the high spanwise bending become competing aeroelastic phenomena since they create extra drag and lower the aerodynamic efficiency of these kites. Likewise, the aerostructural deformation of ram-air kites was measured during wind tunnel tests highlighting similar deformation features (de Wachter 2008).

Swept semi-rigid wings (Figure 1.2e) are used by companies like EnerKíte and the AWE group of Universidad Carlos III de Madrid (UC3M)[5]. The EnerKíte wing was aerostructurally designed (Candade *et al.* 2020*a*) and optimized (Candade *et al.* 2020*b*) considering the bridle configuration and a hybrid structure made of carbon fiber and a textile covering. At UC3M and in this thesis, the commercial acrobatic kite HQ Fazer XXL, which is a rigid-framed delta (RFD) kite with a wing span of 3.6 m shown in Figure 1.3, is considered. The kite consists of a rigid frame made of carbon fiber bars that support the membrane-like canopy. This acrobatic kite is characterized by low- to mid- aeroelastic deformations and good maneuverability.

Figure 1.3: RFD kite (HQ Fazer XXL) of the UC3M AWE group with a boom holding the multi-hole pitot tube during the flight test campaign of Borobia-Moreno *et al.* (2021). The inset shows the avionics. Source: Borobia-Moreno *et al.* (2021).

[5]Webpage at `https://aero.uc3m.es/airborne-wind-energy/`

1.2.3. Experimental aerodynamics

Conducting experimental research on the aerodynamics of AWE systems is a complicated task. On the one hand, it is almost impossible to control the aerodynamic velocity vector, like in a wind tunnel facility, because it involves the wind velocity and the complex kite dynamics. On the other hand, the control inputs normally vary the shape of the kite and, therefore, an aero-servo-elastic coupling arises. Despite many AWE small-scale machines and testbeds (see Section 1.4) were prepared in the past, only a few of them focused on aerodynamic characterization of AWE systems.

Estimation algorithms, such as the extended Kalman filter, that fuses data from on-ground and onboard sensors were used to estimate aerodynamic variables such as the aerodynamic force and moment coefficients (Borobia *et al.* 2018; Schmidt *et al.* 2020; Borobia-Moreno *et al.* 2021). One of the major difficulties lay in the accurate observation of the aerodynamic velocity vector (airspeed magnitude, angle of attack and sideslip angle). It was observed by solely using on-ground sensors in Schmidt *et al.* (2020). However, in-situ flow measurements became necessary to reduce uncertainty. The first study on this topic was Oehler & Schmehl (2019), where a system of vanes and a pitot tube was attached to the bridle lines of a LEI kite to measure the aerodynamic velocity vector. A more accurate multi-hole pitot tube was boarded on the RFD and LEI kites of the UC3M group (see RFD kite in Figure 1.3) with the same purpose in Borobia-Moreno *et al.* (2021). The estimation before modelling technique was employed to reconstruct the state vector that included aerodynamic variables. Like in Oehler & Schmehl (2019), high variations of the aerodynamic coefficients and the angle of attack were observed suggesting unsteady aerodynamic and/or aeroelastic phenomena. The experimental results from the flight test campaign of Borobia-Moreno *et al.* (2021) were used in this thesis for validation purposes in Papers 1 and 2 of Chapter 2.

1.2.4. Numerical aerodynamics

Numerical aerodynamic methods become an economic option that can be easily combined with other multi-disciplinary tools such as flight simulators. Methods at different levels of fidelity and computational cost were extensively used to study AWE aircraft aerodynamics. In the following, the methods are divided into potential-flow approaches (Section 1.2.4.1) and CFD methods (Section 1.2.4.2).

1.2.4.1. *Aerodynamic studies mainly based on potential-flow methods*

Potential-flow methods provide low- to mid-fidelity aerodynamic predictions at much lower computational cost than CFD. They are typically used for preliminary calculations where quick analyses are needed. For this reason, numerous works on AWE systems aerodynamics explored the validity of a variety potential-flow tools.

The potential-flow approximation assumes an inviscid (high Reynolds number Re) and irrotational flow (null rotational of the velocity vector) and, as a consequence, the velocity field can be computed as the gradient of a velocity potential. For the incompressible case, this velocity potential satisfies the Laplace's equation. In practical numerical methods, a number of singularities (vortices, doublets, sources, etc), that naturally satisfy Laplace's equation, are distributed on the aerodynamic surfaces (Katz & Plotkin 2001). Their strengths are computed by imposing the impenetrability boundary condition, i.e., zero

normal component of the relative velocity between the fluid and the solid. In the following, tools applied to AWE aircraft and mainly based on potential-flow methods are reviewed.

Lifting-line methods apply the Prandtl lifting-line theory (Prandtl 1918) to predict the spanwise lift distribution of 3D wings. A finite number of planar horseshoe vortices are placed along the wing span. They model three-dimensional, sweep and dihedral effects within the potential-flow assumption. For instance, the lifting-line method was successfully employed to study the flutter instability in a fixed-wing AWE system with onboard turbines (Wijnja *et al.* 2018). To improve the drag predictions, the method was used in combination with 2D viscous aerodynamic polars (Leloup *et al.* 2013; Haas *et al.* 2022). More recently, various existing lifting-line approaches, that essentially differed in implementation details of the boundary conditions, were benchmarked against one another and the vortex lattice method (VLM) used as a reference (Gaunaa 2023). The VLM makes fewer assumptions and overcomes the inability of the lifting-line methods to capture the chordwise pressure distribution.

Nonlinear vortex-step methods are similar to lifting-line methods in terms of discretization, but they account for viscous effects such as stall corrections by including externally derived nonlinear airfoil polar data. The AWE community routinely applied this method in aerostructural frameworks of fixed-wing aircraft (Damiani *et al.* 2019; Candade *et al.* 2020*b*) and LEI kites (Cayon *et al.* 2023) due to its favorable balance between accuracy and computational efficiency.

Vortex lattice methods (VLM) distribute singularities over the full aerodynamic surface and solve their strengths following the boundary element method (Katz & Plotkin 2001). They become useful for zero thickness and highly nonplanar wings. In fact, the VLM was useful to obtain the pressure distribution over camber-morphing AWE wings within an aerostructural optimization (Fasel *et al.* 2017) and a reduced-order model (Fasel *et al.* 2019). Furthermore, the VLM combined with 2D airfoil coefficients for airfoil thickness and viscous corrections was benchmarked against CFD for a C-type kite with an uniform sectional shape (Gaunaa *et al.* 2011). An excellent agreement was found for cases where the flow was attached. Since important flow separation occurs on the suction side and behind the leading-edge tube of LEI kites, a multiple-wake VLM that shed part of the total circulation from prescribed positions was proposed in Leuthold (2015). However, the author highlighted the sensitivity of this method to the prescribed separation and re-attachment points. Unlike in lifting-line and nonlinear vortex-step methods, the unsteady VLM solver is also available by shedding a wake from the trailing edge that grows in length as the simulation time advances. Ref. Fonzi *et al.* (2020) included an unsteady VLM in its nonlinear aeroelastic framework for a fixed-wing kite.

Panel methods also belong to boundary element methods and present both steady and unsteady solvers. They are applied to thick aerodynamic bodies, i.e., composed of an upper (extrados) and a lower (intrados) surfaces, like typical aircraft wings. The pressure distribution over a ram-air kite (Thedens & Schmehl 2023) and box wing kites (Eijkelhof *et al.* 2023) was studied using the open-source steady panel method APAME.

The RFD kite (Figure 1.3) studied in this thesis is a swept (delta) and highly nonplanar wing, i.e., formed by planes at different dihedral angles. For this reason, low-cost lifting line methods would not accurately predict its aerodynamic characteristics according to previous studies in AWE systems (Gaunaa 2023). Moreover, the aerodynamic surface (canopy) has zero thickness, precluding any obvious manner of externally computing

sectional polar curves. Only the VLM remains as a feasible potential-flow option. On the other hand, the majority of previous aerodynamic works focused on steady-state computations because of the typical quasi-steady assumption in AWE systems. However, the experimental results from Borobia-Moreno *et al.* (2021) revealed important unsteady phenomena in highly dynamic maneuvers of the RFD kite. Unsteady aerodynamics was identified as a research gap that this thesis attempts to fill. The unsteady VLM within the in-house unsteady panel method (UnPaM) suite (Nardini 2014; Cavallaro *et al.* 2015) was applied to the RFD kite in Papers 1 and 2 of Chapter 2.

1.2.4.2. *Aerodynamic studies based on computational fluid dynamics methods*

CFD methods are hereafter considered as numerical approaches that solve the Navier-Stokes equations (generally, conservation of mass, momentum and energy) at different levels of approximation. They are needed in AWE to accurately resolve viscous flows with significant separation as shown in multiple works (Folkersma *et al.* 2019; Viré *et al.* 2020, 2022). In viscous flows, the Reynolds number poses an important numerical limitation that impedes the use of the most accurate approximation, namely, direct numerical simulation, for all cases. For high Re ($\sim 10^6$), current computational capacities enable the resolution of the Reynolds-averaged Navier-Stokes (RANS) and large-eddy simulation equations in reasonable computational times. Both of them model all or part of the turbulence through additional closure equations (turbulence models) as compared to direct numerical simulation, where all the scales (up to the grid resolution) of the flow are resolved.

The use of large-eddy simulations is limited to the first and only (to date) work by Haas et al. (Haas *et al.* 2022) whose focus was the atmospheric aerodynamics of an AWE farm rather than the detailed aerodynamics of AWE aircraft. In contrast, the RANS approximation was extensively applied to 2D and 3D cases to investigate the particular aerodynamic characteristics of different types of kites (see Section 1.2.2). Most of the 2D works generated steady CFD databases to be queried by other lower-fidelity aerodynamic models such as nonlinear vortex-step methods (Leloup *et al.* 2013; Bosch *et al.* 2014; Breukels *et al.* 2013; Damiani *et al.* 2019; Candade *et al.* 2020*b*; Cayon *et al.* 2023). This is particularly useful for fixed-wing and LEI kites since they present thick and virtually uniform airfoils. Other works focused on the flow physics of specific types of airfoils. For instance, Folkersma *et al.* (2019) investigated the effect of laminar to turbulent transition on LEI airfoils with the open-source tool OpenFOAM. They applied the $\gamma - \widetilde{Re}_{\theta t}$ transition model along with the $k-\omega$ shear stress transport (SST) turbulence model and concluded that transition is relevant for $Re < 5 \times 10^6$. However, such a transition model relies on empirical correlations and important features of the woven membrane that may trip the transition were not taken into account. Moreover, a parametric study of a multi-element airfoil applied to AWE was performed through OpenFOAM set with RANS equations closed by the Spalart-Allmaras model (De Fezza & Barber 2022). No significant differences between the latter and the $k-\omega$ SST turbulence model were noticed. A similar multi-element airfoil was optimized by using the viscous-inviscid interaction MSES code (Ko *et al.* 2023). Further comparisons between MSES and OpenFOAM (RANS) revealed a significant underprediction of the airfoil drag by the former.

Three-dimensional RANS analyses are more scarce than bi-dimensional ones in the literature. Among the first studies on AWE, the steady-state aerodynamic characteristics

of curved kites with an uniform NACA 64-418 sectional shape were obtained by using the in-house CFD tool EllipSys3D (Gaunaa *et al.* 2011). A C-type wing with a double membrane was analyzed with CFD (Buffoni *et al.* 2014) to obtain a database of aerodynamic force and moment coefficients versus the angle of attack and the airspeed. With the same purpose, the flow past a LEI kite was solved with OpenFOAM for a range of angles of attack and Reynolds number (Viré *et al.* 2020). This work, that did take into account 3D effects, confirmed most of the 2D flow features of LEI airfoils discovered in Folkersma *et al.* (2019). An extension of this work studied the effect of chordwise struts and flow misalignment (sideslip angle) by using the same model (Viré *et al.* 2022).

Obtaining CFD databases is a very efficient way of using high-fidelity tools because the computations are carried out only once. However, the validity of these databases is limited to rigid and steady-state cases. For instance, Ref. Folkersma *et al.* (2020) performed a two-way coupling between a finite-element structural model and steady-state RANS aerodynamics (OpenFOAM) for a ram-air kite. Unavoidably, the aerodynamics was resolved in every aeroelastic iteration. Likewise, unsteady RANS were necessary in a fluid-structure interaction analysis of a multi-megawatt fixed-wing AWE aircraft (Pynaert *et al.* 2023). They considered the aircraft immersed in the full wind window ($620 \times 620 \times 100$ m^3) performing a circular trajectory with constant absolute velocity and a logarithm wind-shear profile. The latter caused periodic variations in the angle of attack and, consequently, in the longitudinal aerodynamic coefficients highlighting the importance of considering realistic kinematics between the body and wind reference frames.

This thesis used the open-source code SU2 (Palacios *et al.* 2013, 2014; Economon *et al.* 2016) to solve the unsteady RANS equations closed with the $k-\omega$ SST turbulence model. Apart from the CFD solvers, the SU2 suite has additional fluid-structure frameworks ready to be used for future extensions of the present work. This tool is used with the aim of uncovering relevant unsteady viscous aerodynamic phenomena during the crosswind flight of the RFD kite that are not captured by other lower-fidelity methods in Paper 2 of Chapter 2.

1.3. Dynamic stall phenomenon

Stall in airfoils and wings is a sudden reduction of lift when a critical angle of attack (stall angle of attack) is exceeded. This conventional stall is normally triggered by flow reversal that induces flow separation on the aerodynamic surface. On the other hand, the dynamic stall is a periodic unsteady phenomenon that involves separation and re-attachment of the flow during imposed or free oscillations in the angle of attack (Ham & Garelick 1968; Ham 1968; Carr 1988). It presents the following features: (i) stall delay reaching a higher lift without stalling; (ii) periodic formation and shedding of a leading-edge vortex and (iii) flow re-attachment if the angle of attack diminishes sufficiently. Figure 1.4 depicts the typical five stages in dynamic stall along with the longitudinal aerodynamic coefficients (lift, pitch moment and drag) versus the angle of attack (Pereira 2020). The phenomenon is characterized by a hysteresis behavior in the three curves, i.e., the instantaneous angle of attack does not identify a single value of the coefficients (like in the static case) but two that depend on the angle of attack history. The characteristics of such hysteresis cycles generally depend on the frequency and amplitude of the oscillations.

Motivated by the occurrence of this phenomenon in helicopter and wind turbine blades, among others, dynamic stall was experimentally characterized for several airfoil sections

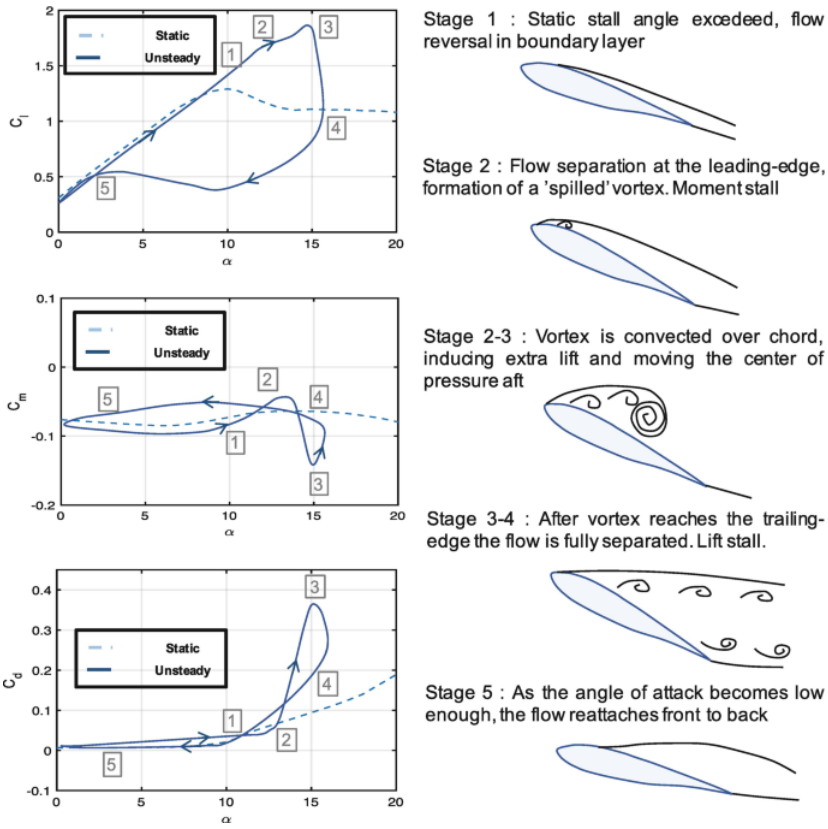

Figure 1.4: Lift, pitch moment and drag coefficients versus the angle of attack (left column) and typical stages (right column) of the dynamic stall phenomenon. Source: Pereira (2020).

in the three volumes released by NASA (McCroskey *et al.* 1982; McAlister *et al.* 1982; Carr *et al.* 1982). Additionally, much research effort was put on the numerical side to better understand the unsteady flow of two-dimensional (Ekaterinaris & Platzer 1997) and three-dimensional (Spentzos *et al.* 2007) dynamic stall. The latter highlighted the strong interaction between leading-edge and tip vortices for most of the studied planforms. Likewise, work Gad-el Hak & Ho (1985) observed a significant interaction between the leading-edge vortices inherently shed by a delta wing and those shed during dynamic stall. Within the complexity of dynamic stall, the leading-edge vortex mechanisms and modeling remain to be an open field of research. In fact, a comprehensive literature review of the field was recently presented in Eldredge & Jones (2019).

After understanding the phenomenology associated to dynamic stall, a novel category of methods named semi-empirical dynamic stall models were developed. They obtain the best of experimental and numerical methods by combining them. Among the first methods, the ONERA model due to Tran and Petrot (Tran & Petot 1980) and the Leishman-Beddoes model due to Leishman and Beddoes (Leishman & Beddoes 1989) stood out from the

rest due to their remarkable physical representation. These two methods consist of an attached-flow (potential flow) module and a phenomenological module. The latter has free empirical parameters that must be fined tuned with high-fidelity data coming from experiments or simulations. The Leishman-Beddoes model suffered several modifications to allow for higher Mach numbers (Sheng *et al.* 2012), and lower Mach and Reynolds numbers (Boutet *et al.* 2020). Additionally, Ref. Hansen *et al.* (2004) considered the unsteady effects in the aerodynamic coefficients as variations about the steady values improving the match between the model and the empirical data.

A semi-empirical dynamic stall model based on the original Leishman-Beddoes model after modifications by Boutet *et al.* (2020) and Hansen *et al.* (2004) is proposed in this work. The model combines our in-house potential-flow tool UnPaM with a phenomenological dynamic stall module that is fine tuned with data from the CFD tool SU2. The results from this tool are presented in Paper 2 of Chapter 2. Figure 1.5 shows the complete multi-fidelity aerodynamic framework used in this thesis to investigate the unsteady aerodynamics of the RFD kite.

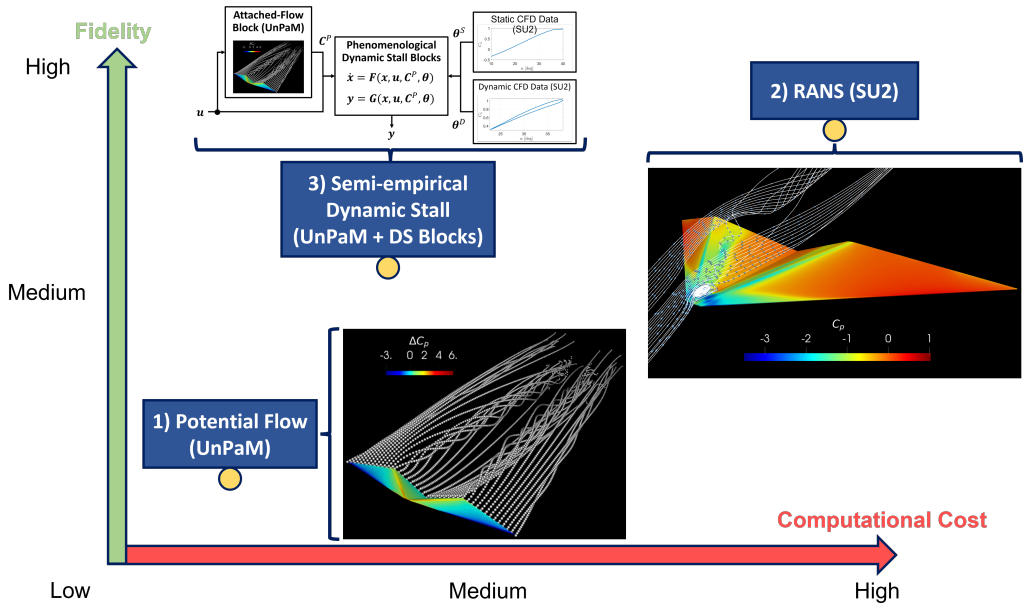

Figure 1.5: Multi-fidelity aerodynamic framework of this thesis. 1) unsteady VLM within the UnPaM suite, 2) unsteady RANS equations with the $k-\omega$ SST turbulence model within SU2 and 3) combination of 1) and 2) in a semi-empirical dynamic stall model.

1.4. Airborne wind energy machines and testbeds

This section provides a literature review of AWE experimental setups with the goal of introducing the testbed and flight test campaign presented in Paper 3 of Chapter 2. An overview of AWE infrastructures is first presented followed by a state of the art in estimation techniques, dynamics and control in AWE.

1.4.1. Overview of AWE infrastructures

A large variety of AWE concepts have arisen since the beginning of the 21st century. One of the first patented concepts was the laddermill, a closed loop composed of multiple tethered wings moving upward or downward, proposed by the first Dutch astronaut Wubbo Ockels (Ockels 2001). A recent classification of AWE technologies is shown in Figure 1.6 (Schmehl 2019). AWE systems are first divided depending on the type of electricity generation method (with fixed ground station (GS), with moving GS and on flying device). Each may be split into three flight modes (crosswind, tether-aligned and rotational). The crosswind and tether-aligned modes were already discussed in the pioneering work of Loyd's (Loyd 1980). The rotational mode consists in transferring the aerodynamic torque of an airborne rotor-blade configuration to a generator. The main past and current prototypes are also gathered on the right-hand side of each architecture. The majority of them chose crosswind flight due to its inherent power production advantage. Companies like Kitemill, TwingTec, EnerKíte and KiteKraft, among others, have already tested their proof-of-concept designs and are up-scaling their systems. Others like Kitepower and SkySails Power have their ~ 100 kW machines ready or close to be commercialized.

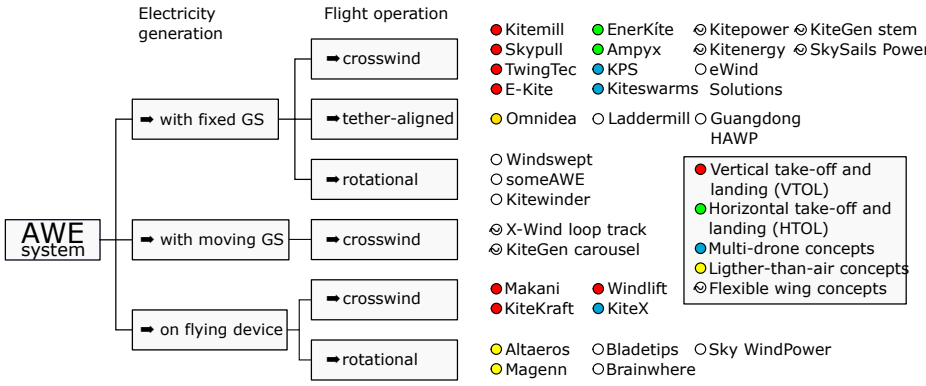

Figure 1.6: Classification of AWE technologies. Source: Schmehl (2019).

Since the beginning of AWE development and simultaneously to fully operational machines, small-scale prototypes and testbeds were prepared to study relevant topics for AWE including dynamics, control, estimation and aerodynamics through flight testing. Among the first technology demonstrators, a 20 kW system by Kitepower (van der Vlugt *et al.* 2013) and a 60 kW Yo-Yo AWE generator by Kitenergy (Milanese *et al.* 2013) showed the feasibility of pumping-cycle operation in AWE systems. A small-scale AWE prototype for two- and three-line kites was designed and manufactured by Prof. Fagiano and co-workers at the University of California, Santa Barbara (US) (Fagiano & Marks 2015). Despite the prototype was not aimed at energy generation, this platform enabled fruitful research regarding sensor fusion and estimation (Fagiano *et al.* 2014*a*), control characterization of membrane wings (Fagiano *et al.* 2014*b*), data-driven control approaches (Fagiano & Novara 2014), active pitch control to maximize the traction force (Buffoni *et al.* 2014) and real-time optimizations (Zgraggen *et al.* 2015).

Realistic and repeatable wind conditions to fly tethered kites were reproduced through towing test units, i.e., testbeds towed by a truck moving in straight paths, at the Technical University of Berlin (Germany) (Hummel *et al.* 2019) and the Kyushu University (Japan) (Rushdi *et al.* 2020). Both works effectively characterized the dynamics of small membrane wings (< 10 m^2) which becomes an essential task for the validation of numerical models. Other studies relied on the capability of rotating platforms to mimic static and dynamic flight conditions in the laboratory. For instance, Healy *et al.* (2022) built a novel pendulum-like testbed to test the dynamics of a commercial aircraft prototype equipped with folding wingtips. This work demonstrates that tethered flight testing is not only relevant for the AWE community but other fields may also benefit from it. Likewise, a carousel-like testbed proved to be an effective indoor infrastructure for circular launch and recovery testing (Geebelen *et al.* 2013). Takeoff and landing were and remain to be important technical challenges for unpropelled tethered airplanes. For that reason, a small-scale testbed was built to study the takeoff of tethered aircraft in compact space (Fagiano *et al.* 2017*a*,*b*, 2018).

A key feature of any of the described testbeds is the electro-mechanical actuation capability to achieve automatic steering (lateral-directional) and reel-in/reel-out (tether length) control. With that purpose, this thesis builds upon the former UC3M AWE testbed developed in Borobia *et al.* (2018) and Borobia-Moreno *et al.* (2021) by replacing the manual control bar with an automatic ground control unit (GCU) based on a linear actuator and a winch as shown in Figure 1.7. These modifications were performed in collaboration with an industrial PhD being developed at UC3M, whose objective is to convert the testbed into an AWE machine prototype. The global navigation satellite system (GNSS) receivers and the wind station were upgraded. Moreover, the testbed was equipped with a novel visual sensor (bottom of Figure 1.7). These changes enhanced the control and estimation capabilities of the testbed that naturally led to a more accurate aerodynamic, dynamic and control characterization of our AWE system. The testbed and a flight test campaign are fully described in Paper 3 of Chapter 2.

1.4.2. Estimation techniques

Accurate state estimation (also known as filtering) becomes essential for the control and operation of AWE systems. Any guidance, navigation and control system in AWE requires good estimates (in a statistical sense) of the state vector of the kite, the tether(s) and the environment. Several estimation techniques like moving horizon estimation (Geebelen *et al.* 2013) and recursive least squares (Cobb *et al.* 2020) were explored in the AWE field. Due to its extensive use for aerospace applications, the extended Kalman filter (EKF), which considers nonlinear processes, was mostly applied. An EKF essentially consists of an observation and a process model (Simon 2006). The former needs measurements from several sensors and relates these with the state vector being estimated. The process model describes how the state vector evolves over time. Among the many existing models, purely kinematic processes were employed to avoid prior knowledge of aircraft's geometric, inertial and aerodynamic properties (Fagiano *et al.* 2014*a*; Millane *et al.* 2015). Moreover, Ref. Millane *et al.* (2015) applied a multiplicative version of the EKF to avoid singularities introduced by the quaternions in the covariance matrix. Aerodynamic variables such as the aerodynamic force and moment about the kite center of mass were included in the state vector of an EKF with dynamic Schmidt *et al.* (2020) and stochastic (Gauss-Markov) Borobia-Moreno *et al.* (2021) processes. Some of these estimators were adapted to

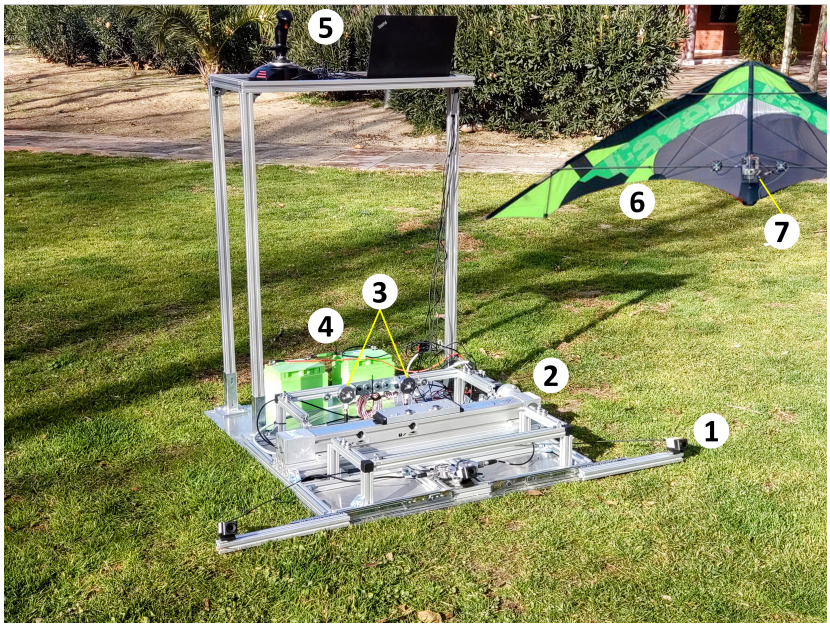

Figure 1.7: Ground control unit and RFD kite of the testbed. ① three-camera system, ② linear actuator, ③ load cells (replaced by a motorized winch in the *winch configuration*), ④ batteries, ⑤ control joystick and laptop, ⑥ RFD kite and ⑦ avionics.

include tether constraints by measuring the tether length to further correct the estimations (Fagiano *et al.* 2014*a*; Borobia *et al.* 2018; Schmidt *et al.* 2020; Borobia-Moreno *et al.* 2021).

Estimation involves the fusion of measurements from multiple onboard and on-ground sensors such as Inertial Measurement Units (IMU), barometers, magnetometers, GNSS receivers, anemometers, load cells, line angle sensors, etc (van der Vlugt *et al.* 2013; Milanese *et al.* 2013; Fagiano *et al.* 2014*a*; Borobia *et al.* 2018). Despite its robustness, line angle sensors proved inaccurate as compared to range-inertial sensors in a numerical study due to the presence of tether sagging and dynamics (Millane *et al.* 2015). All these sensors allow, among others, for the reconstruction of the full kinematic state of the kite (position, attitude, linear and angular rates), tether forces and direction, and wind speed and direction Borobia *et al.* (2018).

Regarding aerodynamic variables, the angle of attack and the lift and drag coefficients were estimated by solely using on-ground sensors (Schmidt *et al.* 2020). However, to reduce uncertainties in the so-called aerodynamic velocity vector, in-situ measurements of the apparent wind becomes essential. For that reason, Oehler & Schmehl (2019) designed and manufactured a system composed of vanes and a pitot tube to be attached close to the kite control pod of a LEI kite. The raw data from the vanes rotary encoders and pitot pressure sensors were post-processed to find the aerodynamic velocity vector and characterize the aerodynamics of a soft kite. Further progress was achieved by boarding a multi-hole pitot tube located at the tip of a boom attached to the central spine of LEI

and RFD kites Borobia-Moreno *et al.* (2021). A more direct and accurate measurement of the angle of attack, sideslip angle and airspeed was obtained thanks to its positioning on the kite and compact (no moving parts) design.

Visual sensors have not received much attention in the AWE field. In particular, Visual Motion Tracking (VMT) systems become a reliable and drift-free source of data independent of onboard measurements such as IMU and GNSS. Therefore, VMT systems could work in combination with onboard sensors or as a backup for them. In fact, a single-camera VMT system was able to track the kite position by combining accurate object detection and fast motion tracking algorithms (Hesse *et al.* 2018). However, this object detector required human intervention by selecting a sub-image containing the kite at the beginning of the tracking process or if the kite left the camera image. The carousel-like laboratory testbed in Geebelen *et al.* (2013) included a two-camera stereo vision system to reconstruct the position and attitude of the tethered kite. In other fields, it has been demonstrated that machine learning algorithms like neural networks have a favourable effect on the detection capabilities of VMT systems by avoiding human intervention Smolyanskiy *et al.* (2018); Shahzad *et al.* (2020). For this reason, this thesis proposes a novel VMT system based on three cameras (bottom of Figure 1.7) and an artificial neural network to enhance the robustness of the estimations. It was demonstrated that the use of three independent cameras became necessary for continuous (99.9% of the time) detection of the kite by the algorithm.

1.4.3. Dynamics and control of AWE systems

Unlike conventional wind turbines, AWE systems are multi-degree-of-freedom dynamical systems where control is essential for the autonomous operation. Their dynamics and control have been deeply explored through simulations and experiments since the beginning of AWE development (Vermillion *et al.* 2021). The simplest dynamic models but rather effective for control purposes were based on a point mass under a quasi-steady assumption (Erhard & Strauch 2015) and without such an assumption (Cobb *et al.* 2020). Higher degree-of-freedom models considered the typical six degrees of freedom of the aircraft, tether models at different levels of approximation and winch models, among others, (Fechner *et al.* 2015; Williams 2017; Eijkelhof & Schmehl 2022). The latter were based on classical (Newtonian) mechanics which naturally led to non-minimal coordinates. However, minimal coordinates can be achieved through analytical mechanics yielding more efficient flight simulators (Gros & Diehl 2013). Lagrangian mechanics was successfully applied to one-line, two-line and multi-kite AWE systems and gathered in the open-source software LAKSA (Sánchez-Arriaga *et al.* 2017; Sánchez-arriaga *et al.* 2019; Sánchez-Arriaga *et al.* 2021). Unavoidably, all these flight simulators need efficient and accurate aerodynamic models to obtain good predictions.

The main concern of control of AWE systems is to follow reference trajectories such as figure-of-eight and circular patterns which are crosswind and, therefore, produce more energy than steady flight. Among the many existing control strategies, linear proportional-integral (PI) controllers (Fechner *et al.* 2015), nonlinear model predictive control (Gros *et al.* 2013) and control through reinforcement learning (Orzan *et al.* 2023), among others, were numerically studied. Optimal control problems, whose objective is to maximize the power output by optimizing certain design variables, soon started playing a major role in AWE. For instance, a comprehensive optimal control computational framework for single- and multi-aircraft AWE systems was presented in De Schutter *et al.* (2023).

Due to the periodic nature of AWE trajectories, the frequency-domain harmonic balance method was applied for the first time to fly-gen AWE systems (Trevisi *et al.* 2022). Besides trajectory optimal control (Cobb *et al.* 2020; Manuel C. R. M. Fernandes & Fontes 2021), the operational altitude and the reeling speed of pumping kites were optimized in Baheri *et al.* (2017) and Berra & Fagiano (2021), respectively.

The lateral-directional control is performed differently depending on the type of AWE system (see Figure 1.6). For instance, fixed-wing aircraft may use aerodynamic control surfaces while LEI kites are steered either from a hanging control pod or from a ground control unit by differential tether length ΔL. Focusing on the ΔL steering, pioneering studies like Baayen & Ockels (2012) proposed the use of the turning angle γ as a one-dimensional representation of the kite trajectory. This turning angle, which is the angle between the local north (on a virtual sphere with center in the AWE ground station and radius the tether length) and the kite absolute velocity vector, was subsequently denoted by course and velocity angle. It has been extensively used as a feedback control variable in real systems within linear proportional-integral-derivative (PID) controllers (van der Vlugt *et al.* 2013; Milanese *et al.* 2013; Erhard & Strauch 2015). These controllers compare the current course angle with a reference value provided by a navigation module and decide on the steering input to the kite.

Important insights into the control characteristics of soft wings were obtained in Fagiano *et al.* (2014*b*) and Wood *et al.* (2015). Ref. Fagiano *et al.* (2014*b*) proposed a simplified turning law that related the time derivative of the course angle $\dot{\gamma}$ with the steering input ΔL through a proportional gain. The experimental results showed a remarkable correlation between these two variables. In fact, this correlation was further improved in Wood *et al.* (2015) by introducing a steering time delay in such a way that the cause of the turn (ΔL) was delayed with respect to the effect ($\dot{\gamma}$). Both works used the derived turning laws for feedback controller design. In this regard, this thesis paves the way toward closed-loop control of semi-rigid kites by characterizing the control of the UC3M RFD kite by using a methodology similar to works Fagiano *et al.* (2014*b*) and Wood *et al.* (2015). The kite was steered with the new GCU in open loop (Figure 1.7) to perform several figure-of-eight maneuvers. The same turning law as in Wood *et al.* (2015) and an additional one relating $\dot{\gamma}$ with the differential tether tension ΔT were proposed with the latter resulting in a better correlation.

Chapter 2

Scientific journal publications

Summary of the papers

Paper 1

Three-Dimensional Unsteady Aerodynamic Analysis of a Rigid-Framed Delta Kite applied to Airborne Wind Energy

The validity of using a low-computational-cost model for the aerodynamic characterization of Airborne Wind Energy Systems was studied by benchmarking a three-dimensional unsteady panel method (UnPaM) with experimental data from a flight test campaign of a two-line rigid-framed delta kite. The latter, and a subsequent analysis of the experimental data, provided the evolution of the tether tensions, the full kinematic state of the kite (aerodynamic velocity and angular velocity vectors, among others), and its aerodynamic coefficients. The history of the kinematic state was used as input for UnPaM that provided a set of theoretical aerodynamic coefficients. Disparate conclusions were found when comparing the experimental and theoretical aerodynamic coefficients. For a wide range of angles of attack and sideslip angles, the agreement in the lift and lateral force coefficients was good and moderate, respectively, considering UnPaM is a potential flow tool. As expected, UnPaM predicts a much lower drag because it ignores viscous and separation effects. The comparison of the aerodynamic torque coefficients is more delicate due to uncertainties on the experimental data. Besides fully non-stationary simulations, the lift coefficient was also studied with UnPaM by assuming quasi-steady and steady conditions. It was found that for a typical figure-of-eight trajectory there are no significant differences between unsteady and quasi-steady approaches allowing for fast simulations.

Paper 2

Unsteady Aerodynamics of Delta Kites for Airborne Wind Energy under Dynamic Stall Conditions

Three unsteady aerodynamic tools at different levels of fidelity and computational cost were used to investigate the unsteady aerodynamic behavior of a delta kite applied to airborne wind energy. The first tool is an in-house unsteady panel method that is fast but delivers low- to mid-fidelity predictions. The second tool uses the open-source CFD code SU2 to solve the unsteady Reynolds-averaged Navier-Stokes equations with the $k-\omega$ SST turbulence model. At an intermediate level of fidelity, a semi-empirical dynamic stall model that combines the panel method with a phenomenological dynamic stall module is proposed. The latter has free parameters that are fine-tuned with CFD results from the second tool. The research on the dynamic stall model has been inspired by two flight test campaigns suggesting dynamic stall phenomena possibly driven by the periodic variation of the angle of attack (aerodynamic pitching motion) during crosswind maneuvers. The recorded inflow along the flight path was prescribed in the three aerodynamic tools. As expected, the price to pay for the low computational cost of the panel method is its inability to capture the dynamic stall phenomenon. The results from unsteady CFD

qualitatively matched the experimental data identifying a leading-edge vortex that forms and detaches cyclically during the pitching motion. Using RANS data, the semi-empirical tool was fined-tuned to reproduce the dynamic stall behavior, becoming an accurate and fast aerodynamic tool for coupling with any kite flight simulator. Further discussions on the effects of kite aerostructural deflections are included.

Paper 3

Automatic Testbed with a Visual Motion Tracking System for Airborne Wind Energy Applications

The architecture and a flight test campaign of a small-scale testbed aimed at aerodynamic and dynamic characterization of airborne wind energy systems are presented. The testbed involves a two-line rigid-framed delta kite and an automatic ground station for the lateral control of the kite and reel-in/reel-out of the two tethers. The environment, and the states of the kite, the tethers and the actuators are measured by a set of on-ground and onboard sensors that include, among others, an inertial measurement unit, GNSS receivers, load cells, actuator encoders, a weather station, and a visual motion tracking (VMT) system based on three cameras and an artificial neural network (YOLOv2). The results of a five-minute flight, including the take-off, crosswind flight, and landing, were used to analyze the capabilities of the testbed. It was shown that the time derivative of the kite course angle exhibits a linear correlation with both the delayed steering input and the delayed differential tether tension, being the dispersion lower for the latter. The intrinsic and extrinsic calibrations proposed for the VMT system led to a good agreement between the estimation of the kite position and course angle provided by the VMT system and the onboard computer. Moreover, although the YOLOv2 algorithm failed in the detection of the kite within around 5% of the images, the simultaneous non-detection from the three cameras was below 0.1% during the full flight. Such a reliability suggests that a VMT system can be used as a redundant or backup sensor for the GNSS.

1

Paper 1

Three-Dimensional Unsteady Aerodynamic Analysis of a Rigid-Framed Delta Kite applied to Airborne Wind Energy

I. Castro-Fernández [1], R. Borobia-Moreno [2], R. Cavallaro [1] & G. Sánchez-Arriaga [1]

[1] Departamento de Bioingeniería e Ingeniería Aeroespacial, Universidad Carlos III de Madrid, Leganés, 28911 Madrid, Spain

[2] Centro de Experimentación de "El Arenosillo" (CEDEA), Instituto Nacional de Técnica Aeroespacial, Mazagón, 21130 Huelva, Spain

Energies (2021), vol. **14(23)** (8080)

The validity of using a low-computational-cost model for the aerodynamic characterization of Airborne Wind Energy Systems was studied by benchmarking a three-dimensional unsteady panel method (UnPaM) with experimental data from a flight test campaign of a two-line rigid-framed delta kite. The latter, and a subsequent analysis of the experimental data, provided the evolution of the tether tensions, the full kinematic state of the kite (aerodynamic velocity and angular velocity vectors, among others), and its aerodynamic coefficients. The history of the kinematic state was used as input for UnPaM that provided a set of theoretical aerodynamic coefficients. Disparate conclusions were found when comparing the experimental and theoretical aerodynamic coefficients. For a wide range of angles of attack and sideslip angles, the agreement in the lift and lateral force coefficients was good and moderate, respectively, considering UnPaM is a potential-flow tool. As expected, UnPaM predicts a much lower drag because it ignores viscous and separation effects. The comparison of the aerodynamic torque coefficients is more delicate due to uncertainties on the experimental data. Besides fully non-stationary simulations, the lift coefficient was also studied with UnPaM by assuming quasi-steady and steady conditions. It was found that for a typical figure-of-eight trajectory there are no significant differences between unsteady and quasi-steady approaches allowing for fast simulations.

Keywords: Aerodynamic coefficients; airborne wind energy system; estimation before modeling; vortex lattice method

---

1. Introduction

Airborne wind energy (AWE) systems constitute a relatively recent technology to harvest energy and produce traction from high-altitude winds. Important technological and theoretical progress led to the introduction of some prototypes in a pre-commercial phase (Ecorys 2018). Being AWE systems operated airborne, with an aircraft linked to the ground by a tether, aerodynamics is one of its critical areas. Whether the generation happens on the ground (ground generation) or onboard the aircraft (fly generation), a good aerodynamic characterization is important for the design, control, and optimization

of these systems. For this reason, AWE community dedicated an important effort to develop aerodynamic models for particular AWE machines (Vimalakanthan *et al.* 2018; Malz *et al.* 2019; Mehr *et al.* 2020; Wijnja *et al.* 2018; Viré *et al.* 2020; Ali & Kim 2020; Saleem & Kim 2020) and also to prepare numerical tools and experimental setups to study the plethora of AWE aircraft, which includes different types of kites and rigid wings (Cherubini *et al.* 2015; Vermillion *et al.* 2021; Licitra *et al.* 2017, 2019).

Due to their importance for AWE applications, previous numerical works on aerodynamics and aeroelasticity were mainly focused on leading-edge inflatable (LEI) and ram-air kites. Computational cost and model fidelity were the main drivers on the selection of the numerical methods. For instance, low-cost models such as a quasi-steady multiple-wake vortex lattice method (VLM) have been applied to LEI kites and highlighted the importance of the position of the separation points of the flow (Leuthold 2015). Aeroelastic analysis on LEI and ram-air kites (Candade *et al.* 2020*a*,*b*) also used a quasi-steady three-dimensional VLM that allows modifications of the boundary conditions to include non-linear airfoil aerodynamic data from external databases (Ranneberg 2015). Reduced order modeling techniques for the aerostructural optimization of morphing wings for AWE applications also used 3D steady VLM (Fasel *et al.* 2017, 2019). Steady Reynolds-averaged Navier–Stokes (RANS) simulations were also used to study LEI kites in 2D (Folkersma *et al.* 2019) and 3D (Viré *et al.* 2020), and fluid structure interaction problems in 2D (Bosch *et al.* 2014; Breukels *et al.* 2013). A 2D interactive boundary-layer approach was also proposed for a ram-air kite (Thedens *et al.* 2019). To the best of the author's knowledge, no previous works on 3D unsteady potential aerodynamics applied to RFD kites exist in the literature.

Concurrently with the numerical work, experimental setups have also been developed to acquire real flight data and find from them the aerodynamic characteristics of the kites. Pioneer works on sensor fusion and estimation were mostly targeted to kite control (Fagiano *et al.* 2014*a*; Hesse *et al.* 2018) and used onboard global navigation satellite system (GNSS) receivers, line angle sensors, cameras, inertial measurement units (IMU), and magnetometers, among others. The aerodynamic efficiency and the lift coefficient as a function of the ratio between power and steering lines were obtained for LEI and ram-air kites (Hummel *et al.* 2019). However, obtaining a full and reliable aerodynamic model requires the direct measurement of the aerodynamic velocity vector, i.e., its modulus, and the angle of attack and sideslip angle of the kite. For this reason, vanes attached to the bridle of the kite were incorporated to the test bench and helped to uncover the importance of the aerodynamic loading on the aerodynamic characteristics due to the kite deformation (Oehler & Schmehl 2019). Estimation Before Modeling Techniques, a method largely used in the aerospace industry (Hoff & Cook 1996), was also proposed to obtain the aerodynamic model of LEI and rigid-framed delta (RFD) kites in a systematic manner (Borobia-Moreno *et al.* 2021). The authors proposed an extended Kalman filter for AWE systems that incorporates the aerodynamic force and torque into the state vector (Borobia *et al.* 2018) and added to the experimental setup a multi-hole pitot tube for the in situ and accurate measurement of the full aerodynamic velocity vector. Key aerodynamic coefficients versus the angle of attack and the sideslip angle for the RFD kite studied in this work were obtained from the flight data acquired during multiple figure-of-eight trajectories (Borobia-Moreno *et al.* 2021).

Among the multiple applications of such an experimental aerodynamic model of the RFD kite, we focus here on the exploration of the validity of using numerical methods

with a low computational cost on the aerodynamic modeling of AWE systems. This is a critical aspect for AWE flight simulators that have been specifically designed to remove the fast longitudinal oscillation of the tether to keep low the computational cost (see for instance (Sánchez-arriaga *et al.* 2019) and references therein). The coupling of these flight simulators with broad databases of aerodynamic coefficients generated with numerical methods or directly with low-cost numerical codes is a key application in AWE. In this work, an in-house 3D and unsteady VLM within the UnPaM suite (Cavallaro *et al.* 2015; Nardini 2014) has been adapted and used to predict the aerodynamic forces in the same flight conditions tested in Borobia-Moreno *et al.* (2021), and results have been compared. Such a combination of data helps in the validation of fast aerodynamic tools such as UnPaM and also provides interesting insights into the underlying aerodynamic phenomena. Moreover, unsteady effects, commonly ignored in previous numerical analyses in AWE systems, are here taken into account (within the assumption of potential flow) and assessed by means of comparison between steady, quasi-steady and unsteady modeling. Another novelty of the work is that the numerical analysis has been carried out using as kinematic input the experimental data of a maneuver that is relevant for AWE applications. The remainder of this article is organized as follows. Section 2 describes the methodology and tools used in this work. The comparison between the theoretical and the experimental aerodynamic models and the role of the unsteady effects are discussed in Sections 3 and 4, respectively. Section 5 presents the conclusions of the work, its limits, and suggests some future works that can contribute to further effectively model RFD kite aerodynamics.

2. Methodology

2.1. Flight test campaign

A previous work on an experimental AWE system (Borobia-Moreno *et al.* 2021) studied both LEI and RFD kites aerodynamics. The present work focuses on the same RFD kite (see Figure 1) and uses the experimental-based data obtained in Borobia-Moreno *et al.* (2021) through the Estimation Before Modeling technique. The reconstructed state vector of the kite along the crosswind trajectories included the kite position, ground speed, aerodynamic velocity vector, Euler angles, angular rates, and aerodynamic forces and moments. The experimental setup consisted of: (1) the two-line RFD kite equipped with onboard sensors: IMU, GNSS and an Aeroprobe$^{\text{TM}}$ micro air data system V2.0 composed of an onboard computer and a multi-hole pitot tube that was responsible for measuring the kite true airspeed (TAS), Angle of Attack (α), and sideslip angle (β); (2) a ground station for wind direction and magnitude measurements; and (3) load cells placed at each line of the kite to directly measure the tether tensions. The latter three sets of measurements constitute the observation model that, together with the process equation, constitute the discrete and continuous parts of the filter, respectively (more details are provided in Borobia *et al.* (2018); Borobia-Moreno *et al.* (2021)).

Table 1 shows the physical characteristics of the RFD kite. The numerical tool explained in Section 2.2 was fed with these data in order to assess the performances of the kite. Properties I_{x_B}, I_{y_B} and I_{z_B} represent the principal moments of inertia about the kite center of mass (CM). For convenience, we define the body axes with origin at the CM, x_B-axis along the spine of the kite, z_B-axis normal to it and contained in the plane of symmetry of the kite (pointing towards the anchoring point in normal flight conditions) and y_B-axis completing the right-handed frame. The body axes coincide with the principal

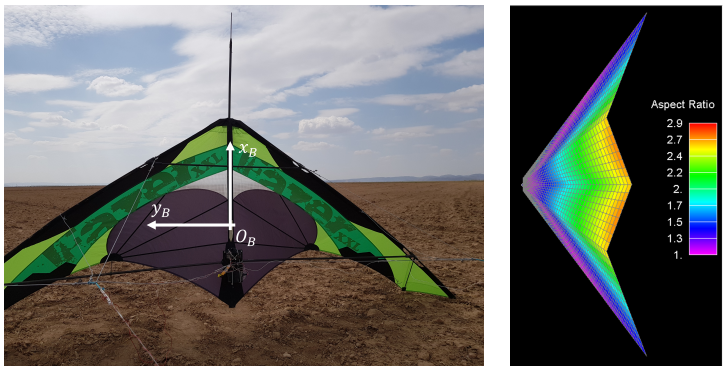

(**a**) (**b**)

Figure 1: (**a**) shows the RFD kite (HQ Fazer XXL) during the experimental campaign. (**b**) displays the aerodynamic mesh of the VLM model. The color bar represents the aspect ratio of the mesh panels.

axes of inertia. The chord (c) is defined as the mean aerodynamic chord of the RFD kite. The lines of the bridle meet at two points named $A^{\pm}$. Their coordinates in the body frame are $x_{A^{\pm}}$, $y_{A^{\pm}}$ and $z_{A^{\pm}}$. These last data have been revised by direct measurement with respect to the previous work (Borobia-Moreno *et al.* 2021). Additionally, tether length, total frontal area of the two tethers and typical values for the tether drag coefficient from refs. (Fechner *et al.* 2015; Fagiano *et al.* 2018) are provided.

Table 1: RFD kite physical characteristics.

Property	**Value**
Mass	2 kg
I_{x_B}	0.72 kg m^2
I_{y_B}	0.09 kg m^2
I_{z_B}	0.81 kg m^2
Surface (S)	1.86 m^2
Span (b)	3.60 m
Chord (c)	0.59 m
$x_{A^{\pm}}$	-0.07 m
$y_{A^{\pm}}$	± 0.73 m
$z_{A^{\pm}}$	1 m
Tether length	39.28 m
Tether frontal surface (S_t)	0.08 m^2
Tether drag coeff. (C_{d_t})	1

The trajectory selected in this work is a figure-of-eight. Using the methodology of Borobia-Moreno *et al.* (2021), the temporal evolution of any variable of interest versus time throughout this trajectory can be obtained, including the true aerodynamic speed, the tether tensions, the angle of attack, the sideslip angle, Euler angles, aerodynamic

coefficients, etc. For instance, Figure 2a,b show the orbit followed by the center of mass of the kite in one of these trajectories during the experimental campaign. The color corresponds to the magnitudes of the experimental true airspeed and the total tether tension (sum of the two tether tensions). For convenience, we used the Earth-fixed frame, that has origin at the anchoring point of the kite, x_E-axis and y_E-axis pointing toward the geographic north and east, respectively, and z_E-axis pointing downwards. As expected, the maximum aerodynamic velocities and tether tension are reached in the straight legs of the trajectory where, as shown in Figure 2c, the angle of attack reaches a minimum. The side slip angle (Figure 2d) changes its sign several times during the orbit and it is mainly an anti-symmetric function with respect to the plane of symmetry of the figure-of-eight. There is a good confidence about the quality of the estimation of these four magnitudes (TAS, tension, α, and β) because all of them are directly measured by the multi-hole pitot tube and the load cells, and their measurements were introduced in the observation model.

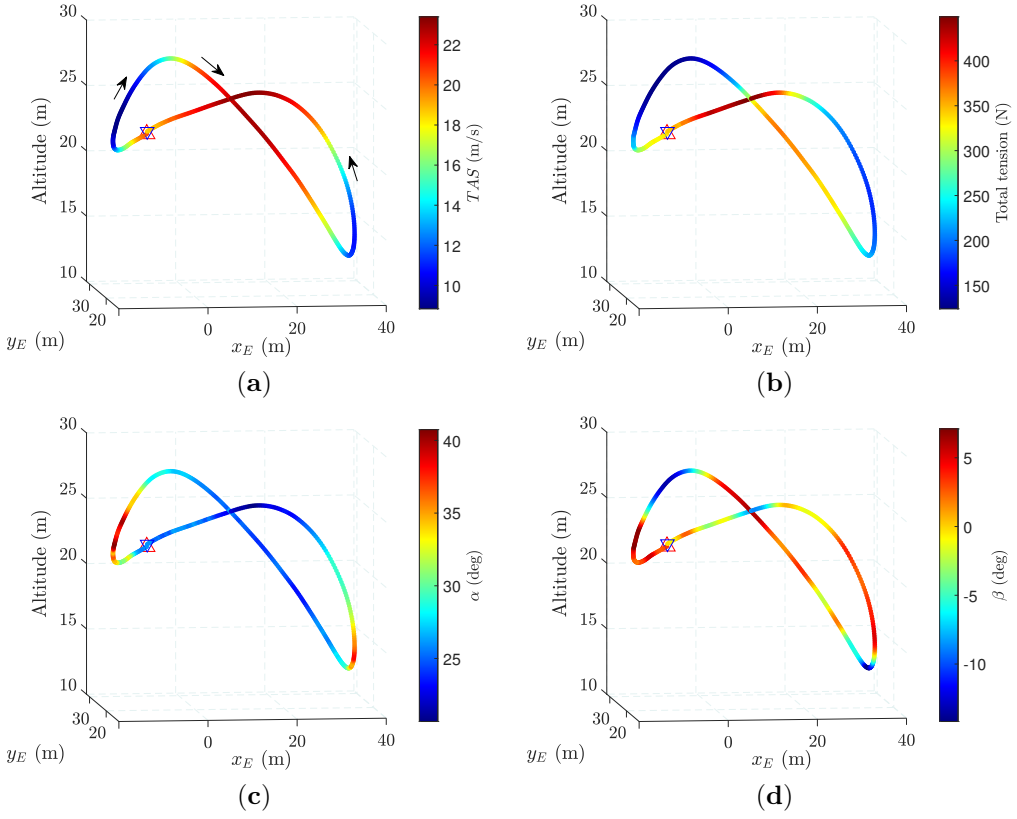

Figure 2: Trajectory of the kite in the selected maneuver. The color in (**a**–**d**) correspond to the true airspeed, the total tension on the two tethers, the angle of attack and the sideslip angle, respectively. The upward red triangle and the downward blue triangle are the starting and final points and the arrows in (**a**) show the direction of the kite motion.

2.2. In-house three-dimensional unsteady panel method (UnPaM)

UnPaM (Cavallaro *et al.* 2015; Nardini 2014) is a code capable of carrying out 3D aerodynamic simulations by using approaches based on the boundary element method. The flow field properties are described by singularities placed on the aerodynamic surface of the object and whose intensities are computed by imposing the boundary conditions. For incompressible flows, effects of unsteadiness concern the time-evolution of the circulation released in the wake and the time-dependent contribution in the momentum (Bernoulli's) equation (find more details in Section 2.2.3). For a correct modeling of the wake, its evolution must be tracked, which typically leads to the so-called 3D wake roll-up.

UnPaM can handle thick and thin (zero-thickness) aerodynamic surfaces. For thin surfaces, considered hereafter due to its inherent suitability to model the flat canopy of the RFD kite, the method becomes the VLM. This makes use of quadrilateral constant-strength vortex rings lying on the panel boundaries/segments. The collocation points, i.e., nodes where the boundary conditions must be fulfilled, are located at the panel centers. The boundary element method imposes the well-known boundary condition for an impenetrable boundary,

$$(\boldsymbol{v}_i + \boldsymbol{V}_i) \cdot \boldsymbol{n}_i = 0, \quad (i = 1 \dots N_b), \tag{1}$$

where $\boldsymbol{v}_i$ is the perturbation velocity vector induced by all the panels, including also wake panels, on the body panels. Vectors $\boldsymbol{V}_i$ and $\boldsymbol{n}_i$ are the external velocity vector, i.e., the local velocity of the air with respect to the kite, and normal vector to the panel at the collocation point i, which runs from 1 to the total number of body panels N_b. Since the perturbation velocity can be expressed as a superposition of the velocities induced by all the panels (body and wake), Equation (1) becomes a system of N_b linear algebraic equations with N_b unknowns that are the bound circulation strengths. When they are all gathered in the vector Γ, Equation (1) reads

$$\bar{\boldsymbol{A}}\boldsymbol{\Gamma} = -\bar{\boldsymbol{B}}\boldsymbol{\Gamma}^w - \boldsymbol{C}, \tag{2}$$

with $\bar{\boldsymbol{A}}$ and $\bar{\boldsymbol{B}}$ the aerodynamic influence coefficient matrices of the body and wake panels on the body collocation points (further details in Nardini (2014)) and the N_b components of vector $\boldsymbol{C}$ given by $\boldsymbol{C}_i = \boldsymbol{V}_i \cdot \boldsymbol{n}_i$.

The wake is shed from the trailing edge (TE) and grows in length as the simulation time-stepping advances. In our non-stationary computations, the wake grows until it reaches a maximum dimension defined a priori in the simulation setup. Afterwards, the oldest wake panels are not modeled any more. For a generic time step, the new wake row in the computational domain and shed by the TE has circulation intensity determined by the Kutta condition:

$$\boldsymbol{\Gamma}^w_{TE} = \boldsymbol{\Gamma}_{TE}, \tag{3}$$

with subscripts TE standing for trailing edge panels and superscript w indicating the first row of wake panels, i.e., the one immediately after the kite. This equation enforces no circulation on the TE and, consequently, no flow around the TE by just equating intensities of panels sharing the TE segments. The wake panels that have been shed previously retain the same circulation intensities. Along the time-stepping procedure, every wake panel will move in accordance with its corner points. Therefore, every corner point is displaced by multiplying the velocity induced by both the external conditions and the singularities over the body and wake by the simulation time step. To initialize the wake in the computational model used in this work, 10 time steps are carried out with

the kite at constant speed with no rotations. For further details of UnPaM's algorithm, a self-explanatory high-level flowchart of UnPaM is presented in Appendix A.

2.2.1. *Aerodynamic mesh*

The VLM requires a lattice-like mesh composed of flat panels (see Figure 1). The kite geometry was split into four surfaces, two of them on each side of the symmetry plane. Each of these surfaces was discretized using quadrilateral elements. To guarantee a high-quality mesh, the elements aspect ratio, i.e., the fraction between the sides of the panel was bounded below 3. Consequently, and since the four surfaces become tapered toward the leading edge (LE), a graded mesh was obtained. Figure 3 shows a convergence analysis by varying the number of panels and monitoring relevant aerodynamic outputs of the tool, such as the lift coefficient for steady conditions at $\alpha = 20°$ and $\beta = 0°$. Hereafter, we consider a mesh with 2080 panels because, as shown in Figure 3, it has a good balance between computational cost and accuracy. Its error for the C_L is less than 5% as compared with the finest mesh considered in Figure 3. For the selected mesh, the computational time for one time step in an unsteady simulation is in the order of a second.

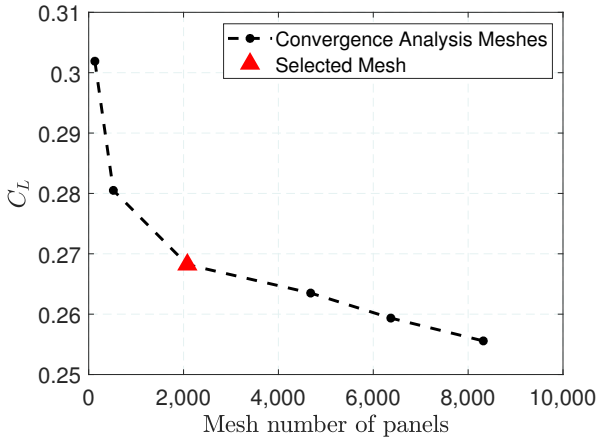

Figure 3: Mesh convergence analysis for steady conditions with $\alpha = 20°$ and $\beta = 0°$.

The correct implementation of the method was verified by considering a flat delta wing with an aspect ratio similar to the one of the RFD kite and comparing the results with previous works. Delta wing aerodynamic characteristics have long been of interest to the aerospace industry (Bartlett & Vidal 1955; Gursul 2004; Gray *et al.* 2003; Gordnier & Visbal 2004) and it is well-known that they develop leading edge vortices for low enough aspect ratio at high angles of attack. Among them, we verified that UnPaM was able to reproduce the lift coefficient versus angle of attack curve of Ref. Bartlett & Vidal (1955) and the aspect ratio of our RFD kite is not low enough to generate important leading edge vortices.

2.2.2. *Kinematic module of UnPaM*

UnPaM has a module that is used to prescribe any relative motion between the kite and the fluid. This module is purely kinematic and not dynamic, i.e., aerodynamic loads are computed as the result of the motion defined by the user. The two relevant frames of reference in the simulations are the wind (identified by index W) and the body (identified by index B) frames, both of them with origin at the center of mass of the kite. The former has the x_W-axis along the aerodynamic velocity vector whereas the z_W-axis lies on the plane of symmetry of the kite and points towards the ground in normal flight conditions. Axis y_w completes the right-handed frame. For convenience, we introduce a third frame, called the global frame (identified by index G), that has axes parallel to the wind frame and is at rest with respect to the computational box, i.e., everything else moves with respect to this frame. Therefore, the origin of the wind and the body frames move at the TAS along the x_G-axis.

The inputs of the kinematic module, which fully define the motion of the kite with respect to the fluid, are the true aerodynamic speed, the angle of attack, the sideslip angle, and their time derivatives ($\dot{\alpha}$, $\dot{\beta}$). All these quantities were mainly estimated by using the information of the multi-hole pitot tube onboard the kite in the experiments (Borobia-Moreno *et al.* 2021). In fact, this is one of the main advantages of this kinematic arrangement in the numerical simulations because it is mainly based on the measurements of the multi-hole pitot tube, which is a high accuracy instrument. The position of the center of mass of the kite are found from them by solving the kinematic relation

$$\frac{d\overline{O_G O_B}}{dt} = TAS\ \boldsymbol{i}_G, \tag{4}$$

with the initial condition $\overline{O_G O_B} = \mathbf{0}$. The attitude of the kite with respect to the fluid is given by the rotation matrix $\bar{R}_{WB}$ that relates vector components in the wind and the body frames

$$\begin{pmatrix} \boldsymbol{i}_W \\ \boldsymbol{j}_W \\ \boldsymbol{k}_W \end{pmatrix} = \bar{\boldsymbol{R}}_{WB} \begin{pmatrix} \boldsymbol{i}_B \\ \boldsymbol{j}_B \\ \boldsymbol{k}_B \end{pmatrix} \equiv \begin{pmatrix} \cos\alpha\cos\beta & -\sin\beta & \sin\alpha\cos\beta \\ \cos\alpha\sin\beta & \cos\beta & \sin\alpha\sin\beta \\ -\sin\alpha & 0 & \cos\alpha \end{pmatrix} \begin{pmatrix} \boldsymbol{i}_B \\ \boldsymbol{j}_B \\ \boldsymbol{k}_B \end{pmatrix} \tag{5}$$

and the angular velocity of the kite with respect to the fluid is

$$\boldsymbol{\omega}_{BG} = \boldsymbol{\omega}_{BW} = -\dot{\beta}\sin\alpha\ \boldsymbol{i}_B + \dot{\alpha}\ \boldsymbol{j}_B + \dot{\beta}\cos\alpha\ \boldsymbol{k}_B. \tag{6}$$

Figure 4 displays the kite and the wake at two different instants of a simulation. The three reference frames and the wake roll-up behind the kite are shown. Figure 4a corresponds to the 20^{th} time step in the simulation, when the kite has $\alpha = 26.1^{\text{o}}$ and $\beta = 2.7^{\text{o}}$ (definitions of α and β rotations in Figure 4a left). Figure 4b shows the 30th time step with $\alpha = 32.0^{\text{o}}$ and $\beta = 5.4^{\text{o}}$. Although the kite moves to the left, it never reaches an exit boundary because the computational box is infinitely long. However, the maximum size of wake is finite and prescribed by the user at the beginning of the simulation.

2.2.3. *Force and moment coefficients computation with UnPaM*

UnPaM computes the aerodynamic forces by summing up the contributions of all the segments of the panels. For segment j of panel i, the Kutta–Joukowski theorem states,

$$\boldsymbol{f}_{ij} = \rho\Gamma_i \boldsymbol{V}_{ij} \times \boldsymbol{l}_{ij}, \quad i = 1 \ldots N_p, \quad j = 1, \ldots 4, \tag{7}$$

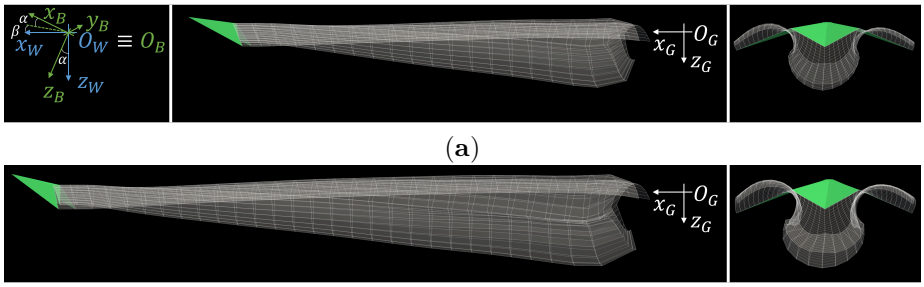

Figure 4: Reference frames and wake in an UnPaM unsteady simulation at the 20$^{\text{th}}$ (**a**) and 30th (**b**) times steps. Left image in (**a**) represents the B and W frames orientation (their origins are at the kite CM) on the $x_G - z_G$ plane at the 20$^{\text{th}}$ time step, center and right [left and right] images of (**a**) [**b**] show the $x_G - z_G$ plane and the $y_G - z_G$ plane, respectively.

where ρ is the air density, Γ_i the panel circulation, $\boldsymbol{V}_{ij}$ the aerodynamic velocity vector at the center of the segment and vector $\boldsymbol{l}_{ij}$ points in the direction of the segment circulation and has a magnitude equal to the segment length. The force acting on each panel ($\boldsymbol{f}_i$) is found from

$$\boldsymbol{f}_i = \sum_{j=1}^{4} \boldsymbol{f}_{ij} + \rho S_i \frac{\Gamma_i^k - \Gamma_i^{k-1}}{\Delta t} \boldsymbol{n}_i, \quad i = 1 \dots N_p, \tag{8}$$

where S_i and $\boldsymbol{n}_i$ are the panel area and the unit vector normal to the panel, respectively. Superscripts k and $k-1$ stand for actual and previous time steps, whereas Δt is the time step, which was kept constant during the simulation. The first and second term in Equation (8) correspond to the steady (or quasi-steady) and unsteady force components. The latter, which corresponds to a backward finite difference approximation of the time derivative, takes into account the temporal change of the panel circulation. The panel contribution to the total aerodynamic moment about the center of mass of the kite is

$$\boldsymbol{m}_i = \boldsymbol{r}_i \times \boldsymbol{f}_i, \quad i = 1 \dots N_p, \tag{9}$$

with $\boldsymbol{r}_i$ a vector with origin at the center of mass of the kite and tip at the center of the panel. Coefficients for drag (C_D), lateral (C_Y) and lift (C_L) forces together with those for roll (C_l), pitch (C_m) and yaw (C_n) moments, which are the quantities used in this work to compare experimental and theoretical results, are obtained by summing for all the panels and normalizing in the standard manner

$$(C_D, C_Y, C_L) = -\frac{2}{\rho V^2 S} \sum_{i}^{N_p} \boldsymbol{f}_i \cdot (\boldsymbol{i}_W, -\boldsymbol{j}_W, \boldsymbol{k}_W), \tag{10}$$

$$(C_l, C_m, C_n) = \frac{2}{\rho V^2 S} \sum_{i}^{N_p} \boldsymbol{m}_i \cdot \left(\frac{\boldsymbol{i}_B}{b}, \frac{\boldsymbol{j}_B}{c}, \frac{\boldsymbol{k}_B}{b} \right). \tag{11}$$

3. Comparison of numerical and experimental results

This section compares the force and moment coefficients predicted by UnPaM and the one obtained by feeding the extended Kalman filter with the data measured in the experimental campaign (Borobia-Moreno *et al.* 2021). The selected trajectory is the figure-of-eight shown in Figure 2. Figure 5 shows the six force and moment coefficients. Longitudinal (C_L, C_D, and C_m) and lateral-directional (C_Y, C_l, and C_n) coefficients are presented versus the angle of attack and the sideslip angle, respectively. Dots and crosses are used to show the results obtained from UnPaM and the experiments.

A good agreement was found for the lift coefficient C_L (Figure 5a), resulting in an average error of around 20% for the full trajectory. Interestingly, and although large values of the angle of attack are reached in the trajectory, the experimental results do not show the stall of the kite. Non-stationary effects have been suggested to explain this feature (Borobia-Moreno *et al.* 2021). Such a circumstance may explain why UnPaM, which is a potential-flow code with no flow separation, can reproduce reasonably well the experimental results for high angles of attack. It is also remarkable that the experimental C_L versus α curve exhibits two values of the C_L for the same angle of attack, whereas the dispersion of the values coming from the potential-flow theory is very small. This is the main cause of mismatch (20%), however, numerical data is centered between the two possible experimental values for every α. Moreover, the dispersion of the experimental C_L cannot be explained in terms of the different values of the sideslip angle reached by the kite in the trajectory, which also cover a small range (between $-15°$ and $8°$). A confirmation that the angle of attack is the main driver of the C_L is provided by Figure 6. It displays C_L versus β and shows a moderate agreement for the trend between the experimental and the numerical results and an average error of around 20%. This result reinforces the argument about the importance of non-stationary effects in RFD kites because there is hysteresis in the experimental $C_L - \alpha$ curve. Dynamic stall, which is a phenomenon that is not captured by the potential-flow code, is a candidate to explain it.

The experimental drag coefficient shown in Figure 5c also exhibits hysteresis. For a fair comparison, the tether drag (D_t) incorrectly attributed to the kite in Borobia-Moreno *et al.* (2021) has been subtracted from the total experimental drag following an overestimated approximation given in Equation (12). As expected, UnPaM, as a potential-flow tool, captures relatively well the drag only for small angles of attack but, in general, the code underestimates C_D. This mismatch is explained by the fact that UnPaM does not include viscous effects and flow separation. As a result, a large difference between the numerical and experimental drag results exist for large angles of attack. The lateral force coefficient in Figure 5b shows a moderate match in trend between the experimental and the numerical results. However, dispersion exhibited by the experimental C_Y is not properly captured by the numerical tool probably due to span-wise complex separation phenomena. Interestingly, the figure-of-eight maneuver was carried out with a bias of around $5°$ in β, i.e., the range of β covered is not symmetric around $\beta = 0°$.

$$C_{D_t} = \frac{D_t}{1/2\rho V^2 S} = \frac{1/2\rho V^2 S_t C_{d_t}}{1/2\rho V^2 S} = \frac{S_t}{S} C_{d_t}. \tag{12}$$

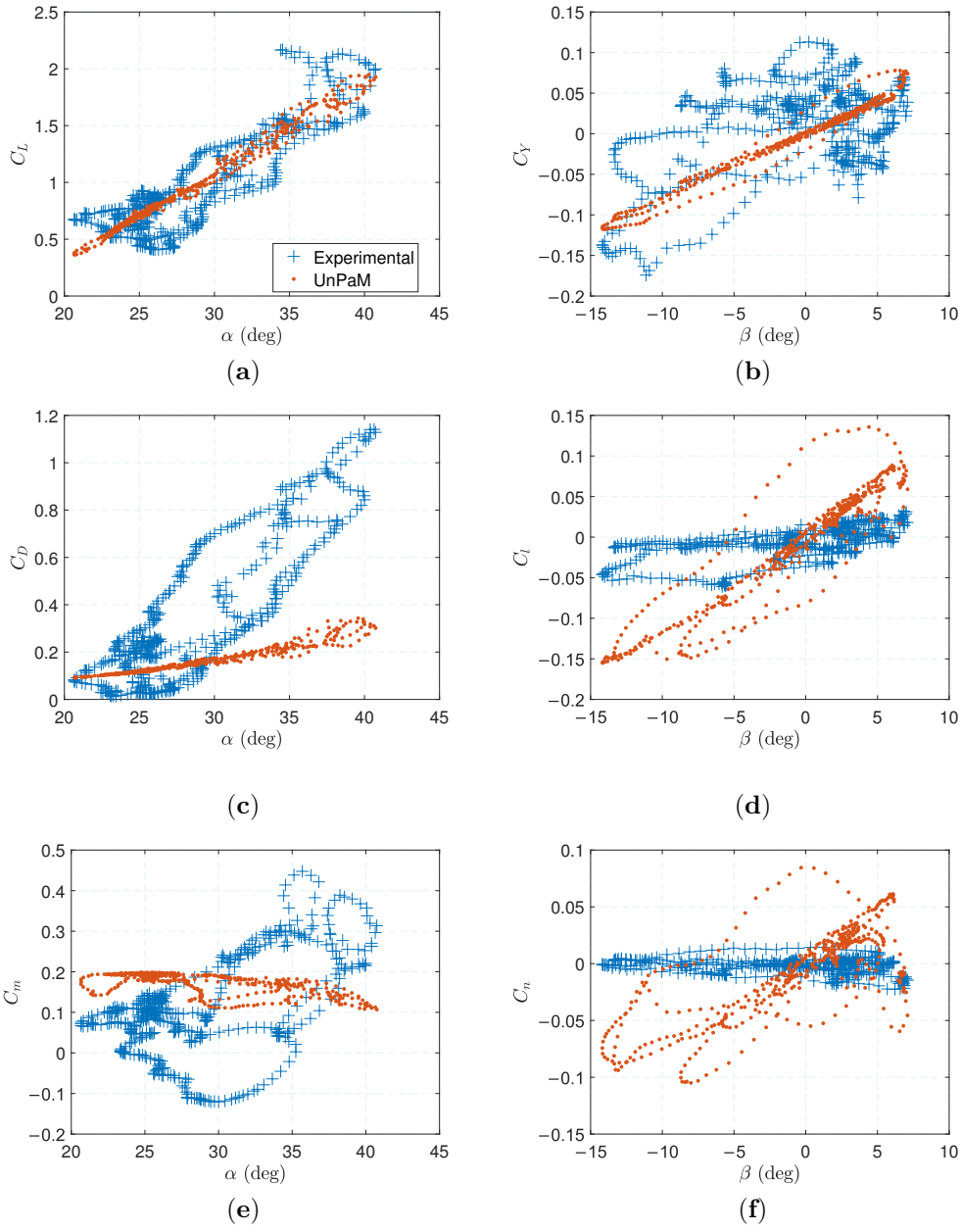

Figure 5: Force (**a**–**c**) for lift, lateral force and drag, and moment (**d**–**f**) for roll, pitch and yaw coefficients comparison between UnPaM and experimental aerodynamic results.

Regarding the three moment coefficients, the magnitudes of the experimental and numerical results are in the same order, but there does not exist a clear match in trend

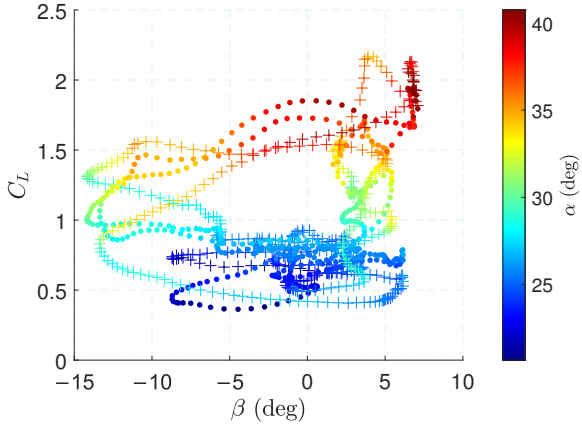

Figure 6: Lift coefficient (crosses and points for experimental and UnPaM data, respectively) versus the sideslip angle with colormap for α values.

between them. In this case, the comparison and the extraction of conclusions is more difficult. On the one hand, UnPaM has the limitations already discussed for the force coefficients, including the inability to capture flow separation. On the other hand, it is not clear that the procedure followed in Borobia-Moreno *et al.* (2021) can provide a high-accurate estimation of the aerodynamic moments. Unlike the TAS, the tension, the angle of attack, and the sideslip angle, the aerodynamic moments are not directly observed. Estimations of these magnitudes are provided by the extended Kalman filter by combining the process equations and the observation model. Moreover, the bridle of the kite was not considered in the state equations of the filter in Borobia-Moreno *et al.* (2021) and this impacts the estimations of C_m, C_L, and C_n. Among them, the one with a better correlation between the experimental and the numerical results is C_m.

Figure 7 shows the values of the force coefficients along the figure-of-eight trajectory. Experimental and numerical results are shown on the left and the right figures. To ease the comparison, the limits of the scale were set evenly for each pair of plots, except for the drag coefficient in Figure 7e,f. The general trend of the three force coefficients correlates reasonably well along the orbit. It also makes evident the very different conditions reached by the kite in the straight legs and the turning phases. The lift (Figure 7a,b) and drag (Figure 7e,f) coefficients reach their maxima in the turns where, eventually, the TAS (Figure 2) finds its minimum. The kite reduces its TAS in the turns, but its angle of attack increases to yield a high C_L and C_D. The opposite situation happens in the straight legs, where the TAS is large and the angle of attack and the force coefficients are small. This explains the high values of the tether tensions shown in Figure 2. The lateral force coefficient (Figure 7c,d) mainly follows the sideslip angle and it changes its sign along the trajectory.

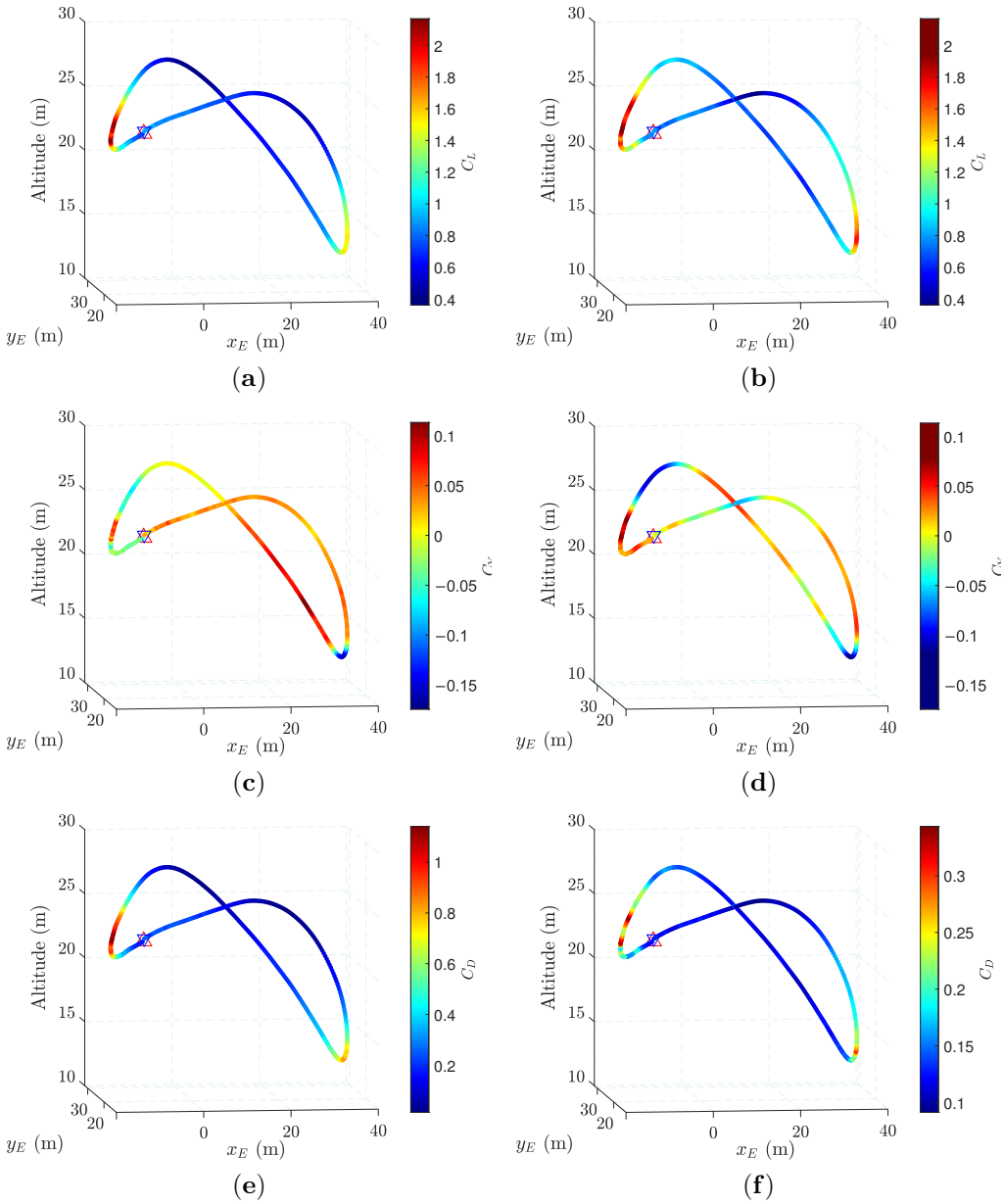

Figure 7: Kite trajectory with color map representing the force coefficients coming from experimental data (**left figures**) and UnPaM simulations (**right figures**).

4. Analysis of the potential flow

Figure 8 shows the results of UnPaM for $\alpha = 20°$, $\beta = 0°$ and $TAS = 10$ m/s, which are the typical conditions found during the figure-of-eight maneuver. UnPaM, which is

a potential-flow code, may work properly for these conditions because we checked that the zero-lift line is at an angle of attack of 15°. As explained in Section 2.2.2, the angle of attack is measured with respect to the spine of the kite in our analysis. The color in Figure 8a indicates the difference of the pressure coefficient between the intrados and extrados (ΔC_p). A very different behavior is observed at the two planes closer to the spine of the kite than in the two other planes that contain the leading edge because these two families of planes have a very different dihedral angle. Consequently, the coefficient ΔC_p is positive in the inner part of the kite and negative at the leading edge for this specific angle of attack. The maximum ΔC_p is reached at the two diagonals where the planes intersect. These three-dimensional results have been compared with the ΔC_p of a two-dimensional flat plate. Figure 8b shows the distribution of ΔC_p along the spine of the kite from UnPaM and Equation (13) of Ref. (Katz & Plotkin 2001) that reads

$$\Delta C_p = 4\sqrt{\frac{c_s - x}{x}}\alpha, \quad x \equiv x_{CM} - x_B, \tag{13}$$

where $c_s = 1.16$ m is the length of the spine of our RFD kite, $x_{CM} = 0.71$ m is the distance between its nose and center of mass, and x_B is the coordinate in the body frame. Due to three-dimensional effects, there is a mismatch between both curves and, as expected, UnPaM predicts a lower ΔC_p. The simulation also provides valuable information about the structure of the wake. As shown in Figure 8a, two pairs of counter-rotating vortices are formed. The first pair starts at the tips of the kite and the second appears at the intersections of the two families of planes. Opposite roll-up is observed for the vortices generated at the tips and the intersections lines due to the different dihedral angles of the planes that produce ΔC_p with different signs.

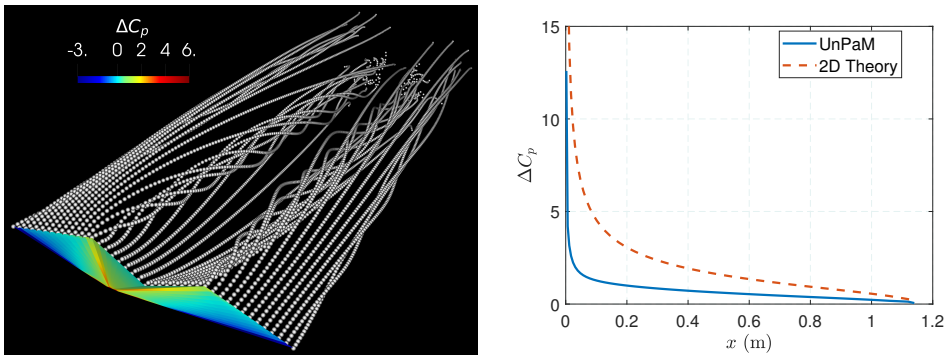

(**a**) (**b**)

Figure 8: UnPaM aerodynamic simulation (20^{th} time step) at a fixed α of 20^{o} and β of 0^{o}. (**a**) shows the ΔC_p across the kite and the wake roll-up while (**b**) shows the central spine ΔC_p distribution for the 3D case (UnPaM) and 2D theory of a flat plate.

In order to obtain an idea of the unsteady effects in the flight of the RFD kite, we present now three different types of results: (i) unsteady results obtained by implementing the methodology explained in Section 2.2, (ii) quasi-steady results obtained such as in (i) but ignoring the second term in Equation (8) and eliminating the roll-up of the wake

by forcing the geometry of its panels, and (iii) steady results obtained such as in (ii) but setting $\boldsymbol{\omega}_{BW} = \mathbf{0}$. Figure 9a shows the lift coefficient of the three approaches versus time (left axis) and, for convenience, it also displays the evolution of the angle of attack (right axis) in the figure-of-eight trajectory. The three approaches give the same results for the straight legs of the figure of eight, where the angle of attack and the angular velocity are small and the TAS is high. The main differences occur during the turns, as shown in the detail provided in Figure 9b. The steady approximation mostly underestimates the value of C_L. Interestingly, there exists a lag between the C_L and α in the unsteady approximation. The maxima of the C_L in the unsteady approximation occurs later than the maxima of the angle of attack. Regarding the steady and the quasi-steady approximations, the maxima of the C_L and the α curves occur simultaneously. Even during the turning, the differences are small and a steady or a quasi-steady simulation may suffice for the aerodynamic modeling of RFD kites flying in crosswind trajectories.

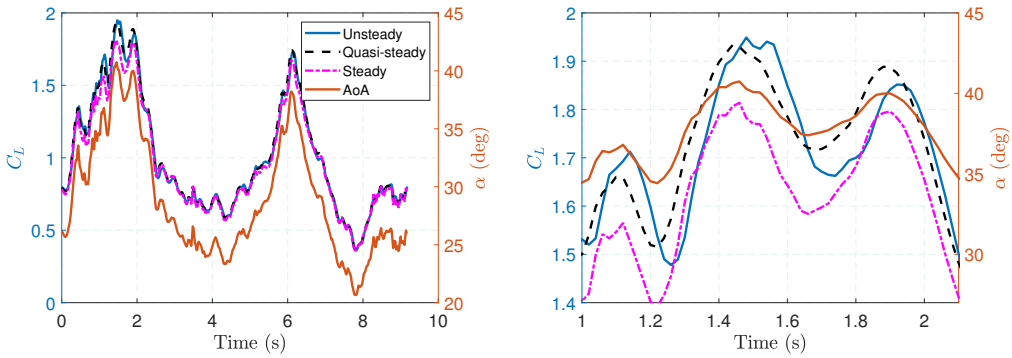

Figure 9: Lift coefficient for unsteady, quasi-steady and steady UnPaM simulations for the kinematics resulting from the figure-of-eight maneuver under study. (**a**,**b**) give the full trajectory and and a zoom-in, respectively.

5. Conclusions

This work benchmarked a three-dimensional unsteady potential aerodynamic tool against experimental data obtained in a flight campaign with a rigid-framed delta kite of 1.86 m^2. A figure-of-eight orbit, which is the relevant trajectory for airborne wind energy systems, was studied in detail. The kinematic state of the kite in the experiments was used as input for the code. A good and moderate agreement for the lift and the lateral force coefficients, respectively, was found. The drag coefficient matched only for low values of the angle of attack. The potential flow code underestimated the drag because ignores viscous effects. Theoretical and experimental moment coefficients are in the same order of magnitude but they do not follow the same trend. In this case, the confidence on the moment coefficients estimated in the experimental campaign is lower than in the case of the forces due to issues related to the modelization of the bridle of the kite and the comparison is troublesome. The experimental and theoretical results presented in this work are a step toward the

understanding and characterization of kite aerodynamics, but more reliable data for the aerodynamic moments (experimental and theoretical) are still necessary.

The experimental results revealed that the lift and drag coefficients can take different values when presented as just a function of the angle of attack. The potential flow code, and a fine analysis of the experimental result, showed that this is not due to a possible dependence of C_L on the sideslip angle. This hysteresis in the C_L and C_D versus α curves, and also the high values of lift coefficients measured in the experiments, may be a consequence of unsteady phenomena. Dynamic stall, which is experienced by wings subject to periodic pitching motions, is one of the candidates to explain it. The results of this study suggest that future works on including dynamic stall semi-empirical methods in the numerical codes can help improve the aerodynamic characterization of the RDF kite while keeping low its computational cost.

UnPaM's performance in terms of computational time opens the possibility for coupling this tool with AWE flight simulators. In particular, if UnPaM is combined with AWE models based on inelastic tethers to remove the fast time scale (longitudinal waves along the tether), a low-computational-cost numerical tool can be prepared. For instance, for the aerodynamic mesh used in this work, the computational time for UnPaM to carry out one time step in our machine is in the order of magnitude of a second. Considering that the real time required by the kite to perform a full figure-of-eight trajectory is 10 s, and a time-step in the dynamic simulations can be in the order of 1×10^{-2} s, the total time to simulate a full orbit is less than half an hour. Moreover, this work demonstrated that a quasi-steady approximation within the UnPaM suite can be sufficient for the characterization of the lift coefficient during the figure-of-eight trajectory and this can be use to speed-up the simulations. Therefore, the tool could be used for broad parametric analysis and optimal control with medium fidelity. Real-time simulations would be also possible by using the code to generate a broad database of aerodynamic coefficients as a function of the angle of attack and the sideslip angles.

Acknowledgements

This work was carried out under the framework of the GreenKite-2 project (PID2019-110146RB-I00) funded by MCIN/AEI/10.13039/501100011033.

Appendix A. UnPaM High-Level Flowchart

Figure 10 shows a flowchart of the aerodynamic tool UnPaM. The unsteady simulations carried out in this tool are based on a time-stepping algorithm based on a Runge-Kutta 4 integrator to update the relevant kinematic variables (Section 2.2.2). At every time step, the kinematic variables are read and the potential flow is found by using the panel method explained in Section 2.2. The wake of the kite grows gradually until reaching a maximum size defined by the user at the beginning of the simulation. A full description of UnPaM is in (Cavallaro *et al.* 2015; Nardini 2014).

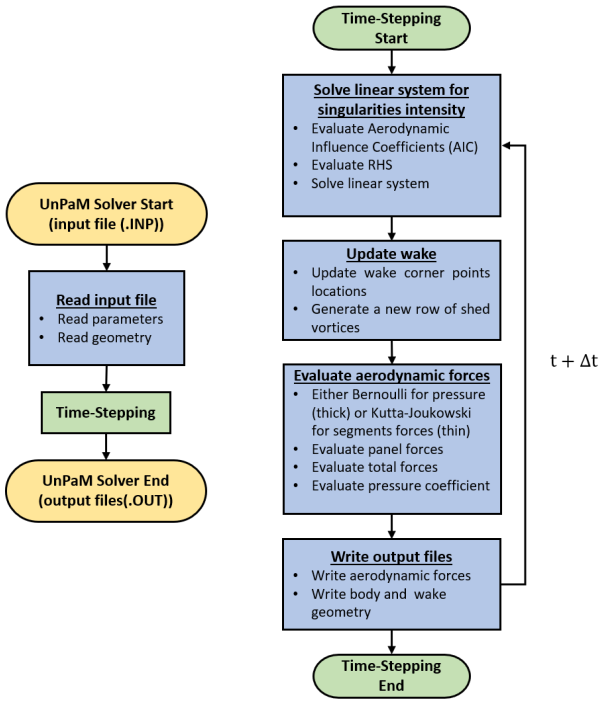

Figure 10: High-level flowchart of UnPaM in unsteady simulations.

References

Ali, Q. S. & Kim, M. H. 2020 Unsteady aerodynamic performance analysis of an airborne wind turbine under load varying conditions at high altitude. *Energy Convers. Manag.* **210** (December 2019), 1–18.

Bartlett, G. E. & Vidal, R. J. 1955 Experimental Investigation of Influence of Edge Shape on the Aerodynamic Characteristics of Low Aspect Ratio Wings at Low Speeds. *J. aernautical Sci.* **22** (8), 517–533.

Borobia, R., Sánchez-Arriaga, G., Serino, A. & Schmehl, R. 2018 Flight-Path Reconstruction and Flight Test of Four-Line Power Kites. *J. Guid. Control. Dyn.* **41** (12), 2604–2614.

Borobia-Moreno, R., Ramiro-Rebollo, D., Schmehl, R. & Sánchez-Arriaga, G. 2021 Identification of kite aerodynamic characteristics using the estimation before modeling technique. *Wind Energy* **24** (6), 596–608.

Bosch, A., Schmehl, R., Tiso, P. & Rixen, D. 2014 Dynamic nonlinear aeroelastic model of a kite for power generation. *J. Guid. Control. Dyn.* **37** (5), 1426–1436.

Breukels, J., Schmehl, R. & Ockels, W. 2013 Aeroelastic Simulation of Flexible Membrane Wings based on Multibody System Dynamics. In *Airborne Wind Energy. Ser. Green energy Technol.*, pp. 287–305.

Candade, A. A., Ranneberg, M. & Schmehl, R. 2020*a* Aero-structural Design of Composite Wings for Airborne Wind Energy Applications. *J. Phys. Conf. Ser.* **1618** (3).

Candade, A. A., Ranneberg, M. & Schmehl, R. 2020*b* Structural analysis and optimization of a tethered swept wing for airborne wind energy generation. *Wind Energy* **23** (4), 1006–1025.

Cavallaro, R., Nardini, M. & Demasi, L. 2015 Amphibious prandtlplane: Preliminary design aspects including propellers integration and ground effect. In *56th AIAA/ASCE/AHS/ASC Struct. Struct. Dyn. Mater. Conf.*, pp. 1–27.

Cherubini, A., Papini, A., Vertechy, R. & Fontana, M. 2015 Airborne Wind Energy Systems: A review of the technologies. *Renew. Sustain. Energy Rev.* **51**, 1461–1476.

Ecorys 2018 Study on Challenges in the commercialisation of airborne wind energy systems. *Tech. Rep.*. European Commission.

Fagiano, L., Huynh, K., Bamieh, B. & Khammash, M. 2014 On Sensor Fusion for Airborne Wind Energy Systems. *IEEE Trans. Control Syst. Technol.* **22** (3), 930–943.

Fagiano, L., Nguyen-Van, E., Rager, F., Schnez, S. & Ohler, C. 2018 Autonomous Takeoff and Flight of a Tethered Aircraft for Airborne Wind Energy. *IEEE Trans. Control Syst. Technol.* **26** (1), 151–166.

Fasel, U., Keidel, D., Molinari, G. & Ermanni, P. 2017 Aerostructural optimization of a morphing wing for airborne wind energy applications. *Smart Mater. Struct.* **26**, 1–11.

Fasel, U., Tiso, P., Keidel, D., Molinari, G. & Ermanni, P. 2019 Reduced-order dynamic model of a morphing airborne wind energy aircraft. *AIAA J.* **57** (8), 3586–3598.

Fechner, U., van der Vlugt, R., Schreuder, E. & Schmehl, R. 2015 Dynamic model of a pumping kite power system. *Renew. Energy* **83**, 705–716.

Folkersma, M., Schmehl, R. & Viré, A. 2019 Boundary layer transition modeling on leading edge inflatable kite airfoils. *Wind Energy* **22** (7), 908–921.

Gordnier, R. E. & Visbal, M. R. 2004 Computation of the aeroelastic response of a flexible delta wing at high angles of attack. *J. Fluid Struct.* **19**, 785–800.

Gray, J. M., Gursul, I. & Butler, R. 2003 Aeroelastic Response of a Flexible Delta Wing due to Unsteady Vortex Flows. *41st Aerosp. Sci. Meet. Exhib. AIAA 2003-1106* (January), 1–8.

Gursul, I. 2004 Recent developments in delta wing aerodynamics. *Aeronaut. J.* (2894), 437 – 452.

Hesse, H., Polzin, M., Wood, T. A. & Smith, R. S. 2018 Visual motion tracking and sensor

fusion for kite power systems. In *Airborne Wind Energy. Ser. Green energy Technol.*, , vol. 9789811019, pp. 413–438.

Hoff, J. C. & Cook, M. V. 1996 Aircraft Parameter Estimation by an Estimation-Before-Modelling Technique. *Aeronaut. J. R. Aeronaut. Soc.* (January 1996).

Hummel, J., Göhlich, D. & Schmehl, R. 2019 Automatic measurement and characterization of the dynamic properties of tethered membrane wings. *Wind Energy Sci.* **4** (1), 41–55.

Katz, J. & Plotkin, A. 2001 *Low-Speed Aerodynamics*, 2nd edn. San Diego.

Leuthold, R. 2015 Multiple-Wake Vortex Lattice Method for Membrane-Wing Kites. *Tech. Rep.* December 2015. Delft University of technology.

Licitra, G., Bürger, A., Williams, P., Ruiterkamp, R. & Diehl, M. 2019 Aerodynamic model identification of an autonomous aircraft for airborne wind energy. *Optim. Control Appl. Methods* **40** (3), 422–447.

Licitra, G., Williams, P., Gillis, J., Ghandchi, S., Sieberling, S., Ruiterkamp, R. & Diehl, M. 2017 Aerodynamic Parameter Identification for an Airborne Wind Energy Pumping System. *IFAC-PapersOnLine* **50** (1), 11951–11958.

Malz, E. C., Koenemann, J., Sieberling, S. & Gros, S. 2019 A reference model for airborne wind energy systems for optimization and control. *Renew. Energy* **140**, 1004–1011.

Mehr, J., Alvarez, E. J. & Ning, A. 2020 Unsteady aerodynamic analysis of wind harvesting aircraft. In *Aiaa Aviat. 2020 Forum*, pp. 1–13.

Nardini, M. 2014 A Computational Multi-purpose Unsteady Aerodynamic Solver for the Analysis of Innovative Wing Configurations, Helicopter Blades and Wind Turbines. *Tech. Rep.*. University of Pisa.

Oehler, J. & Schmehl, R. 2019 Aerodynamic characterization of a soft kite by in situ flow measurement. *Wind Energy Sci.* **4** (1), 1–21.

Ranneberg, M. 2015 Direct Wing Design and Inverse Airfoil Identification with the Nonlinear Weissinger Method. *Tech. Rep.*.

Saleem, A. & Kim, M. H. 2020 Aerodynamic performance optimization of an airfoil-based airborne wind turbine using genetic algorithm. *Energy* **203**, 117841.

Sánchez-arriaga, G., Pastor-rodríguez, A., Sanjurjo-rivo, M. & Schmehl, R. 2019 A lagrangian flight simulator for airborne wind energy systems. *Appl. Math. Model.* **69**, 665–684.

Thedens, P., de Oliveira, G. & Schmehl, R. 2019 Ram-air kite airfoil and reinforcements optimization for airborne wind energy applications. *Wind Energy* **22** (5), 653–665.

Vermillion, C., Cobb, M., Fagiano, L., Leuthold, R., Diehl, M., Smith, R. S., Wood, T. A., Rapp, S., Schmehl, R., Olinger, D. & Demetriou, M. 2021 Electricity in the air: Insights from two decades of advanced control research and experimental flight testing of airborne wind energy systems. *Annu. Rev. Control* **52** (December 2020), 330–357.

Vimalakanthan, K., Caboni, M., Schepers, J., Pechenik, E. & P.Williams 2018 Aerodynamic analysis of Ampyx's airborne wind energy system. *J. Phys. Conf. Ser.* **1037**, 1–10.

Viré, A., Demkowicz, P., Folkersma, M., Roullier, A. & Schmehl, R. 2020 Reynolds-averaged Navier-Stokes simulations of the flow past a leading edge inflatable wing for airborne wind energy applications. *J. Phys. Conf. Ser.* **1618** (3).

Wijnja, J., Schmehl, R., Breuker, R. D., Jensen, K. & Lind, D. V. 2018 Aeroelastic Analysis of a Large Airborne Wind Turbine. *J. Guid. Control. Dyn.* **41**, 1–12.

Paper 2

2

Unsteady Aerodynamics of Delta Kites for Airborne Wind Energy under Dynamic Stall Conditions

I. Castro-Fernández[1], R. Cavallaro[1], R. Schmehl[2] & G. Sánchez-Arriaga[1]

[1] Departamento de Ingeniería Aeroespacial, Universidad Carlos III de Madrid, Leganés, 28911 Madrid, Spain

[2] Faculty of Aerospace Engineering, Delft University of Technology, Delft, The Netherlands

Wind Energy (2023), vol. **(Under Review)**

Three unsteady aerodynamic tools at different levels of fidelity and computational cost were used to investigate the unsteady aerodynamic behavior of a delta kite applied to airborne wind energy. The first tool is an in-house unsteady panel method that is fast but delivers low- to mid-fidelity predictions. The second tool uses the open-source CFD code SU2 to solve the unsteady Reynolds-averaged Navier-Stokes equations with the $k-\omega$ SST turbulence model. At an intermediate level of fidelity, a semi-empirical dynamic stall model that combines the panel method with a phenomenological dynamic stall module is proposed. The latter has free parameters that are fine-tuned with CFD results from the second tool. The research on the dynamic stall model has been inspired by two flight test campaigns suggesting dynamic stall phenomena possibly driven by the periodic variation of the angle of attack (aerodynamic pitching motion) during crosswind maneuvers. The recorded inflow along the flight path was prescribed in the three aerodynamic tools. As expected, the price to pay for the low computational cost of the panel method is its inability to capture the dynamic stall phenomenon. The results from unsteady CFD qualitatively matched the experimental data identifying a leading-edge vortex that forms and detaches cyclically during the pitching motion. Using RANS data, the semi-empirical tool was fined-tuned to reproduce the dynamic stall behavior, becoming an accurate and fast aerodynamic tool for coupling with any kite flight simulator. Further discussions on the effects of kite aerostructural deflections are included.

Keywords: Dynamic stall; flow visualization; leading-edge vortex; rigid-framed delta kite; semi-empirical aerodynamic model

---

1. Introduction

Airborne wind energy (AWE) systems employ tethered aircraft to convert wind power into electricity or gain traction from the wind. The multidisciplinary nature of AWE systems involve, among others, flight dynamics (Fechner *et al.* 2015; Sánchez-arriaga *et al.* 2019), control (Vermillion *et al.* 2021) and fluid-structure interaction (Fasel *et al.* 2019; Pynaert *et al.* 2023). For obvious reasons, aerodynamics has a prominent role, witnessed by the amount of research effort put into numerical aerodynamic modeling and experimental aerodynamic characterization of different AWE aircraft.

Steady aerodynamic tools based on potential flow were broadly applied to AWE systems due to their low computational cost. The lifting-line method was applied to a fixed wing with onboard turbines to investigate the aeroelasticity of a large fly-gen AWE system (Wijnja *et al.* 2018). The same method was combined with externally derived 2D viscous aerodynamic polars to improve the predictions of the drag coefficient (Leloup *et al.* 2013; Haas *et al.* 2022) and to account for nonlinear corrections of the lift coefficient at stall by using a nonlinear vortex step method (Damiani *et al.* 2019; Candade *et al.* 2020*b*; Cayon *et al.* 2023). The major limitation of the lifting-line method is the inherent inability to capture the chordwise lift distribution of the aerodynamic surfaces because the latter are discretized into planar horseshoes (one per chordwise section). For that purpose, the three-dimensional steady vortex lattice method (VLM) was employed to model highly non-planar wings such as leading-edge inflatable (LEI) kites (Gaunaa *et al.* 2011) and morphing wings for AWE applications (Fasel *et al.* 2017, 2019). Nonlinear stall corrections in the lift and drag coefficients were introduced into a 3D VLM by shedding multiple wakes from prescribed positions of flow separation (Leuthold 2015). Due to its suitability for thick wings, the open-source steady panel method APAME was applied to ram-air kites in an aero-structural framework (Thedens & Schmehl 2023) and box-wing configurations (Eijkelhof *et al.* 2023). Besides steady-state analyses, unsteady aerodynamic effects induced by crosswind maneuvers were quantified by applying a 3D unsteady VLM to a rigid-framed delta (RFD) kite (Castro-Fernández *et al.* 2021). Unsteady effects proved to play a role for highly dynamic AWE maneuvers. The unsteady VLM was also useful to generate a reduced-order dynamic model of a fixed-wing AWE system by including the body vortex strengths in the state vector (Fonzi *et al.* 2020). Potential-flow methods have shown to be a low- to mid-fidelity alternative for aerodynamic modeling of AWE systems but are not accurate tools in scenarios where flow separation is essential.

At a higher fidelity level, the 2D flow field over a LEI kite was solved using steady Reynolds-averaged Navier-Stokes (RANS) simulations with the $k-\omega$ SST turbulence model and the $\gamma - \widetilde{Re}_{\theta t}$ laminar to turbulent transition model (Folkersma *et al.* 2019). The steady-state fluid-structure interaction in LEI kites was also studied by coupling 2D steady RANS simulations for the kite's spanwise sections with a multibody model of the tube kite (Breukels *et al.* 2013). A similar steady fluid-structure interaction model was coupled with a dynamic model of the AWE system that also included a flight controller to fly figure-of-eight maneuvers (Bosch *et al.* 2014). All the 2D RANS analyses over LEI kites highlighted the importance of using high-fidelity aerodynamic methods to model the recirculation zone behind the leading edge tube even at low angles of attack and the flow separation on the extrados (suction side). Three-dimensional steady RANS simulations become necessary to capture not only viscous but also three-dimensional effects which are not negligible due to the relatively low aspect ratio and highly non-planar geometries of AWE kites. Some of the first computational fluid dynamics (CFD) studies on kites solved the 3D steady RANS equations around curved (C-type) wings with a double membrane (Buffoni *et al.* 2014) and a NACA 64-418 sectional shape (Gaunaa *et al.* 2011). The 3D flow around a LEI kite was studied by using steady RANS simulations with the $k-\omega$ SST turbulence model and the $\gamma - \widetilde{Re}_{\theta t}$ transition model (Viré *et al.* 2020). An expansion of this work concluded that the effect of chordwise struts in LEI kites is negligible irrespective of the sideslip angle, however, the latter influenced the aerodynamic efficiency (L/D, being L and D the lift and drag) of the LEI kite (Viré *et al.* 2022). The steady aeroelastic

deformation of a ram-air kite was studied by coupling the 3D RANS equations ($k-\omega$ SST turbulence model) with a membrane-like finite element model (Folkersma *et al.* 2020).

High-fidelity CFD simulations were also applied to fixed-wing AWE systems. A multi-element airfoil applied to AWE was aerodynamically optimized using 2D steady RANS (De Fezza & Barber 2022) and the viscous-inviscid solver MSES together with RANS verifications (Ko *et al.* 2023). The comparison between MSES and RANS in Ko *et al.* (2023) highlighted the need of using a CFD tool to verify a lower-fidelity tool. The 3D aerodynamics of the fixed-wing Ampyx power aircraft was studied through RANS ($k-\omega$ SST turbulence model) (Vimalakanthan *et al.* 2018). Apart from RANS approximation, the viscous vortex particle method was applied to the Makani M-600 prototype with and without onboard turbines (Mehr *et al.* 2020). Regarding fluid-structure interaction, a recent work studied a multi-megawatt AWE reference model by coupling a detailed finite element model for the structure with unsteady RANS ($k-\omega$ SST turbulence model and wall-function approximations near the wing) (Pynaert *et al.* 2023). In Pynaert *et al.* (2023), the full wind window of the AWE system ($620 \times 620 \times 100$ m^3) was solved with unsteady RANS and the vehicle followed a circular crosswind trajectory with a logarithmic wind profile. The latter produced variations in the angle of attack and, consequently, in the lift and drag coefficients highlighting the importance of considering realistic crosswind kinematics as compared with steady conditions in AWE applications. Another remark of Pynaert *et al.* (2023) is the negligible influence of the kite's wake on the aerodynamic coefficients ($\sim 0.2\%$) suggesting that a smaller domain containing the aircraft and its kinematics with respect to the wind may be aerodynamically equivalent.

On the experimental side, several AWE testbeds aiming at the aerodynamic characterization of kites fused data from on-ground and onboard sensors to estimate the state vector of the kite including aerodynamic variables (Borobia *et al.* 2018; Oehler & Schmehl 2019; Schmidt *et al.* 2020; Borobia-Moreno *et al.* 2021). In-flight flow measurements to estimate the aerodynamic velocity, angle of attack and sideslip angle were obtained for the first time with a system composed of vanes and a pitot tube attached to the bridle lines of a LEI kite (Oehler & Schmehl 2019). Likewise, a more accurate multi-hole pitot tube was boarded on an RFD kite and the aerodynamic forces and torques were estimated as part of the state vector by using estimation before modeling techniques (Borobia-Moreno *et al.* 2021). Refs. Oehler & Schmehl (2019); Borobia-Moreno *et al.* (2021) uncovered relevant unsteady aerodynamic and aeroelastic phenomena after observing variations of the angle of attack and aerodynamic coefficients during figure-of-eight maneuvers. Refs. Borobia-Moreno *et al.* (2021); Castro-Fernández *et al.* (2021) proposed dynamic stall as a candidate to explain the hysteresis of the experimental aerodynamic coefficients versus the angle of attack. Dynamic stall is an unsteady viscous phenomenon that is not captured by potential-flow theory. Both CFD codes and semi-empirical dynamic stall models have been extensively used to simulate this phenomenon. Semi-empirical dynamic stall models combine potential-flow theory with a set of phenomenological dynamic equations with free empirical parameters at a lower computational cost than CFD simulations. The well-known semi-empirical dynamic stall models of Tran and Petrot (Tran & Petot 1980) (ONERA model), and Leishman and Beddoes (Leishman & Beddoes 1989) (Leishman-Beddoes model) were employed to model the aerodynamic responses of helicopter (Sheng *et al.* 2012) and wind turbine (Bangga *et al.* 2020) blades. Among the various modifications of the Leishman-Beddoes model, Ref. Hansen *et al.* (2004) considered the unsteady effects in the aerodynamic coefficients as variations about the steady values, improving the

agreement between the dynamic stall model and the high-fidelity data, and Ref. Boutet *et al.* (2020) modified the Leishman-Beddoes model to account for low Reynolds and low Mach numbers.

Since used by some companies and universities like Enerkite (Candade *et al.* 2020*b*) and UC3M (Borobia-Moreno *et al.* 2021; Castro-Fernández *et al.* 2023), delta wings and kites are particularly interesting for AWE applications. For this reason, this work carries out a detailed unsteady aerodynamic analysis of RFD kites by combining experiments and numerical simulation with two objectives: (i) uncover dynamic stall phenomena during the figure-of-eight maneuvers and (ii) develop an accurate aerodynamic model with a low computational cost. With this aim, it is first shown in Section 2 that the experimental lift and drag coefficients of RFD kites versus the angle of attack exhibit hysteresis repeatedly in the figure-of-eight trajectories measured in the experiments. Moreover, an in-situ flow visualization experiment revealed a cyclic flow separation on the kite extrados and strong deformations of the central bar (spine) and canopy of the kite. Since to the best of the authors' knowledge dynamic stall was not studied before for AWE applications through numerical simulations, Section 3 presents three aerodynamic models at different levels of fidelity and computational cost. The first model is the 3D unsteady panel method (UnPaM) presented in Castro-Fernández *et al.* (2021) with novel modifications of the wake that improve the prediction quality of the tool. The second model solves the unsteady incompressible RANS equations with the $k-\omega$ SST turbulence model of the open-source code SU2 (Palacios *et al.* 2013, 2014; Economon *et al.* 2016). The third model, which has a degree of fidelity and computational cost between the first and second, is a semi-empirical dynamic stall model that combines UnPaM with a phenomenological dynamic stall module. Such a module has free parameters that were fine-tuned by using steady and unsteady RANS results from the second tool. In Section 4, the results from the three unsteady aerodynamic tools were benchmarked against one another. With the purpose of quantifying the effect of kite deformation, a new deflected geometry was designed. The aerodynamic results of the new and the nominal kites were compared with experiments in Section 5. Finally, Section 6 presents the main conclusions and proposes future works to improve our understanding of the aerodynamic and aeroelastic behavior of RFD kites for AWE applications.

2. Experimental evidence of dynamic stall

The estimation before modeling technique was employed in a previous work to experimentally reconstruct the state vector of a two-line RFD kite (see physical characteristics in Table 1) during multiple figure-of-eight trajectories (Borobia-Moreno *et al.* 2021). The state vector included the aerodynamic velocity vector (magnitude or relative inflow speed V_A, angle of attack α and sideslip angle β) and the force and moment aerodynamic coefficients, among others.

In the following, the aerodynamic force (drag C_D, lateral C_Y and lift C_L) and moment coefficients (roll C_l, pitch C_m and yaw C_n) about the kite center of mass (CM) are defined as

$$(C_D, C_Y, C_L) = -\frac{2}{\rho V_A^2 S}\boldsymbol{F}\cdot(\boldsymbol{i}_W, -\boldsymbol{j}_W, \boldsymbol{k}_W)\,, \tag{1}$$

$$(C_l, C_m, C_n) = \frac{2}{\rho V_A^2 S}\boldsymbol{M}\cdot\left(\frac{\boldsymbol{i}_B}{b}, \frac{\boldsymbol{j}_B}{c}, \frac{\boldsymbol{k}_B}{b}\right), \tag{2}$$

where ρ is the air density, S, c and b are the planform area, chord and span of the kite, respectively (Table 1), $\boldsymbol{F}$ and $\boldsymbol{M}$ are the total aerodynamic force and moment vectors, and $(\boldsymbol{i}, \boldsymbol{j}, \boldsymbol{k})$ denote a Cartesian vector base. The body frame is denoted by subscript B and has the origin at the kite CM, the x_B-axis along the central bar of the kite, the z_B-axis normal to the x_B-axis, contained in the plane of symmetry of the kite and pointing toward the ground in horizontal straight flight, and the y_B-axis completes the right-handed frame. For convenience, the wind frame (denoted by W), also known as aerodynamic or apparent wind frame, is defined with the origin at the kite CM, x_W-axis along the aerodynamic velocity vector, z_W-axis normal to x_W-axis, contained in the kite symmetry plane and pointing toward the ground in horizontal straight flight, and y_W-axis completing the right-handed frame.

Table 1: Physical characteristics of the RFD kite. The position of the center of mass X_{CM} was measured from the nose along the central bar of the kite.

Surface (S)	Span (b)	Mean aerodynamic chord (c)	Central bar chord (c_s)	Center of mass (X_{CM})
1.86 m^2	3.60 m	0.59 m	1.16 m	0.71 m

Figure 1 shows the experimental lift C_L and drag C_D coefficients versus the angle of attack of the RFD kite during one and a half figures of eight. Three hysteresis cycles, where the aerodynamic coefficients are not unequivocally identified by the angle of attack but they also depend on its history, are observed in panels (a) and (b), and are denoted with different markers. The arrows in panels (a) and (b) indicate the loops direction showing that the coefficients reach high values before stalling when $\dot{\alpha} > 0$. However, their values considerably decrease as $\dot{\alpha}$ changes its sign. This cyclic behavior was observed robustly during the whole experiments that lasted for 3 minutes and involved more that 15 figure-of-eight maneuvers.

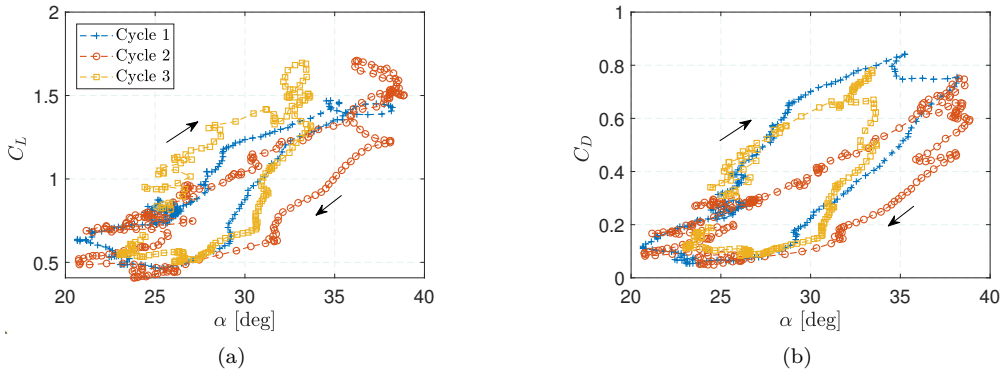

Figure 1: Lift (a) and drag (b) coefficients versus the angle of attack of the RFD kite during three hysteresis cycles (one and a half figures of eight) in the experiment of Borobia-Moreno *et al.* (2021).

An analysis of the evolution of α revealed that it had a period $T \approx 5$s, which is half of the period of the figure-of-eight trajectory, and an amplitude of about 20°. To understand this behavior, panel (a) of Figure 2 shows the kite trajectory for the first two cycles of Figure 1 using the same markers. The magnitude of the absolute velocity of the kite V_K is shown with color. Clearly, there are two complete cycles for each figure-of-eight maneuver and the velocity is maximum and minimum in the straight and turning path segments, respectively. This is probably induced by the type of figures of eight (up-loop) performed in the experiments, where gravity has opposite effects in the straight and turning segments. Since the aerodynamic velocity, i.e., the relative inflow speed, and angle of attack are given by

$$\begin{aligned} \boldsymbol{V}_A &\equiv \boldsymbol{V}_K - \boldsymbol{V}_W, \\ \alpha &\equiv \arctan\left(\frac{\boldsymbol{V}_A \cdot \boldsymbol{k}_B}{\boldsymbol{V}_A \cdot \boldsymbol{i}_B}\right), \end{aligned} \tag{3}$$

and the wind velocity $\boldsymbol{V}_W$ was roughly constant in the experiment, the periodic changes in the angle of attack essentially originate from the variations of the absolute velocity of the kite. For a typical aerodynamic velocity of $V_A = 15$ m/s, the reduced angular frequency associated to the periodic variation of the angle of attack in the experiment is $k = \dfrac{\omega c}{2V_A} \approx 0.03$, where $\omega = 2\pi/T$. For such a reduced frequency, unsteady phenomena like dynamic stall can be induced (McAlister *et al.* 1982; Ekaterinaris & Platzer 1997; Spentzos *et al.* 2007).

To get additional evidence of the dynamic stall, a complementary experiment to the one implemented in Borobia-Moreno *et al.* (2021) was carried out in this work. As shown in Figures 2b and 2c, surface tufts were mounted and recorded by a camera located at the trailing edge (central bar). Figure 2c shows two typical snapshots for attached (top) and separated (bottom) flow when the kite was located in straight and turning segments, respectively. Moreover, Figure 2c shows significant variations in the shape of the kite central bar. The latter increased and decreased its curvature when the flow was attached and separated, respectively, due to the variation in aerodynamic pressure over the kite canopy, suggesting strong fluid-structure interaction. The repeated occurrence of this cyclic behavior is evident in a 6-minute video available at (Universidad Carlos III de Madrid 2023). Despite experimental evidence of both dynamic stall and aerostructural deformation has been found, this work isolates the dynamic stall phenomena through aerodynamic simulation (Section 4). Additionally, a preliminary quantification of the kite deformation effects is carried out in Section 5.

Another important piece of information from the experiments, which is needed for the numerical analysis, is the kinematics of the body frame with respect to the wind frame. Since the focus is on the longitudinal aerodynamic coefficients, we set the numerical tools with zero sideslip angle and the temporal profiles $V_A(t)$ and $\alpha(t)$ measured in the experiment. In fact, they were approximated by the following Fourier series with 4 harmonics,

$$\begin{aligned} \alpha(t) &= \alpha_{c,0} + \sum_{i=1}^{4} \alpha_{c,i} \cos\left(i\omega_\alpha t\right) + \alpha_{s,i} \sin\left(i\omega_\alpha t\right), \\ V_A(t) &= V_{Ac,0} + \sum_{i=1}^{4} V_{Ac,i} \cos\left(i\omega_V t\right) + V_{As,i} \sin\left(i\omega_V t\right), \end{aligned} \tag{4}$$

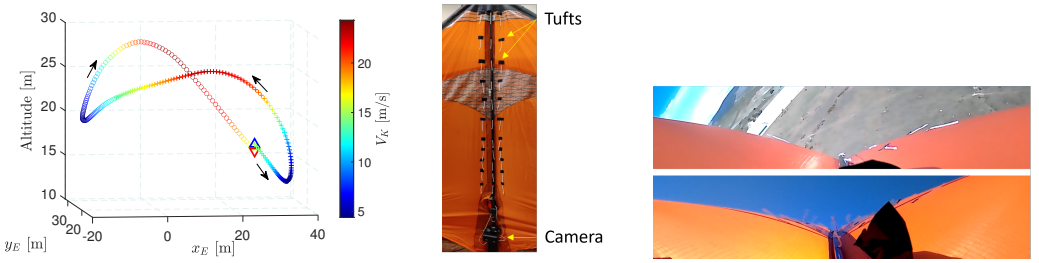

(a) (b) (c)

Figure 2: Panel (a) shows the kite trajectory colored with the magnitude of the kite absolute velocity $\boldsymbol{V}_K$. The blue upward (red downward) triangle corresponds to the start (end) of the trajectory and the crosses and circles correspond to hysteresis cycles 1 and 2 in Figure 1. Panel (b) displays the setup of the flow visualization experiment on the RFD kite with surface tufts and an onboard camera attached to the central bar. Panel (c) shows two typical snapshots for attached (top) and separated (bottom) flow.

to obtain a periodic and smooth kinematic input for the numerical simulations. Constants $\omega_\alpha, \omega_V, \alpha_{c,i}, \alpha_{s,i}, V_{Ac,i}$ and $V_{As,i}$, with $i = 0 \dots 4$, were found by doing 2 fittings from the experimental results for the first 2 cycles (see Table 2). As shown in Figure 3, the fittings provide a good representation of the experimental results.

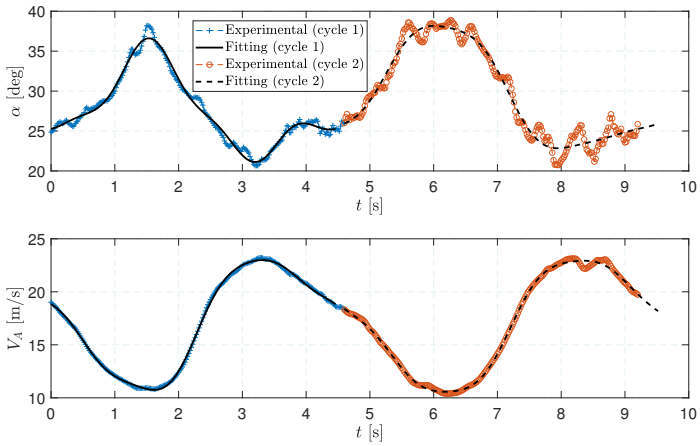

Figure 3: Experimental and approximated (Fourier series fitting) kinematic inputs for hysteresis cycles 1 and 2 in Figure 1.

Table 2: Coefficients of the Fourier series fittings of Equation (4) for hysteresis cycles 1 and 2 with $i = 0 \dots 4$.

	ω_α [rad/s]	ω_V [rad/s]	$\alpha_{c,i}$ [rad]	$\alpha_{s,i}$ [rad]	$V_{Ac,i}$ [m/s]	$V_{As,i}$ [m/s]
Cycle 1	1.406	1.411	0.4817	0	17.15	0
			−0.03563	0.08705	1.561	−5.84
			−0.000265	−0.04686	−0.1326	1.129
			0.006644	−0.005468	0.2246	−0.1846
			−0.01153	0.01131	0.04555	0.2914
Cycle 2	1.276	1.29	0.515	0	16.97	0
			−0.03943	0.1281	1.827	−5.995
			−0.01586	−0.02988	−0.2662	0.9596
			−0.01045	0.0006334	0.1144	−0.07895
			0.00347	−0.006407	−0.2453	0.2069

3. Computational aerodynamic tools

This work uses three different aerodynamic tools. For convenience, the next sections provide references that describe them completely and highlight specific aspects that are relevant for this work.

3.1. Potential-flow aerodynamics

The unsteady panel method (Nardini 2014; Cavallaro *et al.* 2015) is an in-house unsteady potential-flow tool with a low to medium level of fidelity and computational cost. As compared with Castro-Fernández *et al.* (2021), the wake geometry was modified in this work by changing the shedding direction based on RANS data from the tool in Section 3.2 (details are provided in Appendix A).

3.2. Unsteady Reynolds-averaged Navier-Stokes aerodynamics

3.2.1. *Fluid governing equations*

The open-source multiphysics suite SU2 (Palacios *et al.* 2013, 2014; Economon *et al.* 2016) have been chosen as CFD software. Due to the relatively low Mach numbers ($M \approx 0.05$), the incompressible solver was selected. Mesh deformation during the rigid motion of the kite was treated with an arbitrary Lagrangian-Eulerian (ALE) formulation. The equations governing the fluid motion in an ALE non-conservative differential form read (Hirsch 1984),

$$\begin{aligned} \rho \frac{\partial \boldsymbol{v}}{\partial t} + \rho \left([\boldsymbol{v} - \boldsymbol{v}_\Omega] \cdot \nabla \right) \boldsymbol{v} &= -\nabla P + \mu_{tot} \Delta \boldsymbol{v}, \quad \text{in } \Omega, t > 0, \\ \nabla \cdot \boldsymbol{v} &= \boldsymbol{0}, \qquad\qquad\qquad\quad \text{in } \Omega, t > 0, \end{aligned} \tag{5}$$

where ρ is the fluid density, $\boldsymbol{v}$ and $\boldsymbol{v}_\Omega$ are the fluid and mesh velocity vectors, P is the static pressure, Ω represents the 3D fluid domain and μ_{tot} is the sum of the dynamic viscosity μ_{dyn}, which is assumed to satisfy Sutherland's law (White 1974), and the turbulent viscosity μ_{turb}, which is obtained from the solution of the $k - \omega$ SST turbulence model due to Menter (Menter 1994). The latter describes the evolution of the turbulent kinetic energy k and specific dissipation ω through two additional partial differential equations.

The first and second equations in (5) are the momentum and mass conservation equations which provides four partial differential equations to solve for $\boldsymbol{v}$ and P.

Figure 4a shows the fluid domain Ω ($50 \times 40 \times 20$ m^3) considered for symmetric-flight conditions, which contains the right semi-wing of the RFD kite and the different boundary conditions. The no-slip boundary conditions, imposing that the fluid has the velocity of the body on its surface, are applied on the kite surface, the symmetric boundary conditions apply on the symmetry plane and the characteristic-based far-field boundary conditions are applied on the rest of the domain boundaries to ensure that they fulfill the free-stream conditions.

SU2 discretizes the domain with a finite volume method. In this work, the central Lax-Friedrich scheme (0.07 dissipation factor) and a Venkatakrishnan slope limiter were used to evaluate the convective terms of Equation (5). SU2 has steady and unsteady solvers. The steady solver uses a pseudo-time iteration scheme to find the steady-state solution. The selected unsteady solver uses a second-order dual time stepping procedure where there is an outer loop for the physical time steps ($\Delta t = 0.01$ s) and an inner loop using the pseudo-time iteration of the steady solver to converge to a solution at every physical time step.

3.2.2. *Mesh and prescribed kinematics module*

The boundaries of the 3D computational domain were meshed with 2D elements (quadrilaterals and triangles). A refinement region around the kite was defined on the symmetry plane (see refinement region and top view of the right semi-wing in the inset of Figure 4a). The surface of the kite, that encloses a volume, was meshed with 7.1×10^4 2D elements. The 3D computational domain was meshed by using hexahedral elements within the boundary layer (2 cm of thickness), tetrahedrals in the rest of the domain and pyramids in the interfaces between hexahedrals and tetrahedrals. The height of the first boundary-layer row was set to 1×10^{-5} m fulfilling the so-called $y^+ < 2$ criterion (Wilcox 2006). After a mesh convergence analysis, varying the kite surface mesh and the refinement region, a final mesh with roughly 7.8×10^6 3D cells was selected.

Regarding the kite kinematics, this work employed the fluid-structure interaction framework originally developed in Fonzi *et al.* (2022). After minor modifications of the framework regarding rigid-body motion, it was used to prescribe the kite motion and solve for the resulting aerodynamic coefficients. In this case, two rigid-body modes are necessary to describe the kinematics between the body and wind frames. The first mode is an aerodynamic pitching motion defined as a y_B-axis rotation of the kite of value $\alpha(t)$ given by Equation (4). On the other hand, following Equation (3), the fitted aerodynamic velocity $V_A(t)$ of Equation (4) is imposed in SU2 through the following two terms:

$$\boldsymbol{V}_W = -V_{Ac,0}\boldsymbol{i}_G, \quad \boldsymbol{V}_K = \frac{\mathrm{d}\overline{O_G O_B}}{\mathrm{d}t}, \tag{6}$$

with $V_{Ac,0}$ given in Table 2 and subscript G denoting a global frame that has axes parallel to the wind frame and is at rest with respect to the domain as shown in Figure 4a. The wind velocity $\boldsymbol{V}_W$ is set as a constant free-stream velocity in SU2. The kite absolute

velocity $\boldsymbol{V}_K$ is induced by a translation (second rigid-body mode) along x_G-axis as

$$\begin{aligned}\overline{O_G O_B}(t) &= \int_0^t \boldsymbol{V}_K(t)\mathrm{d}t = \int_0^t \left[\boldsymbol{V}_A(t) + \boldsymbol{V}_W(t)\right]\mathrm{d}t \\ &= \sum_{i=1}^{4}\left(\frac{V_{Ac,i}}{i\omega_V}\sin\left(i\omega_V t\right) - \frac{V_{As,i}}{i\omega_V}\cos\left(i\omega_V t\right) + \frac{V_{As,i}}{i\omega_V}\right)\boldsymbol{i}_G,\end{aligned} \tag{7}$$

with initial conditions $\overline{O_G O_B}(0) = \mathbf{0}$.

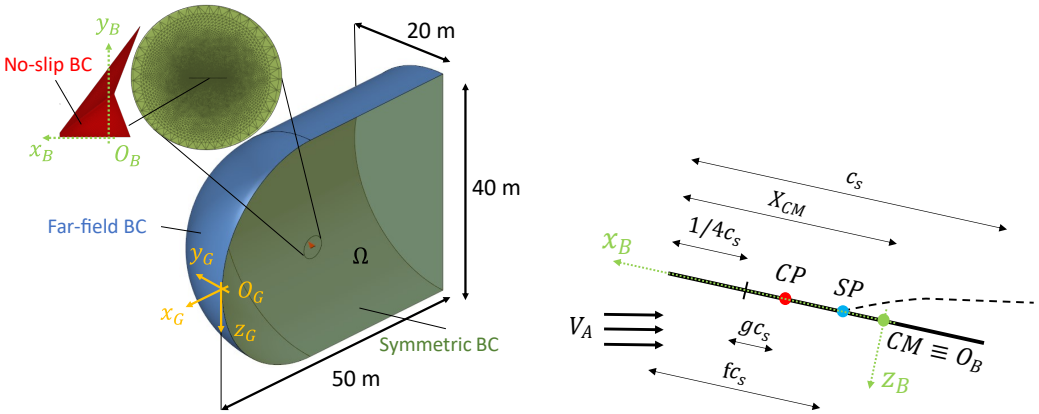

Figure 4: Panel (a) shows the fluid domain Ω indicating the no-slip, symmetric (inset of the refinement region around the kite and top view of the right semi-wing of the RFD kite) and far-field boundary conditions (denoted by BC), and the global reference frame (denoted by subscript G). Panel (b) shows a sketch of the typical section (kite central bar) used by the semi-empirical dynamic stall model with the center of pressure (CP), separation point (SP) and center of mass (CM).

The framework needs a set of structural nodes which in this case are coincident with the aerodynamic nodes of the kite surface mesh. After prescribing the position of the structural nodes following the two rigid-body modes, the fluid mesh must be deformed around the kite surface mesh. To do this, the framework calls a dedicated SU2 mesh deformation solver based on a linear elasticity analogy. Finally, the incompressible unsteady RANS solver of SU2 solves the fluid equations providing the aerodynamic coefficients at the current time step as an output. The loop continues by prescribing the positions of the structural nodes at the next physical time step.

3.3. Semi-empirical dynamic stall aerodynamic model

The third aerodynamic method is a semi-empirical dynamic stall model based on the original Leishman-Beddoes model (Leishman & Beddoes 1989) after some of the modifications described in Hansen *et al.* (2004) and Boutet *et al.* (2020). The Leishman-Beddoes model and its variants were routinely used to model dynamic stall in 2D airfoils and, in some cases, they were applied to several span-wise wing sections integrating the individual

contributions to obtain the global aerodynamic coefficients. In this work, the model is applied directly to the aerodynamic coefficients of the RFD kite and the typical section for 2D computations will be the central bar that is considered a flat plate with chord $c_s = 1.16$ m. Figure 4b displays a sketch of such a typical section with the center of pressure (CP) at a distance gc_s from the quarter-chord, the separation point (SP) at a distance fc_s from the leading edge and the kite CM at a distance X_{CM} from the leading edge. The model combines attached-flow theory through the potential-flow model UnPaM (Section 3.1) and a phenomenological dynamic stall module with three building blocks in state-space form.

3.3.1. *State-space equations*

The three phenomenological dynamic stall blocks, namely, leading edge separation, trailing edge separation and leading edge vortex, model the main physical phenomena associated to dynamic stall (Leishman & Beddoes 1989; Boutet *et al.* 2020). They are governed by a set of three first-order ordinary differential equations for the state $\boldsymbol{x}$ and an output model for the space $\boldsymbol{y}$,

$$\begin{aligned} \dot{\boldsymbol{x}} &= \boldsymbol{F}(\boldsymbol{x}, \boldsymbol{u}, \boldsymbol{C}^P, \boldsymbol{\theta}), \\ \boldsymbol{y} &= \boldsymbol{G}(\boldsymbol{x}, \boldsymbol{u}, \boldsymbol{C}^P, \boldsymbol{\theta}), \end{aligned} \tag{8}$$

with $\dot{\boldsymbol{x}}$ the time derivative of $\boldsymbol{x}$. The state $\boldsymbol{x}$, space $\boldsymbol{y}$, kinematic input $\boldsymbol{u}$, potential-flow coefficients $\boldsymbol{C}^P$ and parameters $\boldsymbol{\theta}$ vectors are given by

$$\begin{cases} \boldsymbol{x} = [\overline{\alpha}', f', C_L^v]^\top, \\ \boldsymbol{y} = [C_D^{DS}, C_Y^{DS}, C_L^{DS}, C_l^{DS}, C_m^{DS}, C_n^{DS}]^\top, \\ \boldsymbol{u} = [\alpha, V_A]^\top, \\ \boldsymbol{C}^P = [\boldsymbol{C}_D^P, \boldsymbol{C}_Y^P, \boldsymbol{C}_L^P, \boldsymbol{C}_l^P, \boldsymbol{C}_m^P, \boldsymbol{C}_n^P]^\top, \quad \boldsymbol{C}_j^P = [C_j^{P,S}, C_j^{P,Dc}, C_j^{P,Di}], \quad j = D, Y, L, l, m, n, \\ \boldsymbol{\theta} = [\boldsymbol{\theta}^S, \boldsymbol{\theta}^D]^\top, \quad \boldsymbol{\theta}^S = [a_{DS}, b_{DS}, c_{DS}, B_1, B_2, C_{D0}^{CFD,S}, C_{m0}^{CFD,S}], \quad \boldsymbol{\theta}^D = [T_f, T_v, T_{vl}]. \end{cases} \tag{9}$$

State $\overline{\alpha}'$ is a delayed version of the effective angle of attack $\overline{\alpha}$, defined from the normal (V_N) and chordwise (V_C) velocities induced at the quarter-chord as

$$\overline{\alpha} = \arctan\left(\left.\frac{V_N}{V_C}\right|_{1/4c_s}\right) = \arctan\left(\frac{V_A \sin\alpha - c_s\,[a - 1/4]\,\dot{\alpha}}{V_A \cos\alpha}\right), \tag{10}$$

with $a \equiv X_{CM}/c_s$ (see Figure 4b). The state variable f' is the delayed trailing edge separation point location f in the typical section of Figure 4b (f is 0 for fully separated flow and 1 for fully attached flow), and C_L^v is the lift contribution due to the change of circulation caused by the oscillatory motion. The space vector $\boldsymbol{y}$ contains the six aerodynamic coefficients obtained with the semi-empirical dynamic stall model. The kinematic input $\boldsymbol{u}$ of the dynamic stall model has two components: the angle of attack α and the aerodynamic velocity V_A. Vector $\boldsymbol{C}^P$ contains the potential-flow aerodynamic coefficients with superscript S standing for steady, and Dc and Di for dynamic circulatory and impulsive or added mass components, respectively. The vector of parameters $\boldsymbol{\theta}$ gathers

static $\boldsymbol{\theta}^S$ and dynamic $\boldsymbol{\theta}^D$ parameters. The static ones, which were taken from Boutet *et al.* (2020) and steady RANS data from SU2, are shown in Table 3. The dynamic parameters consist of three time delays that were fine-tuned by using unsteady RANS data from SU2. The final values are shown in Table 3. For the sake of clarity, further details of the state-space equations (8) are provided in Appendix B.

In an aerodynamic simulation with the semi-empirical dynamic stall tool, the kinematic inputs given by Equation (4) are first prescribed into UnPaM to obtain $\boldsymbol{C}^P$ at every time step. Known $\boldsymbol{u}$, $\boldsymbol{C}^P$ and $\boldsymbol{\theta}$, the state-space equations (8) are run with a set of initial conditions that are irrelevant for our analysis (e.g., $\boldsymbol{x} = [0.1, 0.1, 0.1]$) until a stable periodic solution is reached. The six aerodynamic coefficients resulting from the semi-empirical model at every time step are obtained as an output.

Table 3: Static $\boldsymbol{\theta}^S$ and dynamic $\boldsymbol{\theta}^D$ parameters of the dynamic stall model.

a_{DS}	b_{DS}	c_{DS}	B_1	B_2	$C_{D0}^{CFD,S}$	$C_{m0}^{CFD,S}$	T_f	T_v	T_{vl}
-2.97×10^{-5}	3.50×10^{-3}	-2.59×10^{-2}	1.50×10^{-2}	7.50×10^{-2}	0.17	0.08	0.06	0.10	0.26

4. Results

4.1. Aerodynamic results for steady conditions

Before discussing the unsteady results of the three aerodynamic tools under unsteady kinematic conditions, a comparison between potential-flow (UnPaM) and RANS (SU2) results for steady conditions (fixed aerodynamic velocity and angle of attack) is shown in this section. Figure 5 shows the three longitudinal aerodynamic coefficients (lift, drag and pitch moment) versus the angle of attack. The comparison between potential flow and RANS in the lift coefficient versus the angle of attack curve (Figure 5a) shows that both approximations have slightly different slopes. UnPaM overestimates the lift coefficient because it does not consider recirculation bubbles and separation in the complex geometry of the RFD kite. Moreover, the potential-flow curve keeps linear for the full range of α while RANS computations predict stall occurrence for $\alpha > 36$ deg. However, both tools predict approximately the same zero-lift angle of attack (~ 16 deg). Regarding the curve of the drag coefficient versus angle of attack (Figure 5b), UnPaM inherently underestimates the drag coefficient due to the lack of viscosity. The effect is more remarkable for high values of α where separation becomes more important. The RANS C_D versus α follows a typical polar shape with the minimum around the zero-lift angle of attack. The pitch moment coefficient as a function of α (Figure 5c) shows a good agreement between potential flow and RANS computations for a large range of angles of attack except in the stall region, where UnPaM does not predict the sudden decrease in C_m after stall.

A local analysis of the kite steady aerodynamics by monitoring the pressure coefficient C_p on the kite surface at a mild angle of attack (25°) is shown in Figure 6. Subpicture (a) shows the C_p distribution on the kite upper surface and 4 spanwise sections of the right semi-wing at distances $0, 0.25, 0.5, 1$ m from the kite symmetry plane. A negative-pressure region (suction) is found along the joint between the kite planes at different dihedral angles. In this region, a recirculation bubble forms even at low angles of attack and it bursts at high α being responsible for the full separation of the extrados of the wing. Subpicture (b) shows the pressure coefficient difference between the intrados (pressure side) and extrados

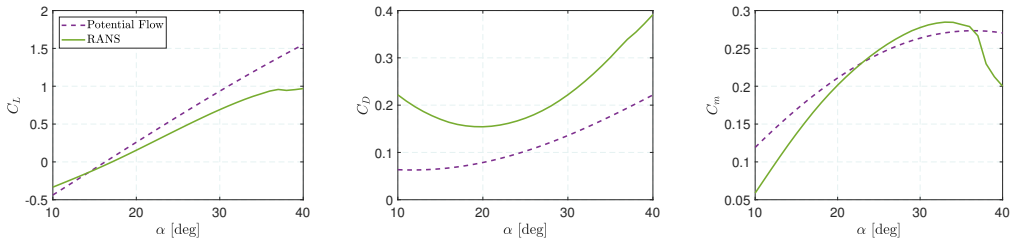

Figure 5: Lift (a), drag (b) and pitch moment (c) coefficients versus the angle of attack of the RFD kite in steady conditions.

(suction side) ΔC_p of the kite for the spanwise sections in panel (a) computed with potential flow (dashed lines) and RANS (solid lines). Both tools qualitatively agree on the distribution of ΔC_p of the 4 sections. Nevertheless, UnPaM predicts higher suction peaks in the leading edge and the joint between the planes at different dihedrals. Moreover, near the wing tip (section $y = 1$ m), RANS computations predict a more negative ΔC_p that leads to a higher downward force. Due to these effects, UnPaM generally overestimates the lift coefficient as compared to RANS as shown in Figure 5a.

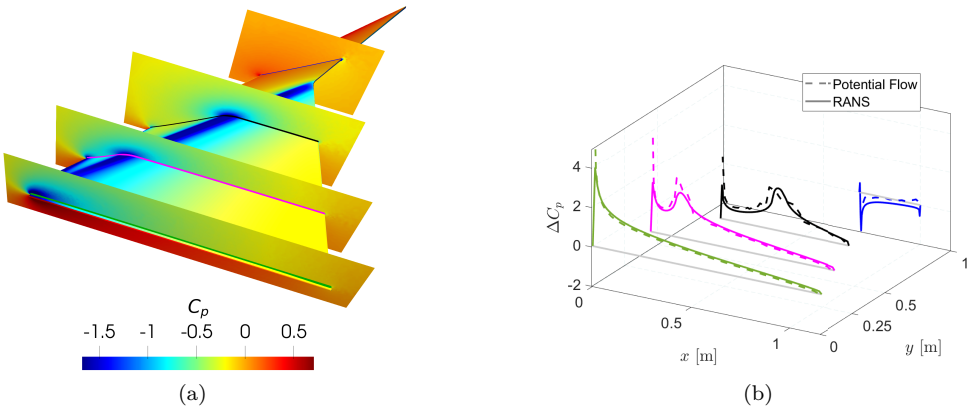

Figure 6: Steady RANS simulation of the RFD right semi-wing at an angle of attack of 25°. Panel (a) shows the pressure coefficient C_p distribution on the kite extrados and 4 spanwise sections at distances $y = 0, 0.25, 0.5, 1$ m from the kite symmetry plane. Panel (b) shows a comparison between potential flow and RANS of the pressure coefficient difference between the intrados and extrados ΔC_p along the chord x of the 4 spanwise sections in panel (a).

4.2. Aerodynamic results for unsteady conditions

Unsteady kinematic conditions were prescribed in the three aerodynamic tools described in Section 3 and the results were compared. Pitching motion ($\dot{\alpha} \neq 0$) and pitching motion with unsteady aerodynamic velocity ($\dot{\alpha} \neq 0$ and $\dot{V}_A \neq 0$) were tested to discuss the main drivers of the dynamic phenomena.

4.2.1. *Aerodynamic results for pitching motion*

The periodic pitching motion ($\dot{\alpha} \neq 0$) of cycle 2 in Figure 3 was firstly tested. The pressure coefficient C_p on the kite surface and some streamlines (colored with a grey scale) computed with unsteady RANS are shown in panels (a)-(f) of Figure 7 for different instants during the pitching motion: $\alpha = 23°$ (upstroke), 30° (upstroke), 35° (upstroke), 38° (downstroke), 35° (downstroke) and 30° (downstroke), where upstroke and downstroke indicate $\dot{\alpha} > 0$ and $\dot{\alpha} < 0$, respectively. It is observed that during the upstroke at low angles of attack (a), thin negative-pressure (suction) regions are present in the joint of the planes at different dihedrals. However, the flow is fully attached. As the angle of attack increases (b-c), wider negative-pressure regions appear near the kite nose and a leading-edge vortex starts forming. The colored streamlines show that there is a notable reduction of velocity within the vortex as compared to the rest of the fluid flow. At the highest angle of attack (d), the leading-edge recirculation bubble detaches triggering flow separation on most of the kite extrados. Finally, during the downstroke (e-f), the flow gradually reattaches at low-enough angles of attack. This behavior is observed cyclically due to the periodicity of the prescribed pitching kinematics.

Figure 8 shows the lift and drag coefficients versus α computed by the three tools for the pitching kinematics. To help interpret the unsteady results, the steady curves computed with RANS (denoted by RANS (steady)) are also shown. Results show a hysteresis on the aerodynamic coefficient response, which does not only depend on the instantaneous angle of attack but also on its history. Regarding the lift coefficient versus the angle of attack (Figure 8a), the unsteady RANS (denoted by URANS) and semi-empirical dynamic stall (denoted by Dynamic Stall) tools provide very similar outputs, verifying the second tool against URANS. During the upstroke, the lift coefficient is higher than in the steady case because the boundary layer is energised by the pith-up motion preventing separation. The downstroke is characterized by a lower C_L due to the full separation triggered by the detachment of the recirculation bubble (Figure 7d). The potential-flow tool (denoted by Potential Flow) presents a hysteresis cycle distanced from and in opposite direction to the ones predicted by the other two tools. Such big differences are due to the distinct nature of the potential-flow hysteresis. The latter is due to the change in aerodynamic normal wash on the kite surface induced by the pitching motion and the unsteady aerodynamic lags instead of viscous effects.

A remarkable match between the URANS and dynamic stall models is observed in the C_D versus α curves (Figure 8b). Similarly to the $C_L(\alpha)$ curve, the C_D is higher during the upstroke than during the downstroke for the unsteady RANS and Dynamic Stall models. The potential-flow curve presents negligible hysteresis and lower values than the other tools which can be explained by the lack of viscous effects (wall friction and separation).

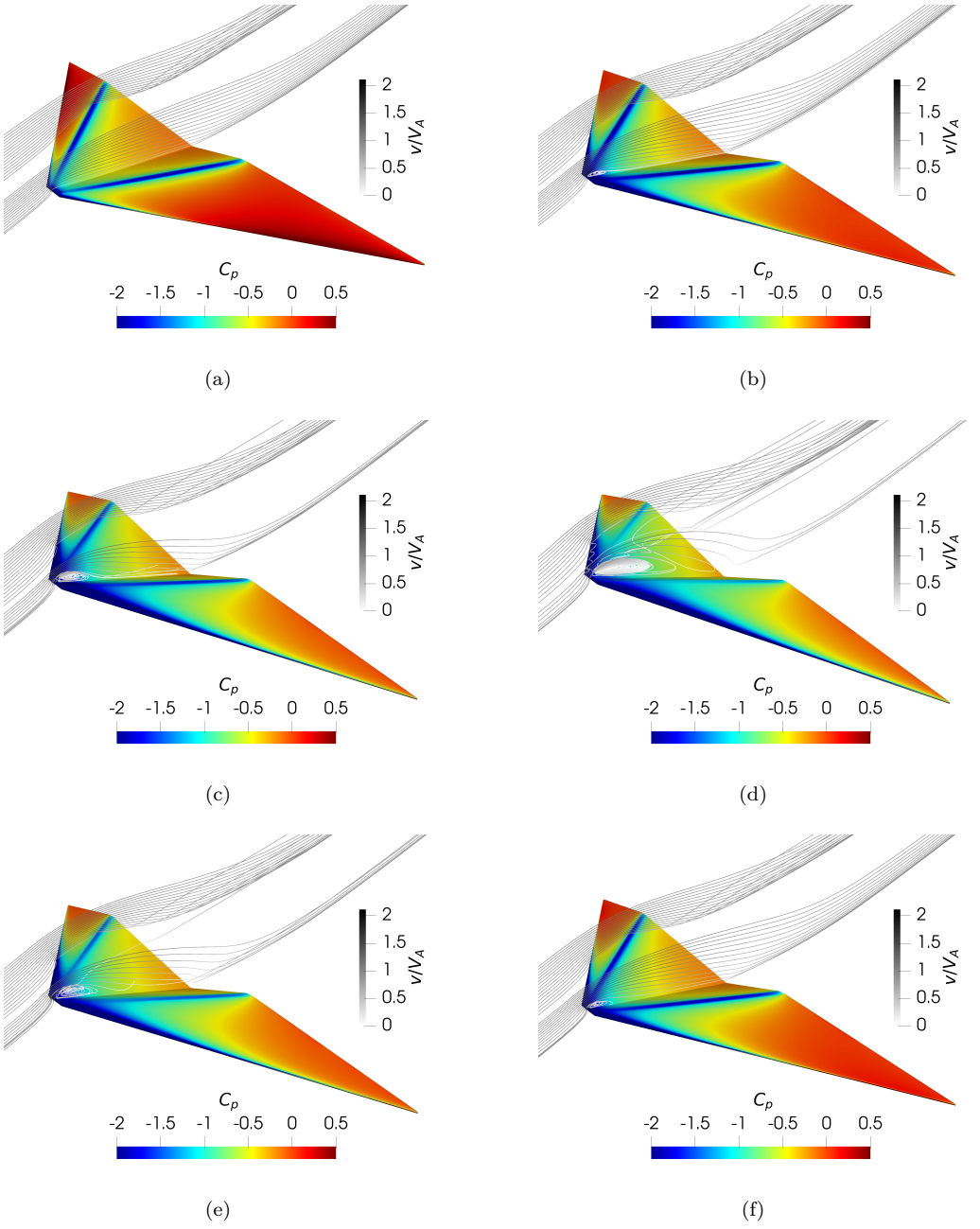

Figure 7: Unsteady RANS simulation for the pitching motion ($\dot{\alpha} \neq 0$) of cycle 2 in Figure 3. Panels (a)-(f) correspond to angles of attack of 23° (upstroke), 30° (upstroke), 35° (upstroke), 38° (downstroke), 35° (downstroke) and 30° (downstroke), respectively. The streamlines are colored with the normalized velocity (local velocity over aerodynamic velocity).

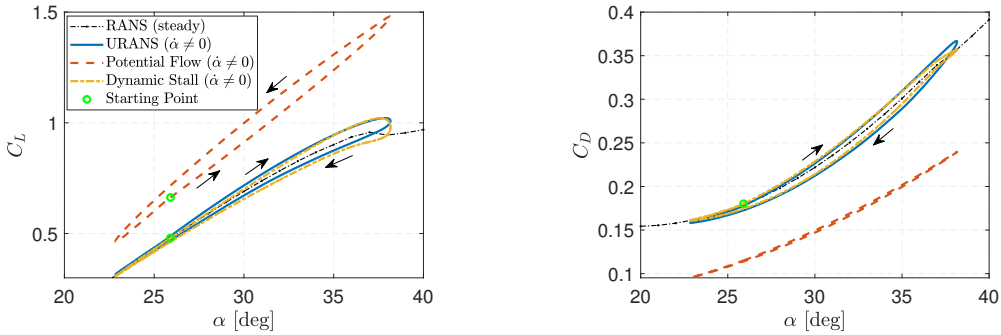

(a) (b)

Figure 8: Lift (a) and drag (b) coefficients versus the angle of attack of the RFD kite for the pitching motion of cycle 2 in Figure 3. Results from steady RANS, unsteady RANS, potential flow and semi-empirical dynamic stall models are shown.

4.2.2. *Comparison between pitching motion and pitching motion with unsteady aerodynamic velocity*

The pitching motion ($\dot{\alpha} \neq 0$) and unsteady aerodynamic velocity ($\dot{V}_A \neq 0$) of cycle 2 in Figure 3 were prescribed in the unsteady RANS tool. Figure 9 shows the lift and drag coefficients as a function of the angle of attack computed with unsteady RANS for conditions $\dot{\alpha} \neq 0$ and $\dot{V}_A \neq 0$ as compared with pitching-only conditions $\dot{\alpha} \neq 0$. The main motivation for the comparison of the two URANS simulations is to check the effects of a non-constant reduced frequency of the pitching motion and the added mass (impulsive) aerodynamic forces. The numerical tool predicts very similar hysteresis loops for both sets of kinematic conditions. Therefore, conditions $\dot{V}_A \neq 0$ do not essentially affect the dynamic stall phenomenon being the pitching motion its main driver.

5. Discussion

The comparison of the experimental results and the unsteady aerodynamic simulations revealed some important facts. The RANS simulations showed that the cyclic flow separation observed in the experiments (see Figure 2c and full video in Universidad Carlos III de Madrid (2023)) is driven by the periodic changes in the angle of attack. The simulations demonstrated that a leading-edge vortex forms and detaches cyclically triggering full flow separation on the kite extrados. An analysis of Figures 1a and 1b and Figures 8a and 8b reveals that the evolution of the lift and drag coefficients during a cycle is captured by the unsteady aerodynamic tools and the experimental and numerical results agree in terms of direction of the hysteresis loops.

However, as shown by Figure 10a, there may be additional phenomena playing an important role during the figure-of-eight maneuvers. The amplitude of the experimental cycles for the lift coefficient (dashed orange line with markers) can reach almost 100%, while the RANS simulations (blue line) predicts that dynamic stall is responsible for only about 15-20%. The important kite deformation observed in the experiments (see video in

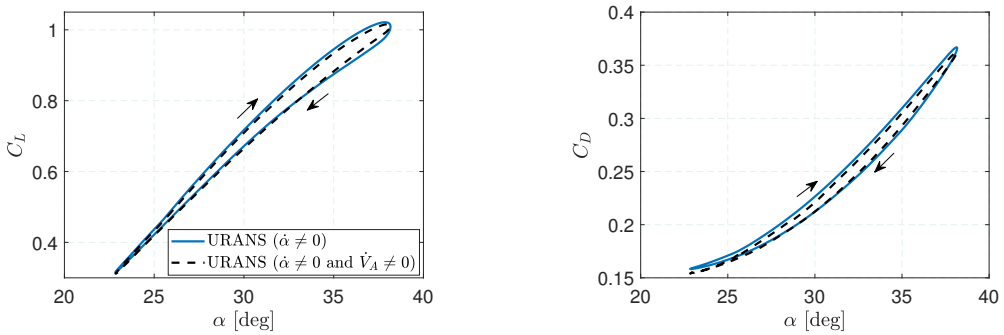

Figure 9: Lift (a) and drag (b) coefficients versus the angle of attack of the RFD kite. Results from unsteady RANS under conditions i) $\dot{\alpha} \neq 0$) and ii) $\dot{\alpha} \neq 0$ and $\dot{V}_A \neq 0$ of cycle 2 in Figure 3 are shown.

Universidad Carlos III de Madrid (2023)) suggests that aeroelastic phenomena may work collaboratively with the dynamic stall to produce high-amplitude cycles. Moreover, the RANS simulations captures very well the lower part of the cycle, where the aerodynamic loads are smaller and the kite geometry may be closer to the one used in the RANS simulations (kite geometry without any aerodynamic load).

Although a coupled fluid-structure interaction analysis is beyond the scope of this work, an extra campaign of simulations has been carried out considering a different shape of the kite (deflected shape), selected taking inspiration from the images of the experimental activity; in particular, it was decided to keep the same geometry for the outer edges of the kite and introduce a deflection (curvature) of 5% at their middle points for the central bar and the two diagonal lines joining the 2 planes at different dihedrals. A new fluid mesh was generated for the new geometry and the kite was considered as rigid for the subsequent aerodynamic simulations.

The black dashed line in Figures 10a and 10b shows the lift and drag coefficients of the deflected kite versus α computed with unsteady RANS for pitching conditions ($\dot{\alpha} \neq 0$). Regarding the $C_L(\alpha)$, the numerical hysteresis cycles of the deflected kite fits well the upper branch of the experimental results. In the case of the $C_D(\alpha)$, this match is moderate since the experimental drag coefficient, estimated through the estimation before modeling technique in Borobia-Moreno *et al.* (2021), incorrectly attributed the drag of the 2 tethers to the kite. Additionally, the amplitude of the cycle is smaller for the deformed kite due to the delay of flow separation induced by the new shape. A detailed analysis revealed that, unlike for the original geometry, the flow is not fully separated at the maximum angle of attack of the pitching motion (Figure 7d). Two conclusions can be drawn: the amplitude of the cycles observed experimentally is due in major measure to the aerostructural coupling, i.e., the kite changing its shape. However, unsteady aerodynamic phenomena (dynamic stall) are present and play a role, as suggested in (Borobia-Moreno *et al.* 2021) and corroborated by this work.

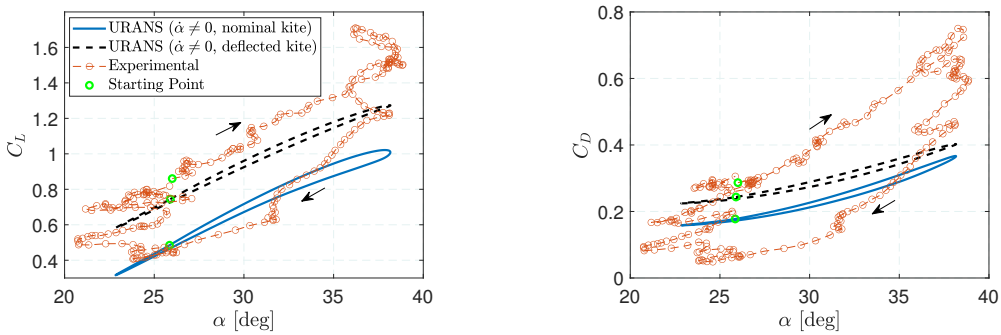

(a) (b)

Figure 10: Lift (a) and drag (b) coefficients versus the angle of attack of the RFD kite for the pitching motion of cycle 2 in Figure 3. Results from unsteady RANS of the nominal and deflected kites, and experimental data from (Borobia-Moreno *et al.* 2021) are shown.

6. Conclusions

A detailed investigation of the unsteady aerodynamics of delta kites applied to AWE during typical figure-of-eight maneuvers has been performed by combining experiments and simulations. In the first place, experimental evidences of the behavior of delta kites were shown. The post-processing of experimental data from a flight test campaign revealed strong and persistent hysteresis in the lift and drag coefficients versus the angle of attack. Moreover, an in-situ flow visualization showed periodic separation and re-attachment of the flow and significant deformations of the kite structure. Dynamic stall, driven by periodic changes in the angle of attack with amplitudes and periods of about 20° and 5s, was identified as one of the relevant unsteady phenomena involved. To allow for a deep understanding and characterization of the dynamic stall behavior, three unsteady computational aerodynamic tools were benchmarked against one another and the experimental data. The level of fidelity and computational cost ranged from low for the potential-flow tool (UnPaM) to high for RANS (SU2). Moreover, aiming at reducing the computational burden while keeping a high accuracy, a semi-empirical dynamic stall model was proposed.

The comparison between UnPaM and SU2 results for steady conditions, i.e., fixed aerodynamic velocity and angle of attack, showed that viscous effects such as recirculation bubbles, separation and wall friction, not modeled in the in-house panel method, induce moderate discrepancies in the lift and drag responses, most relevant at higher angles of attack where separation dominates. However, both tools agreed on the order of magnitude and trend of the pitch moment coefficient before stall. A local analysis of the pressure coefficient difference between the intrados and extrados ΔC_p demonstrated that despite the qualitative agreement between both tools was very good, UnPaM predicted higher suction peaks in the leading edge and the joint between the planes at different dihedral angles. This essentially leads to an overestimation of the lift coefficient by the potential-flow tool.

The unsteady aerodynamic simulations of the three tools allowed to isolate and quantify the dynamic stall phenomenon by prescribing the kite kinematics measured in the experiments. The pitching motion ($\dot{\alpha} \neq 0$) without the need of including an unsteady aerodynamic velocity ($\dot{V}_A \neq 0$) demonstrated to be the main driver of dynamic stall. The results from unsteady RANS partially explained the experimental hysteresis in the lift and drag coefficients versus the angle of attack. Analogously to the experimental observations, a leading-edge vortex that periodically forms and detaches was identified in the unsteady RANS simulations. A comparison of the three numerical tools highlighted the inability of UnPaM to capture the dynamic stall phenomenon. After fine-tuning the free parameters of the semi-empirical dynamic stall tool with steady and unsteady RANS data, a remarkable agreement with unsteady RANS was achieved on the lift and drag coefficients. Therefore, the semi-empirical tool becomes a low-cost but accurate aerodynamic tool that can be coupled with flight simulators. This is especially true for rigid AWE aircraft (fixed-wing, box-wing, etc.) performing highly-dynamic maneuvers where unsteady aerodynamics plays a fundamental role.

Motivated by the significant structural deformations experimentally observed, a deflected kite was aerodynamically analysed as a rigid body. The results revealed that a small imposed curvature (5%) on the kite central bar and the joint between planes at different dihedrals considerably shifted up the $C_L(\alpha)$ and $C_D(\alpha)$ curves. These last results suggest that, to fully reproduce the amplitude of the hysteretic response, fluid-structure coupling will need to be included. Future works will be conducted on aeroelastic modeling of delta kites to fully understand and characterize the phenomena involved during the flight of these semi-rigid kites.

Acknowledgements

This work was carried out under the framework of the GreenKite-2 project (PID2019-110146RB-I00) funded by MCIN/AEI/10.13039/501100011033.

Appendix A. Corrected wake shedding direction in UnPaM

UnPaM sheds a row of wake panels from the trailing edge in a user-defined direction at every time step of an unsteady simulation (Cavallaro *et al.* 2015; Castro-Fernández *et al.* 2021). Among the infinite existing shedding directions, Ref. (Mangler & Smith 1970) demonstrated that the direction defined by the bi-sector of the two surfaces gathering at the trailing edge was physically representative for thick bodies. In addition, CFD data visualizations of the RFD kite shows that the flow leaves the trailing edge tangentially to the trailing edge surfaces. An implementation for thin surfaces following (Mangler & Smith 1970) and the observations in the CFD data has been carried out in this work by defining a preliminary wake shedding direction $\boldsymbol{V}_s'$ as

$$\begin{aligned} \boldsymbol{V}_s' &= \left(\frac{\boldsymbol{V}_A}{V_A} \cdot \boldsymbol{V}_t\right) \boldsymbol{V}_t + \left(\frac{\boldsymbol{V}_A}{V_A} \cdot \boldsymbol{V}_n\right) \boldsymbol{V}_n, \\ \boldsymbol{V}_t &= \frac{\boldsymbol{P}_{i,j+1}^{TE} - \boldsymbol{P}_{i,j}^{TE}}{\left|\boldsymbol{P}_{i,j+1}^{TE} - \boldsymbol{P}_{i,j}^{TE}\right|}, \quad \boldsymbol{V}_n = \frac{\boldsymbol{P}_{i,j}^{TE} - \boldsymbol{P}_{i-1,j}^{TE}}{\left|\boldsymbol{P}_{i,j}^{TE} - \boldsymbol{P}_{i-1,j}^{TE}\right|}, \end{aligned} \tag{11}$$

where $\boldsymbol{V_t}$ and $\boldsymbol{V_n}$ are two coplanar unitary vectors defined from three corner points of the trailing edge quadrilateral panels as shown in Figure 11. Equation (11) represents a

projection of the aerodynamic velocity on a plane tangential to the trailing edge surface. Then, a final shedding direction is defined by using part of the information from $\boldsymbol{V}_s'$ and canceling the y_W-axis component to avoid nonphysical crossings of wake panels shed by different trailing edge segments,

$$\boldsymbol{V}_s = \frac{\boldsymbol{V}_s' \cdot \boldsymbol{i}_W + \boldsymbol{V}_s' \cdot \boldsymbol{k}_W}{|\boldsymbol{V}_s' \cdot \boldsymbol{i}_W + \boldsymbol{V}_s' \cdot \boldsymbol{k}_W|}. \tag{12}$$

This methodology ensures that the shedding direction of every trailing edge panel follows the aerodynamic velocity and is quasi-contained in the panel plane. The first row of wake panels is shed by creating a row of new wake points as

$$\boldsymbol{P}^W_{i+1,j} = \boldsymbol{P}^{TE}_{i,j} + V_A \Delta t \boldsymbol{V}_s, \quad \boldsymbol{P}^W_{i+1,j+1} = \boldsymbol{P}^{TE}_{i,j+1} + V_A \Delta t \boldsymbol{V}_s, \tag{13}$$

with Δt the time step of the aerodynamic simulation. The rest of the wake points are displaced by multiplying the total velocity induced by both the kinematic conditions and the singularities placed on the body and wake by Δt. In steady computations, only one row of long wake panels is shed by using Equation (13) and $\Delta t = \Delta X^W / V_A$, where $\Delta X^W = 50$ m is a user-defined wake length.

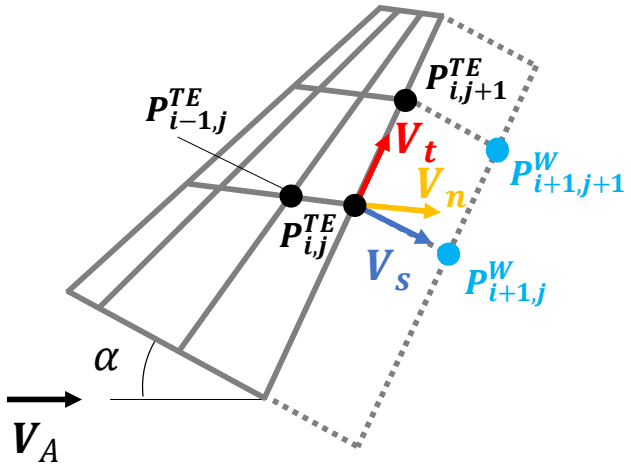

Figure 11: Sketch of a generic wing and shed wake discretized with the vortex lattice method implemented in UnPaM.

Appendix B. State-space equations of the semi-empirical dynamic stall aerodynamic model

Considering the state-space model presented in Section 3.3, the first state equation is a lag equation for the effective angle of attack $\overline{\alpha}$,

$$\dot{\overline{\alpha}}' = \frac{\overline{\alpha} - \overline{\alpha}'}{T_f}, \tag{14}$$

with T_f one of the constant dynamic parameters $\boldsymbol{\theta}^D$ that account for the stall delay induced by the pitching motion. The resulting $\overline{\alpha}$ at every time step is used to monitor

the leading edge separation through the detachment of the leading edge vortex which is triggered at time t_{v0} when conditions $\overline{\alpha} \geq \alpha_{DS}(\dot{\alpha})$ and $\dot{\overline{\alpha}}\ \overline{\alpha} \geq 0$ are met, with

$$\alpha_{DS}(\dot{\alpha}) = \frac{-b_{DS} + \sqrt{b_{DS}^2 - 4a_{DS}\left(c_{DS} - \frac{\dot{\alpha}c_s}{2\overline{V}_A}\right)}}{2a_{DS}}, \tag{15}$$

expressed in degrees and a_{DS}, b_{DS}, c_{DS} being fitting parameters from experiments of pitching airfoils directly taken from Boutet *et al.* (2020) (see Table 3).

Another lag equation is needed for the trailing edge separation point with the same time delay T_f (Boutet *et al.* 2020),

$$\dot{f}' = \frac{f(\overline{\alpha}) - f'}{T_f}, \tag{16}$$

where $f(\overline{\alpha})$ was pre-computed by using the Kirchhoff model (Thwaites 1960). The latter was used to relate the location of the flow separation point f with the CFD ($C_L^{CFD,S}(\alpha)$) and potential-flow ($C_L^{P,S}(\alpha)$) lift coefficients of the RFD kite for α in static conditions,

$$f(\alpha) = \left(2\sqrt{\frac{C_L^{CFD,S}(\alpha)}{C_L^{P,S}(\alpha)}} - 1\right)^2, \tag{17}$$

where both coefficients were obtained from pre-computed steady lift coefficient versus angle of attack curves with SU2 and UnPaM, respectively. The original Leishman-Beddoes model (Leishman & Beddoes 1989) employed a piecewise fit with 3 free parameters to approximate the experimental $f(\alpha)$. In this work, due to the abundant CFD and potential-flow data, a linear interpolation was used to look up the lift coefficients in Equation 17.

The third differential equation governs the lag of the lift coefficient due to the change of circulation for oscillatory motion C_L^v,

$$\dot{C}_L^v = \dot{C}_v - \frac{C_L^v}{T_v}, \tag{18}$$

with T_v a constant time delay (dynamic parameter $\boldsymbol{\theta}^D$), C_v an estimate of the change in circulation computed as

$$C_v = C_L^{P,Dc} - C_L^f, \tag{19}$$

where $C_L^{P,Dc}$ is the circulatory part of the potential-flow lift coefficient under dynamic conditions and C_L^f is the unsteady lift coefficient due to the trailing edge separation process given by

$$C_L^f = C_L^{P,S}(\overline{\alpha})f' + C_L^{fs}(\overline{\alpha})(1 - f'), \quad C_L^{fs}(\overline{\alpha}) = \frac{C_L^{CFD,S}(\overline{\alpha}) - C_L^{P,S}(\overline{\alpha})f(\overline{\alpha})}{1 - f(\overline{\alpha})}, \tag{20}$$

with C_L^{fs} the fully-separated lift coefficient. Equation 20 computes C_L^f as a weighted average between the fully-attached and fully-separated lift coefficients (Hansen *et al.* 2004). Additionally, this work uses a model originally proposed by Sheng et al. (Sheng *et al.* 2008) for the overshoot in the lift and pitch moment coefficients due to the leading edge vortex shedding process,

$$\Delta C_L^v = B_1(f' - f(\overline{\alpha}))V_\chi, \quad \Delta C_m^v = B_2 \Delta C_L^v, \quad V_\chi = \left|\sin\left(\frac{\pi(t - t_{v0})}{2T_{vl}}\right)\right|, \tag{21}$$

where B_1 and B_2 are two parameters experimentally identified in Boutet *et al.* (2020) (see Table 3). This overshoot is only present from the moment in which the leading edge vortex detaches from the leading edge (t_{v0}) until the leading edge vortex clears the trailing edge ($t_{v0} + T_{vl}$, where T_{vl} is another dynamic parameter within $\boldsymbol{\theta}^D$). Additional lift ($C_L^{P,Di}$), drag ($C_D^{P,Di}$) and pitch moment ($C_m^{P,Di}$) coefficients contributions were added in the current work to account for impulsive terms. By summing all the lift contributions, the dynamic stall lift coefficient C_L^{DS} reads,

$$C_L^{DS} = C_L^f + C_L^v + C_L^{P,Di} + \Delta C_L^v. \tag{22}$$

The dynamic stall drag coefficient was computed by adding unsteady variations to the steady drag computed with CFD $C_D^{CFD,S}$ which already contains 3D and viscous drag effects (Hansen *et al.* 2004),

$$C_D^{DS} = C_D^{CFD,S}(\alpha) + \Delta C_D^{ind} + \Delta C_D^f + C_D^{P,Di}, \tag{23}$$

where ΔC_D^{ind} and ΔC_D^f are given by

$$\Delta C_D^{ind} = C_L^{DS}(\alpha - \overline{\alpha}), \quad \Delta C_D^f = \left(C_D^{CFD,S}(\alpha) - C_{D0}^{CFD,S}\right)\left[\left(\frac{1-\sqrt{f'}}{2}\right)^2 - \left(\frac{1-\sqrt{f(\overline{\alpha})}}{2}\right)^2\right], \tag{24}$$

and account for the drag induced by the unsteady pitching motion and the pressure drag contribution due to trailing edge separation, respectively. The latter is computed by multiplying the steady pressure drag, i.e., total CFD drag minus a constant viscous drag (zero-lift CFD drag, $C_{D0}^{CFD,S}$, in Table 3), by a modulation factor that depends on the lag between f' and $f(\overline{\alpha})$ (Hansen *et al.* 2004).

The dynamic stall pitch moment coefficient reads,

$$C_m^{DS} = C_{m0}^{CFD,S} + C_m^f + C_m^v + C_m^{P,Di} + \Delta C_m^v, \tag{25}$$

where $C_{m0}^{CFD,S}$ is the zero-lift pitch moment obtained from the static CFD data (Table 3), C_m^f and C_m^v are the contributions due to separation and change of circulation, respectively, computed by assuming that C_L^f and C_L^v are applied at the center of pressure of our typical section,

$$C_m^f = C_L^f\left(a - [g(\overline{\alpha}') + 1/4]\right), \quad C_m^v = C_L^v\left(a - [g(\overline{\alpha}') + 1/4]\right), \tag{26}$$

with $g(\overline{\alpha})$ the position of the center of pressure measured from the quarter-chord of the typical section (see a depiction in Figure 4b) computed as described in Section B.1. To complete the space vector $\boldsymbol{y}$, the lateral-directional aerodynamic coefficients C_Y^{DS}, C_l^{DS}, C_n^{DS} are given by their potential-flow unsteady counterparts, i.e., $C_j^{DS} = C_j^{P,Dc} + C_j^{P,Di}, j = Y, l, n$, since it is assumed that the dynamic stall phenomenon does not affect them.

B.1. Location of the center of pressure

The center of pressure is assumed to be located at the quarter-chord at the zero-lift angle of attack and move downstream as the angle of attack increases (see Figure 4b). In static conditions, this assumption leads to

$$C_m^{CFD,S}(\alpha)\big|_{1/4c_s} = C_{m0}^{CFD,S}\Big|_{1/4c_s} - C_L^{CFD,S}(\alpha)g(\alpha)\left[\frac{c_s}{c}\right], \tag{27}$$

with $C_{m0}^{CFD,S}\Big|_{1/4c_s}$ and $C_m^{CFD,S}(\alpha)\big|_{1/4c_s}$ the zero-lift and current (at α) pitch moment coefficients about the quarter-chord computed with SU2. From Equation 27, $g(\alpha)$ is isolated,

$$g(\alpha) = \frac{C_{m0}^{CFD,S}\Big|_{1/4c_s} - C_m^{CFD,S}(\alpha)\big|_{1/4c_s}}{C_L^{CFD,S}(\alpha)\left[\frac{c_s}{c}\right]}. \tag{28}$$

Leishman and Beddoes (Leishman & Beddoes 1989) approximated g with a 4-parameter fit of experimental data. In the current work, the values for $C_{m0}^{CFD,S}\Big|_{1/4c_s}$, $C_m^{CFD,S}(\alpha)\big|_{1/4c_s}$ and $C_L^{CFD,S}(\alpha)$ were looked up from a steady RANS database pre-computed with SU2.

References

Bangga, G., Lutz, T. & Arnold, M. 2020 An improved second-order dynamic stall model for wind turbine airfoils. *Wind Energy Sci.* **5**, 1037–1058.

Borobia, R., Sánchez-Arriaga, G., Serino, A. & Schmehl, R. 2018 Flight-Path Reconstruction and Flight Test of Four-Line Power Kites. *J. Guid. Control. Dyn.* **41** (12), 2604–2614.

Borobia-Moreno, R., Ramiro-Rebollo, D., Schmehl, R. & Sánchez-Arriaga, G. 2021 Identification of kite aerodynamic characteristics using the estimation before modeling technique. *Wind Energy* **24** (6), 596–608.

Bosch, A., Schmehl, R., Tiso, P. & Rixen, D. 2014 Dynamic nonlinear aeroelastic model of a kite for power generation. *J. Guid. Control. Dyn.* **37** (5), 1426–1436.

Boutet, J., Dimitriadis, G. & Amandolese, X. 2020 A modified Leishman – Beddoes model for airfoil sections undergoing dynamic stall at low Reynolds numbers. *J. Fluids Struct.* **93**, 102852.

Breukels, J., Schmehl, R. & Ockels, W. 2013 Aeroelastic Simulation of Flexible Membrane Wings based on Multibody System Dynamics. In *Airborne Wind Energy. Ser. Green energy Technol.*, pp. 287–305.

Buffoni, M., Galletti, B., Ferreau, J., Fagiano, L. & Mercangoez, M. 2014 Active pitch control of tethered wings for airborne wind energy. In *53rd IEEE Conf. Decis. Control*, pp. 4893–4898. IEEE.

Candade, A. A., Ranneberg, M. & Schmehl, R. 2020 Structural analysis and optimization of a tethered swept wing for airborne wind energy generation. *Wind Energy* **23** (4), 1006–1025.

Castro-Fernández, I., Borobia-Moreno, R., Cavallaro, R. & Sánchez-Arriaga, G. 2021 Three-Dimensional Unsteady Aerodynamic Analysis of a Rigid-Framed Delta Kite Applied to Airborne Wind Energy. *Energies* **14** (23), 8080.

Castro-Fernández, I., DeLosRíos-Navarrete, F., Borobia-Moreno, R., Fernández-Jiménez, M., García-Cousillas, H., Zas-Bustingorri, M., Ghobaissi, Á. T., López-Vega, F., Best, K., Cavallaro, R. & Sánchez-Arriaga, G. 2023 Automatic testbed with a visual motion tracking system for airborne wind energy applications. *Wind Energy* **26** (4), 388–401.

Cavallaro, R., Nardini, M. & Demasi, L. 2015 Amphibious prandtlplane: Preliminary design aspects including propellers integration and ground effect. In *56th AIAA/ASCE/AHS/ASC Struct. Struct. Dyn. Mater. Conf.*, pp. 1–27.

Cayon, O., Gaunaa, M. & Schmehl, R. 2023 Fast Aero-Structural Model of a Leading-Edge Inflatable Kite. *Energies* **16** (7), 3061.

Damiani, R., Wendt, F., Jonkman, J. & Sicard, J. 2019 A vortex step method for nonlinear airfoil polar data as implemented in KiteAeroDyn. In *AIAA Scitech 2019 Forum*, pp. 1–11.

De Fezza, G. D. & Barber, S. 2022 Parameter analysis of a multi-element airfoil for application to airborne wind energy. *Wind Energy Sci.* **7**, 1627–1640.

Economon, T. D., Palacios, F., Copeland, S. R., Lukaczyk, T. W. & Alonso, J. J. 2016 SU2: An open-source suite for multiphysics simulation and design. *AIAA J.* **54** (3), 828–846.

Eijkelhof, D., Buendía, G. & Schmehl, R. 2023 Low- and High-Fidelity Aerodynamic Simulations of Box Wing Kites for Airborne Wind Energy Applications. *Energies* **16** (7), 3008.

Ekaterinaris, J. A. & Platzer, M. F. 1997 Computational prediction of airfoil dynamic stall. *Prog. Aerosp. Sci.* **33** (11-12), 759–846.

Fasel, U., Keidel, D., Molinari, G. & Ermanni, P. 2017 Aerostructural optimization of a morphing wing for airborne wind energy applications. *Smart Mater. Struct.* **26**, 1–11.

Fasel, U., Tiso, P., Keidel, D., Molinari, G. & Ermanni, P. 2019 Reduced-order dynamic model of a morphing airborne wind energy aircraft. *AIAA J.* **57** (8), 3586–3598.

Fechner, U., van der Vlugt, R., Schreuder, E. & Schmehl, R. 2015 Dynamic model of a pumping kite power system. *Renew. Energy* **83**, 705–716.

Folkersma, M., Schmehl, R. & Viré, A. 2019 Boundary layer transition modeling on leading edge inflatable kite airfoils. *Wind Energy* **22** (7), 908–921.

Folkersma, M., Schmehl, R. & Vire, A. 2020 Steady-state aeroelasticity of a ram-air wing for airborne wind energy applications. *J. Phys. Conf. Ser.* (September), 1–13.

Fonzi, N., Brunton, S. L. & Fasel, U. 2020 Data-driven nonlinear aeroelastic models of morphing wings for control. In *R. Soc. A*, pp. 1–23.

Fonzi, N., Cavalieri, V., Gaspari, A. D. & Ricci, S. 2022 Extended computational capabilities for high-fidelity fluid – structure simulations. *J. Comput. Sci.* **62** (May), 1–18.

Gaunaa, M., Carqueija, F. P. P., Réthoré, P.-E. & Sørensen, N. N. 2011 A computationally efficient method for determining the aerodynamic performance of kites for wind energy applications. In *EWEA 2011*, pp. 1–11.

Haas, T., De Schutter, J., Diehl, M. & Meyers, J. 2022 Large-eddy simulation of airborne wind energy farms. *Wind Energy Sci.* **7** (3), 1093–1135.

Hansen, M., Gaunaa, M. & Aagaard Madsen, H. 2004 A Beddoes-Leishman type dynamic stall model in state-space and indicial formulations. *Tech. Rep.*. Forskningscenter Risoe.

Hirsch, C. 1984 *Numerical computation of internal and external flows*. New York: Wiley.

Ko, A. P., Smidt, S., Schmehl, R. & Mandru, M. 2023 Optimization of a Multi-Element Airfoil for a Fixed-Wing Airborne Wind Energy System. *Energies* **16** (8), 3521.

Leishman, J. . & Beddoes, T. S. 1989 A Semi-Empirical Model for Dynamic Stall. *J. Am. Helicopter Soc.* pp. 3–17.

Leloup, R., Roncin, K., Bles, G. & Leroux, J.-b. 2013 Estimation of the Lift-to-Drag Ratio Using the Lifting Line Method : Application to a Leading Edge Inflatable Kite. In *Airborne Wind Energy. Ser. Green energy Technol.*, pp. 339–355.

Leuthold, R. 2015 Multiple-Wake Vortex Lattice Method for Membrane-Wing Kites. *Tech. Rep.* December 2015. Delft University of technology.

Mangler, K. W. & Smith, J. H. B. 1970 Behaviour of the Vortex Sheet at the Trailing Edge of a Lifting Wing. *Aeronaut. J. R. Aeronaut. Soc.* **74**, 906–908.

McAlister, K. W., Pucci, S. L., McCroskey, W. J. & Carr, L. W. 1982 An Experimental Study of Dynamic Stall on Advanced Airfoil Sections Volume 2. Pressure and Force Data. *Tech. Rep.*. NASA.

Mehr, J., Alvarez, E. J. & Ning, A. 2020 Unsteady aerodynamic analysis of wind harvesting aircraft. In *Aiaa Aviat. 2020 Forum*, pp. 1–13.

Menter, F. R. 1994 Two-equation eddy-viscosity turbulence models for engineering applications. *AIAA J.* **32** (8), 1598–1605.

Nardini, M. 2014 A Computational Multi-purpose Unsteady Aerodynamic Solver for the Analysis of Innovative Wing Configurations, Helicopter Blades and Wind Turbines. *Tech. Rep.*. University of Pisa.

Oehler, J. & Schmehl, R. 2019 Aerodynamic characterization of a soft kite by in situ flow measurement. *Wind Energy Sci.* **4** (1), 1–21.

Palacios, F., Colonno, M. R., Aranake, A. C., Campos, A., Copeland, S. R., Economon, T. D., Lonkar, A. K., Lukaczyk, T. W., Taylor, T. W. R. & Alonso, J. J. 2013 Stanford University Unstructured (SU 2): An open-source integrated computational environment for multi-physics simulation and design . In *51st AIAA Aerosp. Sci. Meet. Incl. New Horizons Forum Aerosp. Expo.*, pp. 1–60.

Palacios, F., Economon, T. D., Aranake, A. C., Copeland, S. R., Lonkar, A. K., Lukaczyk, T. W., Manosalvas, D. E., Naik, K. R., Padr, A. S., Tracey, B., Variyar,

A. & Alonso, J. J. 2014 Stanford University Unstructured (SU 2): Open-source Analysis and Design Technology for Turbulent Flows. In *52nd Aerosp. Sci. Meet.*, pp. 1–33.

Pynaert, N., Haas, T., Wauters, J., Crevecoeur, G. & Degroote, J. 2023 Wing Deformation of an Airborne Wind Energy System in Crosswind Flight Using High-Fidelity Fluid – Structure Interaction. *Energies* **16** (2), 602.

Sánchez-arriaga, G., Pastor-rodríguez, A., Sanjurjo-rivo, M. & Schmehl, R. 2019 A lagrangian flight simulator for airborne wind energy systems. *Appl. Math. Model.* **69**, 665–684.

Schmidt, E., De Lellis Costa De Oliveira, M., Saraiva Da Silva, R., Fagiano, L. & Trofino Neto, A. 2020 In-Flight Estimation of the Aerodynamics of Tethered Wings for Airborne Wind Energy. *IEEE Trans. Control Syst. Technol.* **28** (4), 1309–1322.

Sheng, W., Chan, W. & Galbraith, R. 2012 Advancement of aerofoil section dynamic stall synthesis methods for rotor design. *Aeronaut. J.* **116**, 521–539.

Sheng, W., Galbraith, R. A. M. & Coton, F. N. 2008 A Modified Dynamic Stall Model for Low Mach Numbers 1. *J. Sol. Energy Eng.* **130** (August 2008), 1–10.

Spentzos, A., Barakos, G. N., Badcock, K. J., Richards, B. E., Coton, F. N., Galbraith, R. A. D., Berton, E. & Favier, D. 2007 Computational fluid dynamics study of three-dimensional dynamic stall of various planform shapes. *J. Aircr.* **44** (4), 1118–1128.

Thedens, P. & Schmehl, R. 2023 An Aero-Structural Model for Ram-Air Kite Simulations. *Energies* **16** (6), 2603.

Thwaites, B. 1960 *Incompressible aerodynamics : an account of the theory and observation of the steady flow of incompressible fluid past aerofoils, wings and other bodies*. New York: Dover Publications.

Tran, C. T. & Petot, D. 1980 Semi-empirical model for the dynamic stall of airfoils in view of the application to the calculation of responses of a helicopter blade in forward flight. In *Sixth Eur. Rotorcr. Powered Lift Aircr. Forum*, pp. 1–23.

Universidad Carlos III de Madrid 2023 UC3M-CT Ingenieros flight campaign (April 23). [https://www.youtube.com/watch?v=W9tkuaRj83w].

Vermillion, C., Cobb, M., Fagiano, L., Leuthold, R., Diehl, M., Smith, R. S., Wood, T. A., Rapp, S., Schmehl, R., Olinger, D. & Demetriou, M. 2021 Electricity in the air: Insights from two decades of advanced control research and experimental flight testing of airborne wind energy systems. *Annu. Rev. Control* **52** (December 2020), 330–357.

Vimalakanthan, K., Caboni, M., Schepers, J., Pechenik, E. & P.Williams 2018 Aerodynamic analysis of Ampyx's airborne wind energy system. *J. Phys. Conf. Ser.* **1037**, 1–10.

Viré, A., Demkowicz, P., Folkersma, M., Roullier, A. & Schmehl, R. 2020 Reynolds-averaged Navier-Stokes simulations of the flow past a leading edge inflatable wing for airborne wind energy applications. *J. Phys. Conf. Ser.* **1618** (3).

Viré, A., Lebesque, G., Folkersma, M. & Schmehl, R. 2022 Effect of Chordwise Struts and Misaligned Flow on the Aerodynamic Performance of a Leading-Edge Inflatable Wing. *Energies* **15** (4), 1450.

White, F. M. 1974 *Viscous Fluid Flow*. New York: McGraw-Hill.

Wijnja, J., Schmehl, R., Breuker, R. D., Jensen, K. & Lind, D. V. 2018 Aeroelastic Analysis of a Large Airborne Wind Turbine. *J. Guid. Control. Dyn.* **41**, 1–12.

Wilcox, D. C. 2006 *Turbulence Modelling for CFD*, 3rd edn. DCW Industries.

Paper 3

3

Automatic Testbed with a Visual Motion Tracking System for Airborne Wind Energy Applications

I. Castro-Fernández[1], F. DeLosRíos-Navarrete[1], R. Borobia-Moreno[2], M. Fernández-Jiménez[1], H. García-Cousillas[1], M. Zas-Bustingorri[1], A. T. Ghobaissi[1], F. Lopez-Vega[1], K. Best[1], R. Cavallaro[1] & G. Sánchez-Arriaga[1]

[1] Departamento de Ingeniería Aeroespacial, Universidad Carlos III de Madrid, Leganés, 28911 Madrid, Spain

[2] Centro de Experimentación de "El Arenosillo" (CEDEA), Instituto Nacional de Técnica Aeroespacial, Mazagón, 21130 Huelva, Spain

Wind Energy (2023), vol. **26(4)**, 388-401

The architecture and a flight test campaign of a small-scale testbed aimed at aerodynamic and dynamic characterization of airborne wind energy systems are presented. The testbed involves a two-line rigid-framed delta kite and an automatic ground station for the lateral control of the kite and reel-in/reel-out of the two tethers. The environment, and the states of the kite, the tethers and the actuators are measured by a set of on-ground and onboard sensors that include, among others, an inertial measurement unit, GNSS receivers, load cells, actuator encoders, a weather station, and a visual motion tracking (VMT) system based on three cameras and an artificial neural network (YOLOv2). The results of a five-minute flight, including the take-off, crosswind flight, and landing, were used to analyze the capabilities of the testbed. It was shown that the time derivative of the kite course angle exhibits a linear correlation with both the delayed steering input and the delayed differential tether tension, being the dispersion lower for the latter. The intrinsic and extrinsic calibrations proposed for the VMT system led to a good agreement between the estimation of the kite position and course angle provided by the VMT system and the onboard computer. Moreover, although the YOLOv2 algorithm failed in the detection of the kite within around 5% of the images, the simultaneous non-detection from the three cameras was below 0.1% during the full flight. Such a reliability suggests that a VMT system can be used as a redundant or backup sensor for the GNSS.

Keywords: Artificial neural network; kalman filter; open-loop control; rigid-framed delta kite; visual motion tracking

1. Introduction

Airborne wind energy (AWE) is an emerging field within the wind power sector that aims at harvesting high-altitude wind energy by using tethered aircraft. AWE systems are characterized by a low use of materials, an efficient harvesting of the wind energy by reaching high operational altitudes, and adaptability to changing wind conditions. Studies on commercial feasibility pointed out the large energy harnessing potential but also the lack of full commercial maturity that such systems present to date (Ecorys 2018;

U.S. Department of Energy 2021). Since the introduction of the crosswind kite power concept in 1980 (Loyd 1980), AWE technology matured extraordinarily, specially during the last two decades (Cherubini *et al.* 2015; Watson *et al.* 2019; Vermillion *et al.* 2021). Several AWE machines were developed ranging from small-scale prototypes (van der Vlugt *et al.* 2013; Milanese *et al.* 2013; Deodhar *et al.* 2017; Heudorfer & Dobler 2022) to pre-commercial machines (Erhard & Strauch 2015; Licitra *et al.* 2019; Salma *et al.* 2020) (Refs. Cherubini *et al.* (2015); Vermillion *et al.* (2021) contain a comprehensive review of AWE typology). Some of them are today in the range of around 100 kW and ready or close to be commercialized (Kitepower 2022; SkySails Power 2022).

In parallel with the development of fully operational and large machines, the AWE community has also prepared small-scale infrastructures fully dedicated to the flight testing and the experimental study of a large variety of relevant topics like the dynamics, control, estimation, and aerodynamics of AWE systems. These infrastructures include for instance laboratory test platforms for single-tethered aircraft for the static and dynamic characterization by means of a pendulum-like facility (Healy *et al.* 2022) and a carousel system for the study of the launch & recovery of unpropelled tethered airplanes (Geebelen *et al.* 2013). Takeoff and landing of a rigid AWE airplane was tested with a small-scale outdoor system consisting of a winch and a linear motion system (Fagiano *et al.* 2017*a*,*b*, 2018) demonstrating the feasibility of short-run takeoff and landing of AWE systems. Extensive flight testing of membrane wings was performed with small-scale ground-based test benches provided with a linear motion system for the lateral autonomous control and a linear carriage for the powering/de-powering inputs (Fagiano & Marks 2015). Test platforms based on vehicles towing kites and moving in straight paths to mimic the desired wind conditions was also performed by using a ground-based 3 motor-drum system (Hummel *et al.* 2019) and a kite control unit suspended at less than 1 meter from the towing vehicle (Rushdi *et al.* 2020).

All these small-scale infrastructures involve sensor fusion setups and algorithms mostly targeted (but not limited) to the dynamic characterization and closed-loop control design of AWE systems (Fagiano *et al.* 2014*b*; Wood *et al.* 2015; Coleman *et al.* 2017; Costello *et al.* 2018; Schmidt *et al.* 2020; Fagiano *et al.* 2014*a*). Most of them included onboard equipment like an inertial measurement unit (IMU), global navigation satellite system (GNSS) receivers, load cells and line angle sensors, among others. It was demonstrated that line angle sensors jeopardized the estimations due to tether sagging and tether dynamics when compared with range sensors (Millane *et al.* 2015). Other measurements like in-situ flow measurements were obtained for the first time by using a vane-pitot tube system attached to the bridle lines of a leading-edge inflatable (LEI) kite (Oehler & Schmehl 2019). With the same purpose, a multihole pitot tube was boarded on a rigid-framed delta (RFD) kite to get accurate (about 1°) and time-resolved measurements of the aerodynamic velocity vector, i.e., angle of attack, sideslip angle and airspeed magnitude (Borobia-Moreno *et al.* 2021). The in-situ knowledge of the aerodynamic velocity vector was showed to be essential to uncover underlying unsteady aerodynamic phenomena (Borobia-Moreno *et al.* 2021; Castro-Fernández *et al.* 2021). Regarding estimation techniques, extended Kalman filtering has been broadly used with purely kinematic process models (Fagiano *et al.* 2014*a*), in the form of a multiplicative extended Kalman filter to avoid singularities in the covariance matrix due to the use of quaternions (Millane *et al.* 2015) and including the aerodynamic forces and torques in the state vector (Borobia *et al.* 2018; Schmidt *et al.* 2020).

Visual sensors were also applied to AWE. The 3D deformation of ram-air kites was reconstructed by photogrammetry and compared to laser scanning techniques in a wind tunnel facility (de Wachter 2008). Qualitative information of a LEI kite deformation and its bridle system as a response to powering/de-powering control was retrieved from in-flight recordings of a camera attached to the kite control unit (Oehler & Schmehl 2019). Although there are some exceptions (Hesse *et al.* 2018; Geebelen *et al.* 2013), the use of visual motion tracking (VMT) sensors applied to small-scale AWE testbeds did not receive too much attention in the past. The position of an AWE system was tracked with one camera by employing a combination of object detection (accuracy) based on color features and motion tracking (speed) algorithms (Hesse *et al.* 2018). However, the object detector employed in Hesse *et al.* (2018) required a labeled sub-image containing the kite at the beginning of the tracking process or when the kite left the field of view of the camera. A testbed with stereo vision capabilities by using a pair of cameras that rotated with a carousel system was also developed (Geebelen *et al.* 2013). The aircraft position and attitude were inferred by tracking three markers (red, green and blue LEDs) attached to the aircraft with both cameras. Besides AWE, machine learning algorithms have enhanced the detection capabilities of VMT systems by using neural networks (Smolyanskiy *et al.* 2018; Shahzad *et al.* 2020).

This work contributes to the progress of AWE systems by implementing some key improvements in the testbed of Borobia *et al.* (2018), which was shown to be an effective infrastructure for the aerodynamic characterization of a two-line RFD kite (Borobia-Moreno *et al.* 2021). As explained in Section 2, the old control bar used by a pilot to steer the kite in previous works (Borobia *et al.* 2018; Borobia-Moreno *et al.* 2021) was substituted by a ground station equipped with an automatic control system based on a linear actuator and a winch. The former GNSS sensor and the wind station were also upgraded. Instead of estimating the kite state by post processing the measurements with an extended Kalman filter (EKF) (Borobia-Moreno *et al.* 2021), the dynamic state of the kite was estimated by the onboard computer by fusing GNSS, IMU and magnetic sensors measurements in a built-in Kalman filter and then sent to the ground station by telemetry. Finally, a novel three-camera VMT system that combines the images of the cameras and an artificial neural network (YOLOv2 algorithm) for the estimation of the kite position and course angle was added to the testbed (see Section 3). Unlike Ref. Hesse *et al.* (2018), our VMT system tracks the kite by autonomously detecting it in every frame through a trained artificial neural network ensuring tracking robustness. The capabilities of the testbed are presented in Section 4, where the results of a flight campaign are shown. The conclusions are summarized in Section 5.

2. Testbed for airborne wind energy systems

2.1. Mechanical design of the ground-based control system

The ground segment of the testbed, hereafter called the ground control unit (GCU), consists of structural elements, a set of actuators to steer the two-line kite and sensors to measure its dynamic state. Panel (a) and (b) in Figure 1 show the testbed (GCU and the RFD kite) and a 3D model of the GCU, respectively. The structural integrity of the testbed is provided by a 10 mm thick aluminum base plate, a frame composed of standard aluminium 30x30 mm profiles and the elements to support the actuators. It also includes a table to place the operator's control joystick and a laptop. The two-line RFD kite is

connected to the GCU by two tethers of equal length L_T that pass through a system of metallic pulleys equipped with 3D printed covers to guide them and a mobile carriage linked to a linear actuator.

The GCU admits two alternative configurations. In the so-called *winch configuration* the two tethers are wound in the winch that is showed at the top of panel (b) in Figure 1. The winch is connected to a gearbox and a motor for the automatic reel-in and reel-out of the tethers. This configuration allows to control L_T, but the tether tensions are not measured. In the so-called *load cell configuration*, which is the one shown in panel (b) of Figure 1, the tethers are attached to two independent load cells placed in the rear part of the GCU. Therefore, it allows to get the instantaneous values of the two tether tensions but the length L_T is fixed.

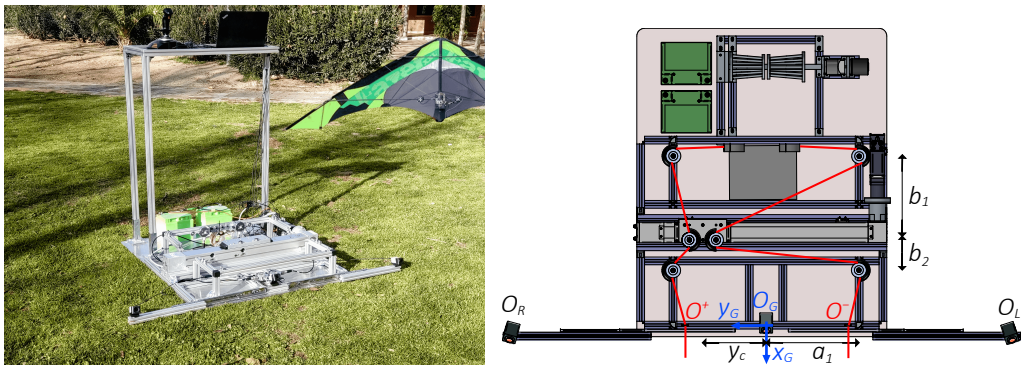

(a) (b)

Figure 1: Panel (a) shows the GCU and the RFD kite of the testbed. Panel (b) displays a sketch of the GCU, the pulleys, and the two tethers in the *load cell configuration*. The ground reference frame (subscript G), the tethers exit points (O^+ and O^-) and the origins of the left (subscript L) and right (subscript R) cameras are shown.

2.2. Actuators and control inputs of the testbed

A commercial linear actuator (*HepcoMotion* SBD2080) based on a pulley-belt system converts the rotational motion of a brushless compact motor (Maxon IDX56L ENC P CO 24V) into a linear lateral motion of the carriage. It is controlled via an USB connected to the laptop of the GCU, where all the electronics are centralized. A gearbox with a reduction ratio of 28:1 to meet a maximum carriage linear speed of 1 m/s and a maximum longitudinal force of 1000 N is placed between the motor and the actuator. Thanks to the proposed configuration of the pulleys shown in Figure 1, the tether tensions are applied in opposite directions on the carriage, thus enhancing the capabilities of the actuator. Regarding the winch actuator, an aluminum flywheel was designed and coupled to an MBoards brushless motor (MBoards 6374 180 kV). A gearbox with a reduction ratio of 10:1 was also necessary to withstand a high torque. The motor control is achieved with an MBoards electronic speed controller (BLDC ESC V4) connected to an Arduino microcontroller to transform the pilot's commands into Pulse Position Modulation signals.

The motors of the linear actuator and the winch are powered by two batteries (12V) connected in series and they are commanded by a pilot through a joystick connected to the laptop. Table 1 shows the main characteristics of the two motorized actuators and the main dimensions of the testbed.

The control variables of the GCU are the lateral motion of the carriage, characterized by its coordinate y_c in the *ground frame* shown in panel (b) of Figure 1, and the number of turns n_W of the tethers around the winch. Using superscripts + and − to denote the tethers leaving the GCU with a positive and negative y_G-coordinate, the tether lengths between the exit point $O^{\pm}$ in Figure 1 and the kite are given by

$$L^{\pm}(n_W, y_c) = L_T - C_1 - 2\pi n_W R_W - \ell^{\pm}(y_c) \tag{1}$$

where C_1 is a geometrical constant that is irrelevant for our analysis, R_W is the mean radius of the winch, and

$$\ell^{\pm}(y_c) = \sqrt{(a_1 \mp y_c)^2 + b_1^2} + \sqrt{(a_1 \mp y_c)^2 + b_2^2}, \tag{2}$$

with a_1, b_1 and b_2 some design parameters shown in Figure 1b. For $|y_c| << a_1$, the difference between the tether lengths outside the GCU reads

$$\Delta L(t) \equiv L^+ - L^- \approx 2a_1 \left(\frac{1}{\sqrt{a_1^2 + b_1^2}} + \frac{1}{\sqrt{a_1^2 + b_2^2}} \right) y_c(t) \tag{3}$$

and it grows linearly with the displacement of the carriage. As shown in Section 4, such a map between the control input ($y_c(t)$) and the real variable affecting the kite dynamics ($\Delta L(t)$), was appropriate to steer the kite with enough authority during the flight campaign.

Table 1: Characteristics of the testbed.

Elements	**Specification**	**Value**
Linear actuator	Maximum force	1000 N
	Maximum speed	1 m/s
	Nominal stroke	0.5 m
	Pulley radius	2.4 cm
Motor of the Actuator	Nominal voltage	24V
	Maximum speed	3090 rpm
	Maximum torque	1.59 Nm
	Gearbox ratio	28:1
Pulleys arrangement	a_1	0.40 m
	b_1	0.30 m
	b_2	0.15 m
Winch	Mean radius	3.5 cm
Motor of the winch	Maximum power	3250 W
	Nominal speed	4320 rpm
	Gearbox ratio	10:1

2.3. Onground and onboard sensors

The testbed has onground and onboard sensors to collect the experimental data about the state of the actuators and the kite during the tests. Figure 2 summarizes them in a block diagram and shows their connections. An absolute encoder embedded in the maxon motor-controller provides the control variable y_c. The control variable n_W is directly related to the rotation angle of the winch, which is measured through the motor hall sensors with a resolution of 60° (equivalent to 3.7 cm of tether length). The tether tensions are measured with two load cells and a data acquisition system by National Instruments™ (find details in Refs. Borobia *et al.* (2018); Borobia-Moreno *et al.* (2021)). The wind velocity vector at the GCU was measured with an ultrasonic wind station. It has an accuracy of 0.1 m/s for the wind velocity and 1° for its azimuth angle.

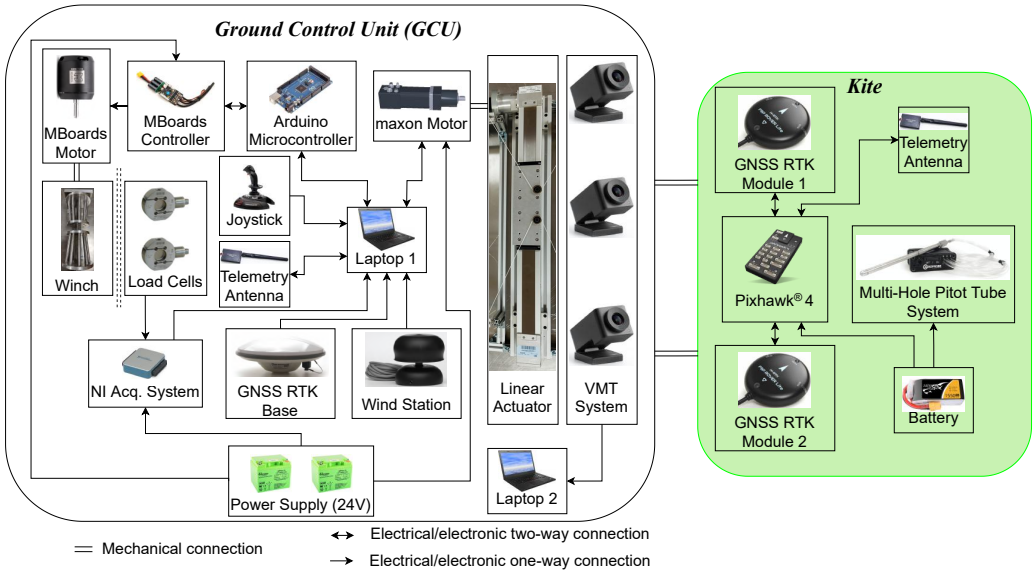

Figure 2: Testbed block diagram.

The testbed was also equipped with three identical cameras in the front part of the GCU. They have a rate of 30 frames per second and wide-angle lenses (120º horizontally and 90º vertically). For later use, we introduce three reference frames S_i, with $i = L, C, R$, attached to the left, center and right cameras (see Figure 1b, where the origins of frames S_L and S_R are shown). The origin of frame S_i, called O_i, coincide with the center of the camera lens, the x_i-axis is perpendicular to the lens and points towards the kite, the z_i-axis is contained in the symmetry plane of the camera and points downward, and the y_i-axis completes a right-handed frame. Vector components in the S_G and S_i frames are related by rotation matrix

$$\begin{pmatrix} \boldsymbol{i}_G \\ \boldsymbol{j}_G \\ \boldsymbol{k}_G \end{pmatrix} = \bar{\boldsymbol{R}}_{Gi}(\chi_i, \lambda_i, \mu_i) \begin{pmatrix} \boldsymbol{i}_i \\ \boldsymbol{j}_i \\ \boldsymbol{k}_i \end{pmatrix}, \tag{4}$$

$$\bar{\boldsymbol{R}}_{Gi}(\chi_i, \lambda_i, \mu_i) \equiv \begin{pmatrix} \mathrm{c}\lambda_i\mathrm{c}\chi_i & \mathrm{s}\mu_i\mathrm{s}\lambda_i\mathrm{c}\chi_i - \mathrm{c}\mu_i\mathrm{s}\chi_i & \mathrm{c}\mu_i\mathrm{s}\lambda_i\mathrm{c}\chi_i + \mathrm{s}\mu_i\mathrm{s}\chi_i \\ \mathrm{c}\lambda_i\mathrm{s}\chi_i & \mathrm{s}\mu_i\mathrm{s}\lambda_i\mathrm{s}\chi_i + \mathrm{c}\mu_i\mathrm{c}\chi_i & \mathrm{c}\mu_i\mathrm{s}\lambda_i\mathrm{s}\chi_i - \mathrm{s}\mu_i\mathrm{c}\chi_i \\ -\mathrm{s}\lambda_i & \mathrm{s}\mu_i\mathrm{c}\lambda_i & \mathrm{c}\mu_i\mathrm{c}\lambda_i \end{pmatrix},$$

where sa and ca stand for sine and cosine of a generic angle a. Table 2 shows the position vector $\overline{O_G O_i}$ and summarizes the nominal values of the rotation angles in Equation (4). We added a subscript 0 to denote that these values are uncalibrated (find more details in Section 3.2).

Table 2: Position vectors and rotation angles of the cameras local frames with respect to ground frame.

	$\chi_{i,0}$ (deg)	$\lambda_{i,0}$ (deg)	$\mu_{i,0}$ (deg)	$\overline{O_G O_i}$ (m)
Left Camera	-17	34	0	$-\boldsymbol{j}_G + 0.14\boldsymbol{k}_G$
Center Camera	0	34	0	$\boldsymbol{0}$
Right Camera	17	34	0	$\boldsymbol{j}_G + 0.14\boldsymbol{k}_G$

An important upgrade of the testbed as compared with previous works (Borobia *et al.* 2018; Borobia-Moreno *et al.* 2021), is the set of sensors onboard the kite. Two GNSS RTK modules and the onboard telemetry antenna were attached to the kite structure by using 3D printed interfaces near the center of mass. They are connected to a Pixhawk®4 microcontroller (onboard computer) which also provides inertial measurements from an embedded IMU and magnetic measurements. The measurements coming from the GNSS, IMU and magnetometer are fused in a built-in Kalman filter and the onboard data is sent to the GCU by telemetry. All the onboard instruments are powered by a small 7.4V LiPo battery whose voltage is converted into 5 V. Since this study is not focused on the kite aerodynamic, the multi-hole pitot tube and its air data computer were not onboard during the flight campaign.

Laptop 1 in Figure 2 reads and saves the control variables, outputs from load cells and the wind station, and onboard data coming from telemetry via USB. The GNSS RTK base is also connected to the laptop to exchange information with the GNSS receivers onboard the kite through the ground telemetry antenna. A separate laptop (laptop 2 in Figure 2) was used to save the video of the three cameras.

3. Visual motion tracking

Figure 3 shows a flow chart of the VMT algorithm employed to estimate the kite position and course angle from the video of a generic camera i. For a given frame, we first identify the pixel $\boldsymbol{P}_i$ with the center of the kite and its polar coordinates $[\delta_i, \ell_i]$. This task is done through a MATLAB-based YOLOv2 artificial neural network (Redmon *et al.* 2016; Redmon & Farhadi 2017). The second step is the computation of the kite position vector with respect to the ground frame $\boldsymbol{r}_k^i$, and the course angle of the kite γ^i. This two-step

procedure is performed for every frame and for each camera. Each step also has its own calibration, which is explained in Appendix A. We remark that the goal of the three cameras in our testbed is not to provide stereo vision through triangulation because the distances between them is too low (≈ 1 m). Their main goal is to upgrade the testbed with sensors to provide redundant measurements of the kite position vector and course angle that could act in a safe mode in case the GNSS would fail.

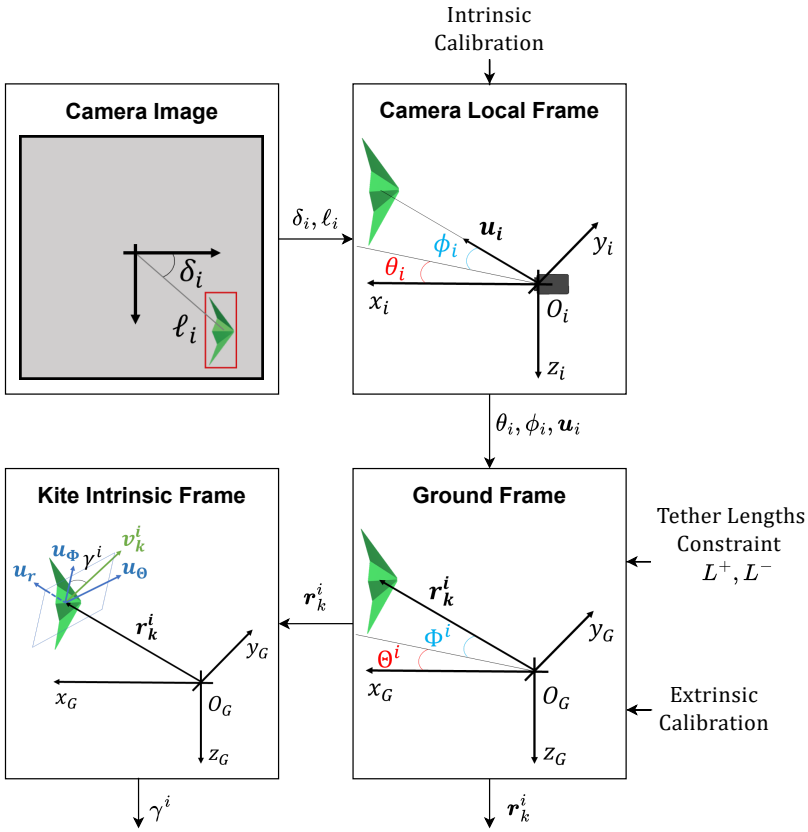

Figure 3: Frames of reference and input/output variables used in the detection (top panels) and the reconstruction (bottom panels) phases.

3.1. Kite detection through artificial neural network YOLOv2

A YOLOv2 algorithm was trained with videos from previous flight test campaigns with the same RFD kite. Such a training phase consists on manually marking with a box the position of the kite for several frames until the algorithm learned to distinguish the kite from the background. Once it was trained, the algorithm is able to autonomously identify the kite with a box and get the pixel at its center together with its polar coordinates $[\delta_i, \ell_i]$ inside the frame.

However, it was found that important distortions were introduced by the lenses and the quality of the measurement can be improved significantly by implementing an intrinsic calibration process (find details in Appendix A). The calibration process not only corrects the polar coordinates of the kite in the image, but also maps them with the spherical angles θ_i and ϕ_i shown in Figure 3. These two angles and the S_i-components of the unit vector

$$\boldsymbol{u}_i \equiv \frac{\overline{O_iO_B}}{|\overline{O_iO_B}|} = \cos\phi_i \cos\theta_i \boldsymbol{i}_i + \cos\phi_i \sin\theta_i \boldsymbol{j}_i - \sin\phi_i \boldsymbol{k}_i, \quad i = L, C, R, \tag{5}$$

are the main output of the detection phase.

In terms of computational cost, the detection part is the most time-consuming task of the VMT algorithm due to the processing of the images by the neural network. Real-time capabilities strongly depend on the graphical processing unit (GPU) of the computer. In this work, the VMT was implemented offline and after the testing campaign was finished. We used a Turing-architecture NVIDIA® mobile GPU that needs around 0.02 s to process one frame. This figure is very close to the time between recorded frames (1/30 s $\approx$ 0.03 s). Therefore, a more powerful GPU or several GPUs would be needed to reach real-time capabilities for the three cameras.

3.2. Reconstruction of the kite position and course angle

The S_G-components of the position vector of the kite estimated by camera i is given by

$$\boldsymbol{r}_k^i = \overline{O_GO_i} + \overline{O_iO_B} = \overline{O_GO_i} + L_i \overline{\boldsymbol{R}}_{Gi}(\chi_i, \lambda_i, \mu_i)\boldsymbol{u}_i, \tag{6}$$

where the S_G-components of the first vector on the right-hand side are in Table 2 and the S_i-components of vector $\boldsymbol{u}_i$ are given by Equation (5). Due to the given difficulties of configuring the testbed with the exact values of the angles shown in Table 2, the angles appearing in the rotation matrix $\overline{\boldsymbol{R}}_{Gi}$ of Equation (5) were found by implementing a self-calibration procedure that is described in Appendix A. Such a procedure, which is iterative and uses the values of Table 2 as initial guess, uses a sample of the onboard data as a reference to calibrate the camera outputs. The calibrated angles just need to be found once and are kept fixed for the whole flight test.

Instead of using the information of the three cameras and triangulation, we propose to compute the module of vector $\overline{O_iO_B}$, i.e., L_i in Equation (6), by solving the nonlinear constraint

$$F(L_i) = |\boldsymbol{r}_k^i| - \frac{L^+ + L^-}{2} = 0. \tag{7}$$

Although this equation ignores the tether sagging, neglects the distance between the exit points $O^{\pm}$ and the cameras, and uses an average value for the tether length outside the GCU, it gives a good approximation for L_i in our testbed (find quantitative results in Section 4).

For later use, we also compute now from $\boldsymbol{r}_k^i$ some interesting quantities that are useful to discuss the experimental results. For instance, the spherical angles are

$$\Theta^i = \arctan\frac{\boldsymbol{r}_k^i \cdot \boldsymbol{j}_G}{\boldsymbol{r}_k^i \cdot \boldsymbol{i}_G}, \qquad \Phi^i = -\arcsin\frac{\boldsymbol{r}_k^i \cdot \boldsymbol{k}_G}{|\boldsymbol{r}_k^i|}. \tag{8}$$

and the unit vectors of the spherical coordinates system shown in Figure 3 read

$$\boldsymbol{u}_r^i = \frac{\boldsymbol{r}_k^i}{|\boldsymbol{r}_k^i|}, \quad \boldsymbol{u}_\Theta^i = -\sin\Theta^i \boldsymbol{i}_G + \cos\Theta^i \boldsymbol{j}_G, \quad \boldsymbol{u}_\Phi^i = \boldsymbol{u}_\Theta \times \boldsymbol{u}_r. \tag{9}$$

The absolute velocity of the kite can also be estimated by using finite differences

$$\boldsymbol{v}_k^i(t) = \frac{\boldsymbol{r}_k^i(t) - \boldsymbol{r}_k^i(t-\Delta t)}{\Delta t}, \tag{10}$$

where $\boldsymbol{r}_k^i(t)$ and $\boldsymbol{r}_k^i(t-\Delta t)$ are the position vector of the kite at time t and $t-\Delta t$ and Δt is the time between frames. The course angle γ^i, which typically plays a very important role in the control of AWE systems, is

$$\gamma^i = \arctan \frac{\boldsymbol{v}_k^i \cdot \boldsymbol{u}_\Theta^i}{\boldsymbol{v}_k^i \cdot \boldsymbol{u}_\Phi^i}. \tag{11}$$

4. Results

4.1. Open-loop control

The flight testing campaign showed that the automatic control system presented in Section 2.2 allows a pilot to control the kite remotely from the ground station without practically any additional external aid and for all the phases of the flight. The only exception is the take-off, where a vertical impulse provided by an assistant is needed to initiate the flight in the power zone of the wind window. A smooth landing was achieved by just steering the kite to make it descend slowly and with its nose up. The results of this section were extracted from a flight of 5 minutes of duration that is available in (Universidad Carlos III de Madrid 2022). This section mainly focuses on the first 15 seconds of the flight. Panel (a) of Figure 4 shows the kite trajectory estimated by the onboard computer in the $\Theta - \Phi$ plane.

After the take-off, the pilot used the automatic control system to steer and fly the kite in crosswind conditions during the 5 minutes. Panel (b) in Figure 4 displays the kite course angle γ estimated with onboard data by using Equation 11 and the lateral control input y_c. The maxima and minima values of the course angle have been labeled with numbers in the three panels of the figure and the kite flight direction is indicated with arrows in panel (a). There is a clear correlation between the actuation (y_c) and the course angle of the kite, which is commonly considered the target variable in the closed-loop control of AWE Systems (Fagiano *et al.* 2014*b*; Wood *et al.* 2015; Vermillion *et al.* 2021).

A lateral displacement to the right of the linear actuator (positive y_c) induces turns toward the left of the kite, i.e., transitions of the course angle from positive to negative values. Some examples of these transitions are the turns happening immediately after an odd number in Fig, 4. All the turns changing the course angle from negative to positive values are induced by a left motion of the linear actuator (negative y_c values) (turns after an even number). This repeatability between turns and control input happened during the full flight.

In the case of soft kites, a correlation between the derivative of the course angle $\dot{\gamma}$ and the steering input ΔL (Equation 3) was found (Fagiano *et al.* 2014*b*; Wood *et al.* 2015). In particular, the following relation between both variables was proposed in the kite turning (Wood *et al.* 2015)

$$\dot{\gamma}(t) = K_L \Delta L(t - t_d), \tag{12}$$

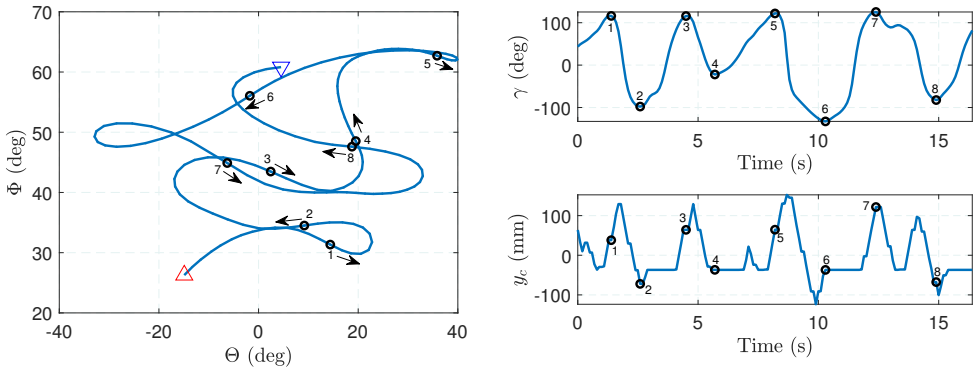

(a) (b)

Figure 4: Panel (a) and (b) show the kite trajectory in the $\Theta - \Phi$ plane, and the evolution of the course angle γ and the lateral position of the linear actuator y_c. The red upward (blue downward) triangle corresponds to the start (end) of the trajectory. The arrows in panel (a) indicate the direction of the flight.

with K_L a gain and $\Delta L(t - t_d)$ the steering input delayed t_d seconds. The validity of such a relation for our automatic control system and the RFD kite was investigated by finding the best correlation between $\dot{\gamma}(t)$ and $\Delta L(t - t_d)$ as t_d was varied. Figure 5 shows such a correlation without delay ($t_d = 0$ s), with the delay corresponding to minimum error of a least-squares linear approximation ($t_d = 0.2$ s), and the least-squares linear approximation for a period of 150 s within the five-minute flight. The experimental data followed Equation (12) but the dispersion for both sets ($t_d = 0$ s and $t_d = 0.2$ s) is slightly higher than in Refs. (Wood *et al.* 2015; Fagiano *et al.* 2014*b*). We highlight that the data in Figure 5 was not filtered for small azimuth angles Θ and the kite did not always followed crosswind figures of eight.

The steering delay ($t_d = 0.2$ s) that minimizes the error of the least-squares fit is smaller than the 0.66 s found in Wood *et al.* (2015) for soft kites. This characterizes the fast turning response of the RFD kite. Another important figure is the slope of the least-squares fit that gives to us the gain $K_L = -8.4$ rad/(ms). Such a value is close to the one found in Wood *et al.* (2015) (-10 rad/(ms)). The steering gain, which is a characteristic of our RFD kite and automatic control system, can be used for future closed-loop control design purposes. Equation 3 shall be used to find the gain of a homologous correlation between $\dot{\gamma}(t)$ and $y_c(t - t_d)$.

As shown in Figure 6, a slightly better correlation (smaller error in the least-squares fit) is found for $\dot{\gamma}(t)$ and the delayed difference in tether tensions (right minus left) $\Delta T(t - t_d)$ measured by the load cells. We propose the law

$$\dot{\gamma}(t) = K_T \Delta T(t - t_d), \tag{13}$$

where K_T is a constant gain. The slope of the least-squares fit in Figure 6 is $K_T = 0.02$ rad/(Ns) which, unlike K_L, is positive because a positive ΔT causes the kite to turn

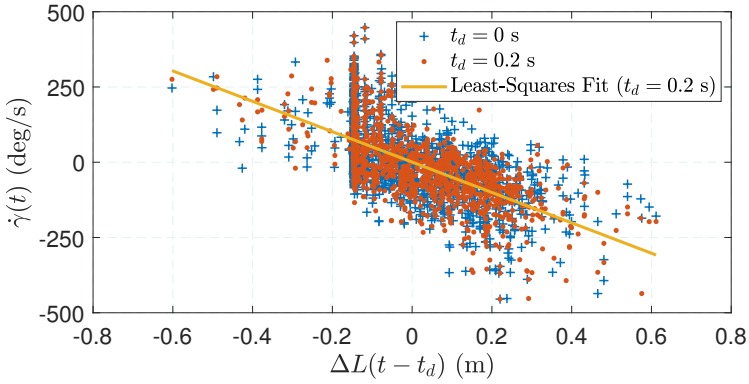

Figure 5: Correlation between time derivative of the course angle estimated with onboard data and delayed (t_d seconds) steering input ΔL.

right, i.e., $\dot{\gamma} > 0$. The smaller dispersion found for this pair of data may be a consequence of the direct impact of the differential tension on the kite turns.

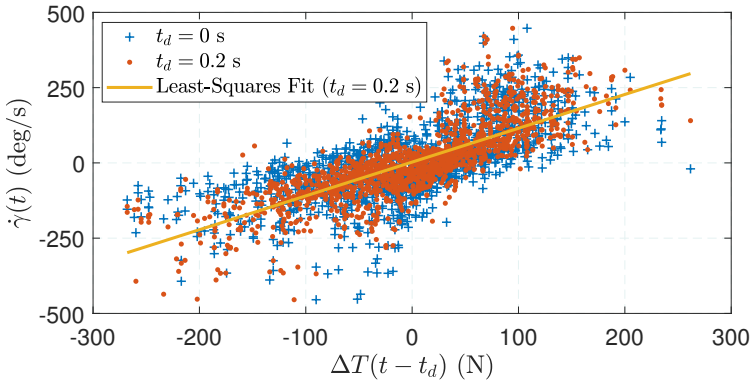

Figure 6: Correlation between time derivative of the course angle estimated with onboard data and delayed (t_d seconds) tether tensions difference (right minus left) ΔT.

4.2. Comparison of VMT system and onboard data

Figure 7 shows the evolution of the spherical coordinates Θ and Φ of the kite computed with the onboard data and independently estimated with the three cameras by using Equation 8. The maneuver analysed is the one shown in Figure 4 with a duration of 23 seconds. The 3 curves obtained from the images of the three cameras present a remarkable similarity among them. The latter and the fact that the cameras had different positions and rotation angles with respect to frame G, i.e., different extrinsic calibration settings, makes the cameras a reliable source of measurements. The trajectory estimated by the onboard

computer generally matches the one by the 3 cameras but there are some differences at some of the turns, i.e., maxima and minima of the azimuth angle Θ. The analysis of the data after the test campaign revealed that these discrepancies may be attributed to a lack of precision of the GNSS and not to the VMT. It was found that the configuration of the GNSS was not optimal because it was prepared for low acceleration (less than 1g) maneuvers whereas the experimental data revealed that it was larger than 1g most of the time. The filter was also configured to use the measurement of the altitude from the barometer instead of the GNSS. These results suggest that future tests can reach higher position accuracy by using a different configuration of the GNSS and the filter and highlight the importance of having redundant and independent measurements, like the one provided by the VMT system.

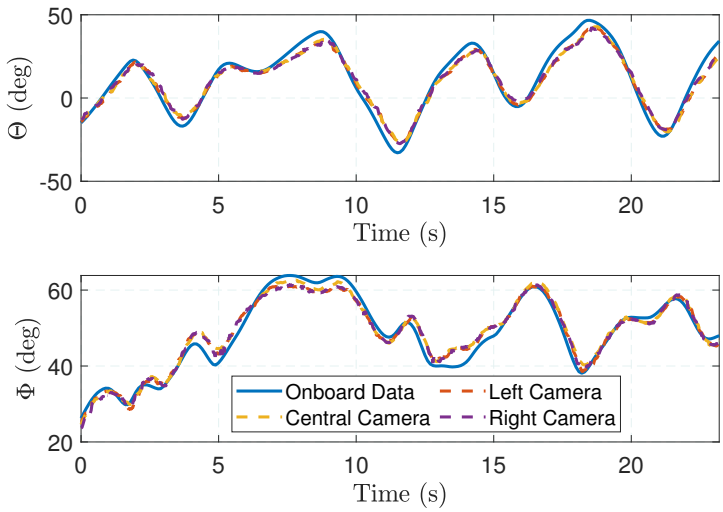

Figure 7: Evolution of the kite position in spherical coordinates Θ and Φ estimated by the onboard computer and the three cameras.

Another important byproduct of the VMT system is the estimation of the kite course angle by using Equation (11). Figure 8 shows the estimation of the course angle with the onboard data and with the central camera for the same flight of Figure 7. For clarity, the course angles given by the left and right cameras are not shown because they practically coincide with the one of the central camera. It is evident from the figure that the raw estimation of the course angle (solid black line) is noisy and cannot be used directly. However, after filtering the data by using a moving-averages filter with a window size of 10 samples, the average course angle is well-captured (solid yellow line) because it exhibits a very good agreement with the values provided by the onboard data (dashed line).

The filtered course angle information obtained with the three-camera system could also be included as one more observation variable inside the observation model of a Kalman filter. This information can be related to the kite attitude (heading angle) in crosswind conditions if the sideslip angle is small (Fagiano *et al.* 2014*b*). Therefore, in the situation

of lack of onboard data, useful attitude information can be extracted from the estimated values of γ obtained from the VMT system.

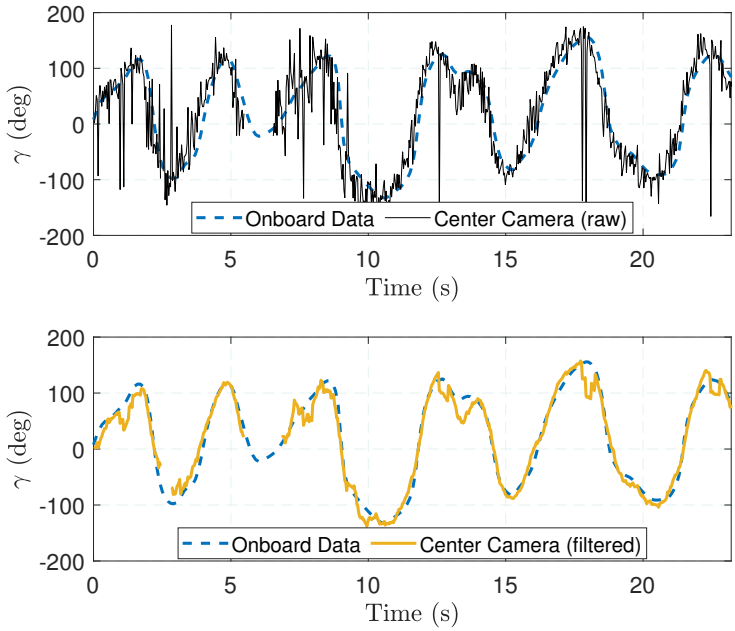

Figure 8: Evolution of the kite course angle γ estimated by the onboard computer and the central camera (raw and filtered measurements).

Another important characteristic of any VTM system is its robustness. In our case, the neural network YOLOv2 was not able to detect the kite for certain frames. Consequently, the kite position and course angle of the kite provided by the cameras in Figures 7 and 8 have some gaps. However, the percentage of non-detection is small (camera 1: 2.5%; camera 2: 4.9%; camera 3: 3.4%) and the coincidence of simultaneous non-detection by the three cameras was below 0.1% for the five-minute flight. This result indicates the robustness of the VMT system based on three independent cameras.

5. Conclusions

The updates implemented in this work improved the UC3M testbed and can open new possibilities in the aerodynamic, dynamic and control characterization of two-line AWE kites. These updates include a precise GNSS RTK modules, an ultrasonic wind station, a telemetry link between the sensors onboard the kite and the ground station, a VMT system, and a ground-based automatic control system with a linear actuator and a winch that substituted the former manual control. As shown by the flight testing campaign, they enlarged the amount, variety, and quality of the experimental data. The five-minute duration test presented in this work showed that the automatic control system has enough authority to steer the kite and perform figure-of-eight maneuvers and complete the landing

of the kite with the commands provided by the pilot. The take-off needs an assistant to provide a vertical impulse to the kite.

The experimental work allowed to correlate the time derivative of the course angle $\dot{\gamma}(t)$ of an RFD kite flying in crosswind conditions and the steering input of the ground station of the testbed $\Delta L(t)$. Aligned with previous works for soft kites, it was found that the relation between $\dot{\gamma}(t)$ and $\Delta L(t - t_d)$ is linear, where t_d is a constant delay time. Experimental values for the gain and t_d were found. Interestingly, the analysis of the correlation of $\dot{\gamma}(t)$ and the delayed differential tether tension $\Delta T(t - t_d)$, which is directly measured by the load cells of the testbed, exhibited an even lower dispersion. This result suggests that, to close the control loop and reach autonomous flight in future works, it can be advantageous to use $\Delta T(t - t_d)$ instead of $\Delta L(t - t_d)$ or at least introduce information about $\Delta T(t - t_d)$ in the control law.

The experimental campaign also showed that the novel VMT system based on three cameras and a neural network (YOLOv2 algorithm) of the updated testbed can be used to obtain reliable estimations of the kite position and course angle. After intrinsic and extrinsic calibrations, it was found that the outputs of the VMT system based on each of the cameras exhibit a good agreement among them and with the independent measurements of the onboard sensors. An important conclusion is that the YOLOv2 algorithm failed in the detection of the kite within around 5% of the frames. However, the simultaneous non-detection from the frames of the three cameras was below 0.1% for the five-minute flight. Therefore, the redundant three-camera system seems to be robust and can be used as an additional observation in the Kalman filter or as a backup system in case of loss of telemetry or GNSS signal. Future work may also explore the use of the three cameras as a stereo vision system by increasing the distance among them.

Acknowledgements

This work was carried out under the framework of the GreenKite-2 project (PID2019-110146RB-I00) funded by MCIN/AEI/10.13039/501100011033. The authors thank A. Bujarrabal from *CT Engineering Group* for the fruitful discussions and support to develop this work.

Appendix A. Intrinsic and extrinsic calibration of the cameras

A.1. Intrinsic calibration

The intrinsic calibration process allows to determine the angles θ and ϕ in Equation (5) from the image of a camera (for simplicity we remove here the subscript i). Therefore, it involves the construction of the map $(\delta_E, \ell_E) \to (\theta, \phi)$, where δ_E and ℓ_E are the polar coordinates of a given pixel in the image and θ and ϕ their real spherical angles for a system centered at the camera. In order to construct such a map, an intrinsic calibration of the cameras was performed to remove the distortions induced by the lenses (Kannala & Brandt 2006). To do the calibration, a spherical pattern with radius $\rho_K = 10.4$ cm was 3D printed to generate a set of grid points with known spherical angles δ_K and β_K and a photo was taken with a camera placed at its center. These two angles, which are shown in Figure 9a, are equivalent to the final outputs of the calibration process (θ and ϕ) because the unit vector in Equation (5) reads

$$\begin{aligned} \boldsymbol{u}_i &= \cos\phi\cos\theta\boldsymbol{i}_i + \cos\phi\sin\theta\boldsymbol{j}_i - \sin\phi\boldsymbol{k}_i \\ &= \cos\beta\boldsymbol{i}_i + \sin\beta\cos\delta\boldsymbol{j}_i + \sin\beta\sin\delta\boldsymbol{k}_i, \end{aligned} \tag{14}$$

and we have

$$\theta = \arctan\left(\tan\beta\cos\delta\right), \quad \phi = \arcsin\left(-\sin\beta\sin\delta\right). \tag{15}$$

To illustrate the calibration process, we show in the panel (a) of Figure 9 a sketch of the spherical pattern, some characteristic lines, and the corresponding image obtained with the camera.

The analysis of the image revealed that lines in the spherical pattern with constant δ_K appears in the image as straight lines with constant δ_E. Therefore, we conclude that the azimuth angle is not affected by the distortion and we can set $\delta = \delta_E$. On the other hand, a circle in the spherical pattern with a constant β_K appears in the image as a circle with radius ℓ_E. Due to the distortion of the camera, ℓ_E does not coincide with the expected radius that reads (Kannala & Brandt 2006)

$$\ell_K = f\tan\beta_K, \tag{16}$$

where $f = 360$ pixels is the focal distance of the camera. Panel (b) in Figure 9 shows the expected radius ℓ_K given in Equation (16) and the one measured in the image ℓ_E for circle in the pattern with different β_k. Therefore, we set in the calibration the relation $\beta = \beta_K(\ell_E)$ shown in panel (b). Since we have such a relation for discrete values of β_K, we used a linear interpolation in the analysis of the images.

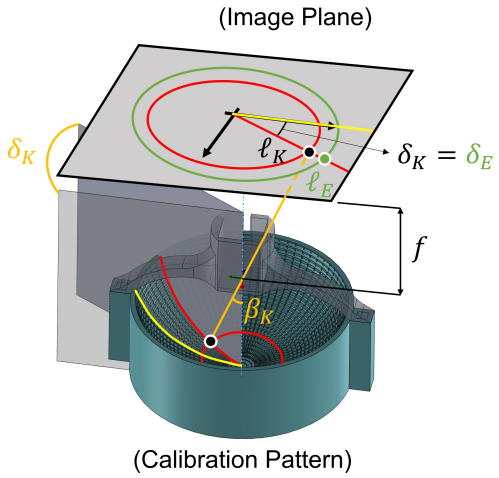

(a)

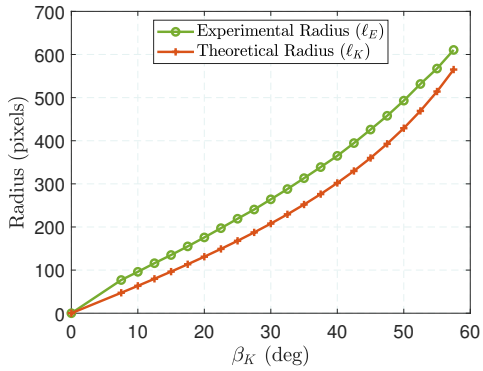

(b)

Figure 9: Panel (a) shows a sketch of the experimental setup for the intrinsic calibration. Panel (b) displays the theoretical and experimental radius of circles of different β_K.

A.2. Extrinsic calibration

The accuracy of the position vectors of the cameras with respect to S_G given in Table 2 is high. The relevant distances can be directly measured in the laboratory and the brackets of the cameras are bolted on the structure of the GCU. Therefore, they are kept fixed reliably during the flight testing. However, ensuring that the orientations of the frames S_i with respect to S_G coincide with the ones given by the nominal values of the angles

shown in Table 2 is more difficult. For this reason, an extrinsic calibration procedure is necessary to correct possible mismatches of the three rotation angles χ_i, λ_i, μ_i for each camera independently.

The proposed calibration is based on minimizing the euclidean distances in the Θ-Φ plane between the position of the kite found by the VMT system and the one estimated by the onboard computer for a subset of $N_t = 700$ camera frames (~ 23 s). In particular, we solved the optimization problem

$$\begin{aligned} \boldsymbol{X}^* &= \arg\left(\min_{\boldsymbol{X}} F(\boldsymbol{X})\right), \\ \text{subject to:} \quad & \boldsymbol{lb} \leq \boldsymbol{X} \leq \boldsymbol{ub}, \end{aligned} \tag{17}$$

where $\boldsymbol{X} = [\chi_i, \lambda_i, \mu_i]$ contains the optimization variables, superscript * stands for optimal variables, $\boldsymbol{lb}$ and $\boldsymbol{ub}$ are the lower and upper bounds of $\boldsymbol{X}$, which were taken as $-90° \leq \chi_i \leq 90°$, $0° \leq \lambda_i \leq 90°$, and $-90° \leq \mu_i \leq 90°$. The objective function F is defined as

$$F(\boldsymbol{X}) \equiv \sum_{j=1}^{N_t} \sqrt{\left[\Theta^i(j\Delta t, \boldsymbol{X}) - \Theta^{\mathrm{OB}}(j\Delta t)\right]^2 + \left[\Phi^i(j\Delta t, \boldsymbol{X}) - \Phi^{\mathrm{OB}}(j\Delta t)\right]^2}, \tag{18}$$

with superscript OB standing for onboard data.

The optimization problem was solved with a standard gradient-based solver and using the angles of Table 2 as initial guesses. Table 3 shows the optimal values for the three angles and, as expected, they are close to the nominal ones (see Table 2).

Table 3: Calibrated rotation angles of the cameras.

	χ_i (deg)	λ_i (deg)	μ_i (deg)
Left Camera	-15.9	48.1	5.0
Center Camera	1.3	33.4	2.9
Right Camera	17.4	39.6	4.1

References

Borobia, R., Sánchez-Arriaga, G., Serino, A. & Schmehl, R. 2018 Flight-Path Reconstruction and Flight Test of Four-Line Power Kites. *J. Guid. Control. Dyn.* **41** (12), 2604–2614.

Borobia-Moreno, R., Ramiro-Rebollo, D., Schmehl, R. & Sánchez-Arriaga, G. 2021 Identification of kite aerodynamic characteristics using the estimation before modeling technique. *Wind Energy* **24** (6), 596–608.

Castro-Fernández, I., Borobia-Moreno, R., Cavallaro, R. & Sánchez-Arriaga, G. 2021 Three-Dimensional Unsteady Aerodynamic Analysis of a Rigid-Framed Delta Kite Applied to Airborne Wind Energy. *Energies* **14** (23), 8080.

Cherubini, A., Papini, A., Vertechy, R. & Fontana, M. 2015 Airborne Wind Energy Systems: A review of the technologies. *Renew. Sustain. Energy Rev.* **51**, 1461–1476.

Coleman, J., Ahmad, H. & Toal, D. 2017 Development and Testing of a Control System for the Automatic Flight of Tethered Parafoils. *J. F. Robot.* **34** (3), 519–538.

Costello, S., Francois, G. & Bonvin, D. 2018 Real-Time Optimizing Control of an Experimental Crosswind Power Kite. *IEEE Trans. Control Syst. Technol.* **26** (2), 507–522.

Deodhar, N., Bafandeh, A., Deese, J., Smith, B., Muyimbwa, T., Vermillion, C. & Tkacik, P. 2017 Laboratory-Scale flight characterization of a multitethered aerostat for wind energy generation. *AIAA J.* **55** (6), 1823–1832.

Ecorys 2018 Study on Challenges in the commercialisation of airborne wind energy systems. *Tech. Rep.*. European Commission.

Erhard, M. & Strauch, H. 2015 Flight control of tethered kites in autonomous pumping cycles for airborne wind energy. *Control Eng. Pract.* **40**, 13–26.

Fagiano, L., Huynh, K., Bamieh, B. & Khammash, M. 2014*a* On Sensor Fusion for Airborne Wind Energy Systems. *IEEE Trans. Control Syst. Technol.* **22** (3), 930–943.

Fagiano, L. & Marks, T. 2015 Design of a small-scale prototype for research in airborne wind energy. *IEEE/ASME Trans. Mechatronics* **20** (1), 166–177.

Fagiano, L., Nguyen-Van, E., Rager, F., Schnez, S. & Ohler, C. 2017*a* A Small-Scale Prototype to Study the Takeoff of Tethered Rigid Aircrafts for Airborne Wind Energy. *IEEE/ASME Trans. Mechatronics* **22** (4), 1869–1880.

Fagiano, L., Nguyen-Van, E., Rager, F., Schnez, S. & Ohler, C. 2017*b* Automatic Take-Off of a Tethered Aircraft for Airborne Wind Energy: Control Design and Experimental Results. *IFAC-PapersOnLine* **50** (1), 11932–11937.

Fagiano, L., Nguyen-Van, E., Rager, F., Schnez, S. & Ohler, C. 2018 Autonomous Takeoff and Flight of a Tethered Aircraft for Airborne Wind Energy. *IEEE Trans. Control Syst. Technol.* **26** (1), 151–166.

Fagiano, L., Zgraggen, A. U., Morari, M. & Khammash, M. 2014*b* Automatic crosswind flight of tethered wings for airborne wind energy: Modeling, control design, and experimental results. *IEEE Trans. Control Syst. Technol.* **22** (4), 1433–1447.

Geebelen, K., Vukov, M., Wagner, A., Ahmad, H., Zanon, M., Gros, S., Vandepitte, D., Swevers, J. & Diehl, M. 2013 An Experimental Test Setup for Advanced Estimation and Control of an Airborne Wind Energy System. In *Airborne Wind Energy. Ser. Green energy Technol.*, pp. 459–471.

Healy, F., Pontillo, A., Rezgui, D., Cooper, J. E., Kirk, J., Wilson, T. & Castrichini, A. 2022 Experimental Analysis of the Dynamics of Flared Folding Wingtips via a Novel Tethered Flight Test. *AIAA 2022-1757* (January).

Hesse, H., Polzin, M., Wood, T. A. & Smith, R. S. 2018 Visual motion tracking and sensor fusion for kite power systems. In *Airborne Wind Energy. Ser. Green energy Technol.*, , vol. 9789811019, pp. 413–438.

Heudorfer, K. & Dobler, U. 2022 The ICM-autoKite Project: Developing an Automated

Kite Propulsion System for the KITE GAS/FUEL SHIP and Economic Green Hydrogen Production. In *Airborne Wind Energy Conf.*, p. 2022.

Hummel, J., Göhlich, D. & Schmehl, R. 2019 Automatic measurement and characterization of the dynamic properties of tethered membrane wings. *Wind Energy Sci.* **4** (1), 41–55.

Kannala, J. & Brandt, S. S. 2006 A Generic Camera Model and Calibration Method for Conventional, Wide-Angle, and Fish-Eye Lenses. *Pattern Anal. Mach. Intell.* **28** (8), 1–15.

Kitepower 2022 Webpage of Kitepower. [https://thekitepower.com/].

Licitra, G., Bürger, A., Williams, P., Ruiterkamp, R. & Diehl, M. 2019 Aerodynamic model identification of an autonomous aircraft for airborne wind energy. *Optim. Control Appl. Methods* **40** (3), 422–447.

Loyd, M. L. 1980 Crosswind Kite Power. *J. Energy* .

Milanese, M., Taddei, F. & Milanese, S. 2013 Design and Testing of a 60 kW Yo-Yo Airborne Wind Energy Generator. In *Airborne Wind Energy. Ser. Green energy Technol.*.

Millane, A., Hesse, H., Wood, T. A. & Smith, R. S. 2015 Range-inertial estimation for airborne wind energy. *Proc. IEEE Conf. Decis. Control* **54rd IEEE** (Cdc), 455–460.

Oehler, J. & Schmehl, R. 2019 Aerodynamic characterization of a soft kite by in situ flow measurement. *Wind Energy Sci.* **4** (1), 1–21.

Redmon, J., Divvala, S., Girshick, R. & Farhadi, A. 2016 You Only Look Once: Unified, Real-Time Object Detection. *Proc. - 30th IEEE Conf. Comput. Vis. Pattern Recognition, CVPR 2016* .

Redmon, J. & Farhadi, A. 2017 YOLO9000: Better, faster, stronger. *Proc. - 30th IEEE Conf. Comput. Vis. Pattern Recognition, CVPR 2017* **2017-Janua**, 6517–6525.

Rushdi, M. A., Dief, T. N., Yoshida, S. & Schmehl, R. 2020 Towing test data set of the kyushu university kite system. *Data* **5** (3), 1–18.

Salma, V., Friedl, F. & Schmehl, R. 2020 Improving reliability and safety of airborne wind energy systems. *Wind Energy* (April 2019), 340–356.

Schmidt, E., De Lellis Costa De Oliveira, M., Saraiva Da Silva, R., Fagiano, L. & Trofino Neto, A. 2020 In-Flight Estimation of the Aerodynamics of Tethered Wings for Airborne Wind Energy. *IEEE Trans. Control Syst. Technol.* **28** (4), 1309–1322.

Shahzad, A., Gao, X., Yasin, A., Javed, K. & Anwar, S. M. 2020 A vision-based path planning and object tracking framework for 6-DOF robotic manipulator. *IEEE Access* **8**, 203158–203167.

SkySails Power 2022 Webpage of Skysails Power. [https://skysails-power.com/].

Smolyanskiy, N., Kamenev, A. & Birchfield, S. 2018 On the importance of stereo for accurate depth estimation: An efficient semi-supervised deep neural network approach. *IEEE Comput. Soc. Conf. Comput. Vis. Pattern Recognit. Work.* **2018-June**, 1120–1128.

Universidad Carlos III de Madrid 2022 Web page of the UC3M Airborne Wind Energy group. [https://aero.uc3m.es/airborne-wind-energy/].

U.S. Department of Energy 2021 Report to Congress: Challenges and Opportunities for Airborne Wind Energy in the United States. *Tech. Rep.* November. United States Department of Energy, Washington, DC 20585.

Vermillion, C., Cobb, M., Fagiano, L., Leuthold, R., Diehl, M., Smith, R. S., Wood, T. A., Rapp, S., Schmehl, R., Olinger, D. & Demetriou, M. 2021 Electricity in the air: Insights from two decades of advanced control research and experimental flight testing of airborne wind energy systems. *Annu. Rev. Control* **52** (December 2020), 330–357.

van der Vlugt, R., Peschel, J. & Schmehl, R. 2013 Design and Experimental Characterization of a Pumping Kite Power System. In *Airborne Wind Energy. Ser. Green energy Technol.*.

de Wachter, A. 2008 Deformation and Aerodynamic Performance of a Ram-Air Wing. *Tech. Rep.* July. Technical University of Delft.

Watson, S., Moro, A., Reis, V., Baniotopoulos, C., Barth, S., Bartoli, G., Bauer, F., Boelman, E., Bosse, D., Cherubini, A., Croce, A., Fagiano, L., Fontana, M., Gambier, A., Gkoumas, K., Golightly, C., Latour, M. I., Jamieson, P., Kaldellis, J., Macdonald, A., Murphy, J., Muskulus, M., Petrini, F., Pigolotti, L., Rasmussen, F., Schild, P., Schmehl, R., Stavridou, N., Tande, J., Taylor, N., Telsnig, T. & Wiser, R. 2019 Future emerging technologies in the wind power sector: A European perspective. *Renew. Sustain. Energy Rev.* **113** (October), 109270.

Wood, T. A., Hesse, H., Zgraggen, A. U. & Smith, R. S. 2015 Model-based identification and control of the velocity vector orientation for autonomous kites. *Proc. Am. Control Conf.* **2015-July**, 2377–2382.

Chapter 3

Conclusions and future works

3.1. Conclusions

In the context of the emerging airborne wind energy field, aerodynamics plays the two most important roles: maintaining the vehicle airborne and producing power from the wind. The numerical and experimental aerodynamic characterization of AWE aircraft is of major importance for the development of AWE technology. This thesis presents two main contributions: (i) investigating the validity of three computational aerodynamic tools applied to an RFD kite with emphasis on its unsteady characteristics and (ii) developing and testing a small-scale testbed aimed at aerodynamic, dynamic and control characterization of two-tether and three-tether AWE systems.

Regarding the numerical investigation (i), three unsteady aerodynamic tools at different degrees of fidelity and computational cost were compared against one another and flight test data in Papers 1 and 2. The measured kite kinematics was prescribed in the tools and the aerodynamic force and moment coefficients as a function of the angle of attack and sideslip angle were compared. Paper 1 presents the in-house 3D unsteady panel method (UnPaM) and highlights that the potential-flow tool matches the order of magnitude in the lift and lateral force coefficients but greatly underestimates the drag because it does not model viscous effects. Moreover, an analysis on steady, quasi-steady and unsteady effects for the prescribed kinematics revealed that the quasi-steady analysis presents important differences with the steady computations but virtually no difference with the unsteady results allowing for faster simulations. On the other hand, an in-depth analysis of the former experimental data and flow visualization data from a complementary flight test campaign showed clear evidences of dynamic stall phenomenology driven by periodic changes in the angle of attack. For this reason, Paper 2 focuses on the unsteady aerodynamics of the RFD kite under these conditions. It introduces two new unsteady viscous tools: the open-source CFD tool SU2 that solves the unsteady RANS equations and a semi-empirical dynamic stall model that combines UnPaM and high-fidelity CFD data. The benchmark demonstrated that only the viscous models (unsteady RANS and semi-empirical), unlike UnPaM, were able to reproduce dynamic stall. Apart from the typical hysteresis behavior in dynamic stall, a leading-edge vortex that periodically forms and detaches was identified in the CFD results qualitatively matching the experimental observations.

The occurrence of unsteady aerodynamic phenomena during the crosswind flight of the RFD kite was corroborated and quantified in Paper 2. However, strong fluid-structure interaction was observed as a by-product of the flow visualization experiment. This inspired an additional campaign of CFD simulations to quantify the effect of kite deflection (curvature). Interestingly, a 5% deflection considerably shifted up the lift and drag coefficients versus the angle of attack curves suggesting that aerostructural coupling and dynamic stall work collaboratively. This may explain the higher amplitudes of the experimental hysteresis cycles as compared to the numerical ones.

The architecture and a flight test campaign of a small-scale testbed (ii) is presented in Paper 3. As compared to the previous testbed of UC3M, the manual control bar was substituted by an automatic linear actuator and a winch, the wind station and GNSS receiver were upgraded and a novel VMT system was included. The enhancement in hardware and automation opens new possibilities for the aerodynamic, dynamic and control characterization of two-line ground-actuated kites. In fact, a control characterization of the RFD kite was performed by identifying key turning parameters relating the time derivative of the course angle with either the steering input or the differential tether tension. This characterization paved the way toward the design of a closed-loop controller in the near future. Moreover, the estimation capability and robustness of the new VMT system based on three cameras and an artificial neural network were showcased. After an intrinsic and extrinsic calibrations, the outputs by the three cameras resulted in very consistent measurements among them and with independent onboard data almost continuously (99.9% of the time). Consequently, the VMT system proved to be an accurate, robust and independent source of data that can be used as a redundant observation in an estimator or as a backup for the onboard sensors.

3.2. Future works

After gaining a better understanding of unsteady aerodynamics of delta kites, proposing and validating different aerodynamic tools and realizing an experimental testbed aimed at aerodynamic characterization, among others, several lines of future works may depart from this thesis:

- The preliminary quantification of aeroelastic effects performed in Paper 2 opens new research questions such as *what is the relative contribution of aeroelasticity and dynamic stall in the measured hysteresis cycles?* To answer this question, the author proposes to perform a new experimental campaign with the small-scale testbed of Paper 3 or newer versions including the multi-hole pitot tube. The automatic control system may reduce the experimental uncertainties present in previous datasets and open the possibility of acquiring a larger amount of data with higher repeatability. Additionally, a fluid-structure interaction framework coupling the aerodynamic models presented in this thesis and an external finite element structural model should be developed and verified.
- Since the contribution of aeroelastic effects are expected to be high, a reduced-order aeroelastic model to gain computational speed without losing much accuracy would benefit its coupling with a kite flight simulator.
- To validate the aeroelastic computational tools, an experimental aeroelastic characterization should be carried out by equipping the testbed with new sensors such as strain gauges, accelerometers and pressure taps in different positions of the wing.
- Despite the VMT system proved to be an accurate and robust sensor, several enhancements are proposed. The imposed tether length constraint, that led to errors mostly induced by tether sagging, can be replaced by a stereo VMT system composed of at least two cameras sufficiently separated from each other. On the other hand, the extrinsic calibration procedure, that still relies on external (onboard) data, should be executed autonomously by a self-calibrating platform.

Bibliography

Ali, Q. S. & Kim, M. H. 2020 Unsteady aerodynamic performance analysis of an airborne wind turbine under load varying conditions at high altitude. *Energy Convers. Manag.* **210** (December 2019), 1–18.

Archer, C. L. 2013 An Introduction to Meteorology for Airborne Wind Energy. In *Airborne Wind Energy. Ser. Green energy Technol.*, pp. 81 – 94. Springer.

Baayen, J. H. & Ockels, W. J. 2012 Tracking control with adaption of kites. *IET Control Theory Appl.* **6** (2), 182–191.

Baheri, A., Bin-Karim, S., Bafandeh, A. & Vermillion, C. 2017 Real-time control using Bayesian optimization: A case study in airborne wind energy systems. *Control Eng. Pract.* **69** (1437296), 131–140.

Bangga, G., Lutz, T. & Arnold, M. 2020 An improved second-order dynamic stall model for wind turbine airfoils. *Wind Energy Sci.* **5**, 1037–1058.

Bartlett, G. E. & Vidal, R. J. 1955 Experimental Investigation of Influence of Edge Shape on the Aerodynamic Characteristics of Low Aspect Ratio Wings at Low Speeds. *J. aernautical Sci.* **22** (8), 517–533.

Berra, A. & Fagiano, L. 2021 An optimal reeling control strategy for pumping airborne wind energy systems without wind speed feedback. In *2021 Eur. Control Conf. ECC 2021*, pp. 1199–1204. EUCA.

Bórawski, P., Bełdycka-Bórawska, A., Jankowski, K. J., Dubis, B. & Dunn, J. W. 2020 Development of wind energy market in the European Union. *Renew. Energy* **161**, 691–700.

Borobia, R., Sánchez-Arriaga, G., Serino, A. & Schmehl, R. 2018 Flight-Path Reconstruction and Flight Test of Four-Line Power Kites. *J. Guid. Control. Dyn.* **41** (12), 2604–2614.

Borobia-Moreno, R., Ramiro-Rebollo, D., Schmehl, R. & Sánchez-Arriaga, G. 2021 Identification of kite aerodynamic characteristics using the estimation before modeling technique. *Wind Energy* **24** (6), 596–608.

Bosch, A., Schmehl, R., Tiso, P. & Rixen, D. 2014 Dynamic nonlinear aeroelastic model of a kite for power generation. *J. Guid. Control. Dyn.* **37** (5), 1426–1436.

Boutet, J., Dimitriadis, G. & Amandolese, X. 2020 A modified Leishman – Beddoes model for airfoil sections undergoing dynamic stall at low Reynolds numbers. *J. Fluids Struct.* **93**, 102852.

Breukels, J. 2010 An engineering methodology for kite design. PhD thesis, Delft University of Technology.

Breukels, J., Schmehl, R. & Ockels, W. 2013 Aeroelastic Simulation of Flexible Membrane Wings based on Multibody System Dynamics. In *Airborne Wind Energy. Ser. Green energy Technol.*, pp. 287–305.

Buffoni, M., Galletti, B., Ferreau, J., Fagiano, L. & Mercangoez, M. 2014 Active pitch control of tethered wings for airborne wind energy. In *53rd IEEE Conf. Decis. Control*, pp. 4893–4898. IEEE.

BVG Associates 2022 Getting airborne - the need to realise the benefits of airborne wind energy for net zero. *Tech. Rep.* September. Airborne Wind Europe.

Candade, A. A., Ranneberg, M. & Schmehl, R. 2020*a* Aero-structural Design of Composite Wings for Airborne Wind Energy Applications. *J. Phys. Conf. Ser.* **1618** (3).

Candade, A. A., Ranneberg, M. & Schmehl, R. 2020*b* Structural analysis and optimization of a tethered swept wing for airborne wind energy generation. *Wind Energy* **23** (4), 1006–1025.

Carr, L. W. 1988 Dynamic stall progress in analysis and prediction. *J. Aircr.* **25** (1).

Carr, L. W., McCroskey, W. J., McAlister, K. W., Carr, L. W., Pucci, S. L. & Lambert, O. 1982 An experimental study of Dynamic Stall on advanced airfoil sections Volume 3. Hot-wire and hot-film measurements. *Tech. Rep.* 84245.

Castro-Fernández, I., Borobia-Moreno, R., Cavallaro, R. & Sánchez-Arriaga, G. 2021 Three-Dimensional Unsteady Aerodynamic Analysis of a Rigid-Framed Delta Kite Applied to Airborne Wind Energy. *Energies* **14** (23), 8080.

Castro-Fernández, I., DeLosRíos-Navarrete, F., Borobia-Moreno, R., Fernández-Jiménez, M., García-Cousillas, H., Zas-Bustingorri, M., Ghobaissi, Á. T., López-Vega, F., Best, K., Cavallaro, R. & Sánchez-Arriaga, G. 2023 Automatic testbed with a visual motion tracking system for airborne wind energy applications. *Wind Energy* **26** (4), 388–401.

Cavallaro, R., Nardini, M. & Demasi, L. 2015 Amphibious prandtlplane: Preliminary design aspects including propellers integration and ground effect. In *56th AIAA/ASCE/AHS/ASC Struct. Struct. Dyn. Mater. Conf.*, pp. 1–27.

Cayon, O., Gaunaa, M. & Schmehl, R. 2023 Fast Aero-Structural Model of a Leading-Edge Inflatable Kite. *Energies* **16** (7), 3061.

Cherubini, A., Papini, A., Vertechy, R. & Fontana, M. 2015 Airborne Wind Energy Systems: A review of the technologies. *Renew. Sustain. Energy Rev.* **51**, 1461–1476.

Cobb, M. K., Barton, K., Fathy, H. & Vermillion, C. 2020 Iterative Learning-Based Path Optimization for Repetitive Path Planning, with Application to 3-D Crosswind Flight of Airborne Wind Energy Systems. In *IEEE Trans. Control Syst. Technol.*, , vol. 28, pp. 1447–1459.

Coleman, J., Ahmad, H. & Toal, D. 2017 Development and Testing of a Control System for the Automatic Flight of Tethered Parafoils. *J. F. Robot.* **34** (3), 519–538.

Costello, S., Costello, C., François, G. & Bonvin, D. 2015 Analysis of the maximum efficiency of kite-power systems. *J. Renew. Sustain. Energy* **7** (5).

Costello, S., Francois, G. & Bonvin, D. 2018 Real-Time Optimizing Control of an Experimental Crosswind Power Kite. *IEEE Trans. Control Syst. Technol.* **26** (2), 507–522.

Damiani, R., Wendt, F., Jonkman, J. & Sicard, J. 2019 A vortex step method for nonlinear airfoil polar data as implemented in KiteAeroDyn. In *AIAA Scitech 2019 Forum*, pp. 1–11.

De Fezza, G. D. & Barber, S. 2022 Parameter analysis of a multi-element airfoil for application to airborne wind energy. *Wind Energy Sci.* **7**, 1627–1640.

De Schutter, J., Leuthold, R., Bronnenmeyer, T., Malz, E., Gros, S. & Diehl, M. 2023 AWEbox: An Optimal Control Framework for Single- and Multi-Aircraft Airborne Wind Energy Systems. *Energies* **16** (4), 1900.

Deodhar, N., Bafandeh, A., Deese, J., Smith, B., Muyimbwa, T., Vermillion, C. & Tkacik, P. 2017 Laboratory-Scale flight characterization of a multitethered aerostat for wind energy generation. *AIAA J.* **55** (6), 1823–1832.

Dolf Gielen, Gorini, R., Wagner, N., Leme, R., Gutierrez, L. & Prakash, G. 2018 Global Energy Transformation. *Tech. Rep.*. International Renewable Energy Agency (IRENA).

Echeverri, P., Fricke, T., Homsy, G. & Tucker, N. 2020*a* The Energy Kite: Selected

Results From The Design, Deelopmend and Testing of Makani's Airborne Wind Turbines Part1. *Tech. Rep.*. Makani.

Echeverri, P., Fricke, T., Homsy, G. & Tucker, N. 2020*b* The Energy Kite Selected Results from the Design, Development and Testing of Makani's Airborne Wind Turbines Part III, Technical Artifacts Makani Team The Energy Kite: Selected Results from the Design, Development, and Testing of Makani's Airborne Wind Tu. *Tech. Rep.*. Makani.

Economon, T. D., Palacios, F., Copeland, S. R., Lukaczyk, T. W. & Alonso, J. J. 2016 SU2: An open-source suite for multiphysics simulation and design. *AIAA J.* **54** (3), 828–846.

Ecorys 2018 Study on Challenges in the commercialisation of airborne wind energy systems. *Tech. Rep.*. European Commission.

Eijkelhof, D., Buendía, G. & Schmehl, R. 2023 Low- and High-Fidelity Aerodynamic Simulations of Box Wing Kites for Airborne Wind Energy Applications. *Energies* **16** (7), 3008.

Eijkelhof, D. & Schmehl, R. 2022 Six-degrees-of-freedom simulation model for future multi-megawatt airborne wind energy systems. *Renew. Energy* **196**, 137–150.

Ekaterinaris, J. A. & Platzer, M. F. 1997 Computational prediction of airfoil dynamic stall. *Prog. Aerosp. Sci.* **33** (11-12), 759–846.

Eldredge, J. D. & Jones, A. R. 2019 Leading-edge vortices: Mechanics and modeling. *Annu. Rev. Fluid Mech.* **51** (August 2018), 75–104.

Erhard, M. & Strauch, H. 2013 Control of towing kites for seagoing vessels. *IEEE Trans. Control Syst. Technol.* **21** (5), 1629–1640.

Erhard, M. & Strauch, H. 2015 Flight control of tethered kites in autonomous pumping cycles for airborne wind energy. *Control Eng. Pract.* **40**, 13–26.

Fagiano, L., Huynh, K., Bamieh, B. & Khammash, M. 2014*a* On Sensor Fusion for Airborne Wind Energy Systems. *IEEE Trans. Control Syst. Technol.* **22** (3), 930–943.

Fagiano, L. & Marks, T. 2015 Design of a small-scale prototype for research in airborne wind energy. *IEEE/ASME Trans. Mechatronics* **20** (1), 166–177.

Fagiano, L. & Milanese, M. 2012 Airborne Wind Energy: An overview. *Proc. Am. Control Conf.* pp. 3132–3143.

Fagiano, L., Nguyen-Van, E., Rager, F., Schnez, S. & Ohler, C. 2017*a* A Small-Scale Prototype to Study the Takeoff of Tethered Rigid Aircrafts for Airborne Wind Energy. *IEEE/ASME Trans. Mechatronics* **22** (4), 1869–1880.

Fagiano, L., Nguyen-Van, E., Rager, F., Schnez, S. & Ohler, C. 2017*b* Automatic Take-Off of a Tethered Aircraft for Airborne Wind Energy: Control Design and Experimental Results. *IFAC-PapersOnLine* **50** (1), 11932–11937.

Fagiano, L., Nguyen-Van, E., Rager, F., Schnez, S. & Ohler, C. 2018 Autonomous Takeoff and Flight of a Tethered Aircraft for Airborne Wind Energy. *IEEE Trans. Control Syst. Technol.* **26** (1), 151–166.

Fagiano, L. & Novara, C. 2014 Automatic crosswind flight of tethered wings for airborne wind energy: A direct data-driven approach. *IFAC Proc. Vol.* **19**, 4927–4932.

Fagiano, L., Zgraggen, A. U., Morari, M. & Khammash, M. 2014*b* Automatic crosswind flight of tethered wings for airborne wind energy: Modeling, control design, and experimental results. *IEEE Trans. Control Syst. Technol.* **22** (4), 1433–1447.

Fasel, U., Keidel, D., Molinari, G. & Ermanni, P. 2017 Aerostructural optimization of a morphing wing for airborne wind energy applications. *Smart Mater. Struct.* **26**, 1–11.

Fasel, U., Tiso, P., Keidel, D., Molinari, G. & Ermanni, P. 2019 Reduced-order dynamic model of a morphing airborne wind energy aircraft. *AIAA J.* **57** (8), 3586–3598.

Fechner, U., van der Vlugt, R., Schreuder, E. & Schmehl, R. 2015 Dynamic model of a pumping kite power system. *Renew. Energy* **83**, 705–716.

Folkersma, M., Schmehl, R. & Viré, A. 2019 Boundary layer transition modeling on leading edge inflatable kite airfoils. *Wind Energy* **22** (7), 908–921.

Folkersma, M., Schmehl, R. & Vire, A. 2020 Steady-state aeroelasticity of a ram-air wing for airborne wind energy applications. *J. Phys. Conf. Ser.* (September), 1–13.

Fonzi, N., Brunton, S. L. & Fasel, U. 2020 Data-driven nonlinear aeroelastic models of morphing wings for control. In *R. Soc. A*, pp. 1–23.

Fonzi, N., Cavalieri, V., Gaspari, A. D. & Ricci, S. 2022 Extended computational capabilities for high-fidelity fluid – structure simulations. *J. Comput. Sci.* **62** (May), 1–18.

Gaunaa, M. 2023 Influence of implementation details in the accuracy of lifting line models for airborne wind energy applications. In *WESC 2023*.

Gaunaa, M., Carqueija, F. P. P., Réthoré, P.-E. & Sørensen, N. N. 2011 A computationally efficient method for determining the aerodynamic performance of kites for wind energy applications. In *EWEA 2011*, pp. 1–11.

Geebelen, K., Vukov, M., Wagner, A., Ahmad, H., Zanon, M., Gros, S., Vandepitte, D., Swevers, J. & Diehl, M. 2013 An Experimental Test Setup for Advanced Estimation and Control of an Airborne Wind Energy System. In *Airborne Wind Energy. Ser. Green energy Technol.*, pp. 459–471.

González, S. & Moreno, H. 2019 Gone with the Wind: Providing Forecasts to the Polar Windsled Expeditions. *Helmholtz Blogs* .

Gordnier, R. E. & Visbal, M. R. 2004 Computation of the aeroelastic response of a flexible delta wing at high angles of attack. *J. Fluid Struct.* **19**, 785–800.

Gray, J. M., Gursul, I. & Butler, R. 2003 Aeroelastic Response of a Flexible Delta Wing due to Unsteady Vortex Flows. *41st Aerosp. Sci. Meet. Exhib. AIAA 2003-1106* (January), 1–8.

Gros, S. & Diehl, M. 2013 Modeling of Airborne Wind Energy Systems in Natural Coordinates. In *Airborne Wind Energy. Ser. Green energy Technol.* (ed. U. Ahrens, M. Diehl & R. Schmehl).

Gros, S., Zanon, M. & Diehl, M. 2013 Model predictive control of rigid-airfoil Airborne Wind Energy systems. In *2013 Eur. Control Conf.*, pp. 219–233.

Gursul, I. 2004 Recent developments in delta wing aerodynamics. *Aeronaut. J.* (2894), 437 – 452.

Haas, T., De Schutter, J., Diehl, M. & Meyers, J. 2022 Large-eddy simulation of airborne wind energy farms. *Wind Energy Sci.* **7** (3), 1093–1135.

Gad-el Hak, M. & Ho, C. M. 1985 Three-dimensional effects on a pitching lifting surface. *AlAA 23rd Aerosp. Sci. Meet.* .

Ham, N. D. 1968 Aerodynamic loading on a two-dimensional airfoil during dynamic stall. *AIAA J.* **6** (10), 1927–1934.

Ham, N. D. & Garelick, M. S. 1968 Dynamic Stall Considerations in Helicopter Rotors. *J. Am. Helicopter Soc.* **13** (2), 49–55.

Hansen, M., Gaunaa, M. & Aagaard Madsen, H. 2004 A Beddoes-Leishman type dynamic stall model in state-space and indicial formulations. *Tech. Rep.*. Forskningscenter Risoe.

Healy, F., Pontillo, A., Rezgui, D., Cooper, J. E., Kirk, J., Wilson, T. & Castrichini, A. 2022 Experimental Analysis of the Dynamics of Flared Folding Wingtips via a Novel Tethered Flight Test. *AIAA 2022-1757* (January).

Hesse, H., Polzin, M., Wood, T. A. & Smith, R. S. 2018 Visual motion tracking and sensor fusion for kite power systems. In *Airborne Wind Energy. Ser. Green energy Technol.*, , vol. 9789811019, pp. 413–438.

Heudorfer, K. & Dobler, U. 2022 The ICM-autoKite Project: Developing an Automated Kite Propulsion System for the KITE GAS/FUEL SHIP and Economic Green Hydrogen Production. In *Airborne Wind Energy Conf.*, p. 2022.

Hirsch, C. 1984 *Numerical computation of internal and external flows*. New York: Wiley.

Hoff, J. C. & Cook, M. V. 1996 Aircraft Parameter Estimation by an Estimation-Before-Modelling Technique. *Aeronaut. J. R. Aeronaut. Soc.* (January 1996).

Hummel, J., Göhlich, D. & Schmehl, R. 2019 Automatic measurement and characterization of the dynamic properties of tethered membrane wings. *Wind Energy Sci.* **4** (1), 41–55.

IPCC 2023 Synthesis Report of the IPCC Sixth Assessment Report (AR6). *Eur. Univ. Inst.* (2), 2–5.

Kannala, J. & Brandt, S. S. 2006 A Generic Camera Model and Calibration Method for Conventional, Wide-Angle, and Fish-Eye Lenses. *Pattern Anal. Mach. Intell.* **28** (8), 1–15.

Katz, J. & Plotkin, A. 2001 *Low-Speed Aerodynamics*, 2nd edn. San Diego.

Kheiri, M., Bourgault, F., Saberi Nasrabad, V. & Victor, S. 2018 On the aerodynamic performance of crosswind kite power systems. *J. Wind Eng. Ind. Aerodyn.* **181** (August), 1–13.

Kheiri, M., Victor, S., Rangriz, S., Karakouzian, M. M. & Bourgault, F. 2022 Aerodynamic Performance and Wake Flow of Crosswind Kite Power Systems. *Energies* **15** (7), 2449.

Kitepower 2022 Webpage of Kitepower. [https://thekitepower.com/].

Ko, A. P., Smidt, S., Schmehl, R. & Mandru, M. 2023 Optimization of a Multi-Element Airfoil for a Fixed-Wing Airborne Wind Energy System. *Energies* **16** (8), 3521.

Leishman, J. . & Beddoes, T. S. 1989 A Semi-Empirical Model for Dynamic Stall. *J. Am. Helicopter Soc.* pp. 3–17.

Leloup, R., Roncin, K., Bles, G. & Leroux, J.-b. 2013 Estimation of the Lift-to-Drag Ratio Using the Lifting Line Method : Application to a Leading Edge Inflatable Kite. In *Airborne Wind Energy. Ser. Green energy Technol.*, pp. 339–355.

Leuthold, R. 2015 Multiple-Wake Vortex Lattice Method for Membrane-Wing Kites. *Tech. Rep.* December 2015. Delft University of technology.

Leuthold, R., Gros, S. & Diehl, M. 2017 Induction in Optimal Control of Multiple-Kite Airborne Wind Energy Systems. *IFAC-PapersOnLine* **50** (1), 153–158.

Licitra, G., Bürger, A., Williams, P., Ruiterkamp, R. & Diehl, M. 2019 Aerodynamic model identification of an autonomous aircraft for airborne wind energy. *Optim. Control Appl. Methods* **40** (3), 422–447.

Licitra, G., Williams, P., Gillis, J., Ghandchi, S., Sieberling, S., Ruiterkamp, R. & Diehl, M. 2017 Aerodynamic Parameter Identification for an Airborne Wind Energy Pumping System. *IFAC-PapersOnLine* **50** (1), 11951–11958.

Loyd, M. L. 1980 Crosswind Kite Power. *J. Energy* .

Makani Team 2020 The Energy Kite Selected Results from the Design, Development and Testing of Makani's Airborne Wind Turbines Part II. *Tech. Rep.*. Makani.

Malz, E. C., Koenemann, J., Sieberling, S. & Gros, S. 2019 A reference model for airborne wind energy systems for optimization and control. *Renew. Energy* **140**, 1004–1011.

Mangler, K. W. & Smith, J. H. B. 1970 Behaviour of the Vortex Sheet at the Trailing Edge of a Lifting Wing. *Aeronaut. J. R. Aeronaut. Soc.* **74**, 906–908.

Manuel C. R. M. Fernandes, L. T. P. & Fontes, F. A. C. C. 2021 *Optimal Path and Path-Following Control in Airborne Wind Energy Systems*, , vol. 36. Springer.

McAlister, K. W., Pucci, S. L., McCroskey, W. J. & Carr, L. W. 1982 An Experimental Study of Dynamic Stall on Advanced Airfoil Sections Volume 2. Pressure and Force Data. *Tech. Rep.*. NASA.

McCroskey, W. J., McAlister, K. W., Carr, L. W. & Pucci, S. L. 1982 An ExperimentalStudy of Dynamic Stall on Advanced Airfoil Sections. Volume 1. Summary of the Experiment. *Tech. Rep.*. NASA.

Mehr, J., Alvarez, E. J. & Ning, A. 2020 Unsteady aerodynamic analysis of wind harvesting aircraft. In *Aiaa Aviat. 2020 Forum*, pp. 1–13.

Menter, F. R. 1994 Two-equation eddy-viscosity turbulence models for engineering applications. *AIAA J.* **32** (8), 1598–1605.

Milanese, M., Taddei, F. & Milanese, S. 2013 Design and Testing of a 60 kW Yo-Yo Airborne Wind Energy Generator. In *Airborne Wind Energy. Ser. Green energy Technol.*.

Millane, A., Hesse, H., Wood, T. A. & Smith, R. S. 2015 Range-inertial estimation for airborne wind energy. *Proc. IEEE Conf. Decis. Control* **54rd IEEE** (Cdc), 455–460.

Nardini, M. 2014 A Computational Multi-purpose Unsteady Aerodynamic Solver for the Analysis of Innovative Wing Configurations, Helicopter Blades and Wind Turbines. *Tech. Rep.*. University of Pisa.

Ockels, W. J. 2001 Laddermill, a novel concept to exploit the energy in the airspace. *Aircr. Des.* **4** (2-3), 81–97.

Oehler, J. & Schmehl, R. 2019 Aerodynamic characterization of a soft kite by in situ flow measurement. *Wind Energy Sci.* **4** (1), 1–21.

Orzan, N., Leone, C., Mazzolini, A., Oyero, J. & Celani, A. 2023 Optimizing airborne wind energy with reinforcement learning. *Eur. Phys. J. E* **46** (1), 1–8.

Palacios, F., Colonno, M. R., Aranake, A. C., Campos, A., Copeland, S. R., Economon, T. D., Lonkar, A. K., Lukaczyk, T. W., Taylor, T. W. R. & Alonso, J. J. 2013 Stanford University Unstructured (SU 2): An open-source integrated computational environment for multi-physics simulation and design . In *51st AIAA Aerosp. Sci. Meet. Incl. New Horizons Forum Aerosp. Expo.*, pp. 1–60.

Palacios, F., Economon, T. D., Aranake, A. C., Copeland, S. R., Lonkar, A. K., Lukaczyk, T. W., Manosalvas, D. E., Naik, K. R., Padr, A. S., Tracey, B., Variyar, A. & Alonso, J. J. 2014 Stanford University Unstructured (SU 2): Open-source Analysis and Design Technology for Turbulent Flows. In *52nd Aerosp. Sci. Meet.*, pp. 1–33.

Pereira, R. 2020 Aerofoil Aerodynamics of Wind Energy Devices. In *Handb. Wind Energy Aerodyn.* (ed. B. Stoevesandt, G. Schepers, P. Fuglsang & S. Yuping), pp. 1–22. Springer, Cham.

Prandtl, L. 1918 Theory of Lifting Surfaces. *Tech. Rep.*. National Advisory Committee for Aeronautics, Washington, DC.

Pynaert, N., Haas, T., Wauters, J., Crevecoeur, G. & Degroote, J. 2023 Wing Deformation of an Airborne Wind Energy System in Crosswind Flight Using High-Fidelity Fluid – Structure Interaction. *Energies* **16** (2), 602.

Ranneberg, M. 2015 Direct Wing Design and Inverse Airfoil Identification with the Nonlinear Weissinger Method. *Tech. Rep.*.

Redmon, J., Divvala, S., Girshick, R. & Farhadi, A. 2016 You Only Look Once: Unified, Real-Time Object Detection. *Proc. - 30th IEEE Conf. Comput. Vis. Pattern Recognition, CVPR 2016* .

Redmon, J. & Farhadi, A. 2017 YOLO9000: Better, faster, stronger. *Proc. - 30th IEEE Conf. Comput. Vis. Pattern Recognition, CVPR 2017* **2017-Janua**, 6517–6525.

Rushdi, M. A., Dief, T. N., Yoshida, S. & Schmehl, R. 2020 Towing test data set of the kyushu university kite system. *Data* **5** (3), 1–18.

Saleem, A. & Kim, M. H. 2020 Aerodynamic performance optimization of an airfoil-based airborne wind turbine using genetic algorithm. *Energy* **203**, 117841.

Salma, V., Friedl, F. & Schmehl, R. 2020 Improving reliability and safety of airborne wind energy systems. *Wind Energy* (April 2019), 340–356.

Sánchez-Arriaga, G., García-Villalba, M. & Schmehl, R. 2017 Modeling and dynamics of a two-line kite. *Appl. Math. Model.* **47**, 473–486.

Sánchez-arriaga, G., Pastor-rodríguez, A., Sanjurjo-rivo, M. & Schmehl, R. 2019 A lagrangian flight simulator for airborne wind energy systems. *Appl. Math. Model.* **69**, 665–684.

Sánchez-Arriaga, G., Serrano-Iglesias, J. A., Leuthold, R. & Diehl, M. 2021 Modeling and Natural Mode Analysis of Tethered Multi-Aircraft Systems. *J. Guid. Control. Dyn.* **44** (6), 1199–1210.

Schmehl, R. 2019 Airborne Wind Energy - An introduction to an emerging technology. [https://awesco.eu/awe-explained/].

Schmidt, E., De Lellis Costa De Oliveira, M., Saraiva Da Silva, R., Fagiano, L. & Trofino Neto, A. 2020 In-Flight Estimation of the Aerodynamics of Tethered Wings for Airborne Wind Energy. *IEEE Trans. Control Syst. Technol.* **28** (4), 1309–1322.

Shahzad, A., Gao, X., Yasin, A., Javed, K. & Anwar, S. M. 2020 A vision-based path planning and object tracking framework for 6-DOF robotic manipulator. *IEEE Access* **8**, 203158–203167.

Sheng, W., Chan, W. & Galbraith, R. 2012 Advancement of aerofoil section dynamic stall synthesis methods for rotor design. *Aeronaut. J.* **116**, 521–539.

Sheng, W., Galbraith, R. A. M. & Coton, F. N. 2008 A Modified Dynamic Stall Model for Low Mach Numbers 1. *J. Sol. Energy Eng.* **130** (August 2008), 1–10.

Simon, D. 2006 *Optimal State Estimation - Kalman, H Infinity and Nonlinear Approaches*. New Jersey: Wiley Interscience.

SkySails Power 2022 Webpage of Skysails Power. [https://skysails-power.com/].

Smolyanskiy, N., Kamenev, A. & Birchfield, S. 2018 On the importance of stereo for accurate depth estimation: An efficient semi-supervised deep neural network approach. *IEEE Comput. Soc. Conf. Comput. Vis. Pattern Recognit. Work.* **2018-June**, 1120–1128.

Spentzos, A., Barakos, G. N., Badcock, K. J., Richards, B. E., Coton, F. N., Galbraith, R. A. D., Berton, E. & Favier, D. 2007 Computational fluid dynamics study of three-dimensional dynamic stall of various planform shapes. *J. Aircr.* **44** (4), 1118–1128.

Thedens, P., de Oliveira, G. & Schmehl, R. 2019 Ram-air kite airfoil and reinforcements optimization for airborne wind energy applications. *Wind Energy* **22** (5), 653–665.

Thedens, P. & Schmehl, R. 2023 An Aero-Structural Model for Ram-Air Kite Simulations. *Energies* **16** (6), 2603.

Thwaites, B. 1960 *Incompressible aerodynamics : an account of the theory and observation of the steady flow of incompressible fluid past aerofoils, wings and other bodies*. New York: Dover Publications.

Tran, C. T. & Petot, D. 1980 Semi-empirical model for the dynamic stall of airfoils in view of the application to the calculation of responses of a helicopter blade in forward flight. In *Sixth Eur. Rotorcr. Powered Lift Aircr. Forum*, pp. 1–23.

Trevisi, F., Castro-Fernández, I., Pasquinelli, G., Riboldi, C. E. D. & Croce, A. 2022 Flight trajectory optimization of Fly-Gen airborne wind energy systems through a harmonic balance method. *Wind Energy Sci.* **7** (5), 2039–2058.

Trevisi, F., Riboldi, C. E. D. & Croce, A. 2023 Vortex model of the aerodynamic wake of airborne wind energy systems. *Wind Energy Sci.* **8** (6), 999–1016.

Universidad Carlos III de Madrid 2022 Web page of the UC3M Airborne Wind Energy group. [https://aero.uc3m.es/airborne-wind-energy/].

Universidad Carlos III de Madrid 2023 UC3M-CT Ingenieros flight campaign (April 23). [https://www.youtube.com/watch?v=W9tkuaRj83w].

U.S. Department of Energy 2021 Report to Congress: Challenges and Opportunities for Airborne Wind Energy in the United States. *Tech. Rep.* November. United States Department of Energy, Washington, DC 20585.

Vermillion, C., Cobb, M., Fagiano, L., Leuthold, R., Diehl, M., Smith, R. S., Wood, T. A., Rapp, S., Schmehl, R., Olinger, D. & Demetriou, M. 2021 Electricity in the air: Insights from two decades of advanced control research and experimental flight testing of airborne wind energy systems. *Annu. Rev. Control* **52** (December 2020), 330–357.

Vimalakanthan, K., Caboni, M., Schepers, J., Pechenik, E. & P.Williams 2018 Aerodynamic analysis of Ampyx's airborne wind energy system. *J. Phys. Conf. Ser.* **1037**, 1–10.

Viré, A., Demkowicz, P., Folkersma, M., Roullier, A. & Schmehl, R. 2020 Reynolds-averaged Navier-Stokes simulations of the flow past a leading edge inflatable wing for airborne wind energy applications. *J. Phys. Conf. Ser.* **1618** (3).

Viré, A., Lebesque, G., Folkersma, M. & Schmehl, R. 2022 Effect of Chordwise Struts and Misaligned Flow on the Aerodynamic Performance of a Leading-Edge Inflatable Wing. *Energies* **15** (4), 1450.

van der Vlugt, R., Peschel, J. & Schmehl, R. 2013 Design and Experimental Characterization of a Pumping Kite Power System. In *Airborne Wind Energy. Ser. Green energy Technol.*.

de Wachter, A. 2008 Deformation and Aerodynamic Performance of a Ram-Air Wing. *Tech. Rep.* July. Technical University of Delft.

Watson, S., Moro, A., Reis, V., Baniotopoulos, C., Barth, S., Bartoli, G., Bauer, F., Boelman, E., Bosse, D., Cherubini, A., Croce, A., Fagiano, L., Fontana, M., Gambier, A., Gkoumas, K., Golightly, C., Latour, M. I., Jamieson, P., Kaldellis, J., Macdonald, A., Murphy, J., Muskulus, M., Petrini, F., Pigolotti, L., Rasmussen, F., Schild, P., Schmehl, R., Stavridou, N., Tande, J., Taylor, N., Telsnig, T. & Wiser, R. 2019 Future emerging technologies in the wind power sector: A European perspective. *Renew. Sustain. Energy Rev.* **113** (October), 109270.

White, F. M. 1974 *Viscous Fluid Flow*. New York: McGraw-Hill.

Wijnja, J., Schmehl, R., Breuker, R. D., Jensen, K. & Lind, D. V. 2018 Aeroelastic Analysis of a Large Airborne Wind Turbine. *J. Guid. Control. Dyn.* **41**, 1–12.

Wilcox, D. C. 2006 *Turbulence Modelling for CFD*, 3rd edn. DCW Industries.

Williams, P. 2017 Cable modeling approximations for rapid simulation. *J. Guid. Control. Dyn.* **40** (7), 1778–1787.

Wood, T. A., Hesse, H., Zgraggen, A. U. & Smith, R. S. 2015 Model-based identification and control of the velocity vector orientation for autonomous kites. *Proc. Am. Control Conf.* **2015-July**, 2377–2382.

Zanon, M., Gros, S., Meyers, J. & Diehl, M. 2014 Airborne wind energy: Airfoil-airmass interaction. *IFAC Proc. Vol.* **19** (2013), 5814–5819.

Zgraggen, A. U., Fagiano, L. & Morari, M. 2015 Real-time optimization and adaptation of the crosswind flight of tethered wings for airborne wind energy. *IEEE Trans. Control Syst. Technol.* **23** (2), 434–448.